INSTABILITY AND WAVE-GROWTH WITHIN SOME OSCILLATORY FLUID FLOWS

Graham Keith Forster

A Thesis Submitted for the Degree of PhD
at the
University of St Andrews

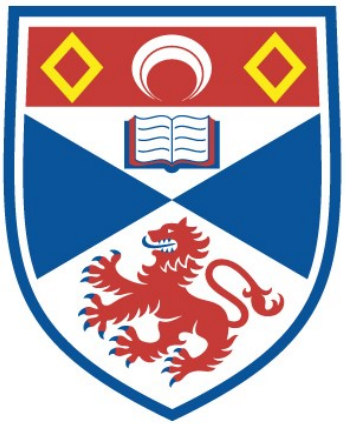

1996

Full metadata for this item is available in
St Andrews Research Repository
at:
http://research-repository.st-andrews.ac.uk/

Please use this identifier to cite or link to this item:
http://hdl.handle.net/10023/14087

This item is protected by original copyright

Instability and Wave-growth within some Oscillatory Fluid Flows.

Graham Keith Forster.

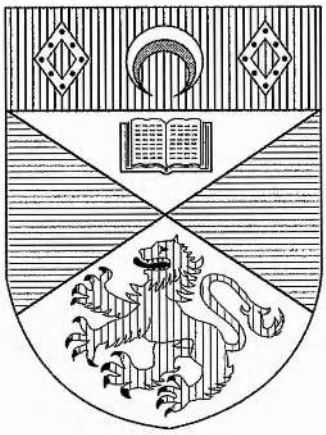

BIBLIOTHECA UNIVERSITATIS ANDREANÆ

Thesis submitted for the degree of Doctor of Philosophy of the University of St. Andrews on 7^{th} November 1995.

ProQuest Number: 10167375

All rights reserved

INFORMATION TO ALL USERS
The quality of this reproduction is dependent upon the quality of the copy submitted.

In the unlikely event that the author did not send a complete manuscript
and there are missing pages, these will be noted. Also, if material had to be removed,
a note will indicate the deletion.

ProQuest 10167375

Published by ProQuest LLC (2017). Copyright of the Dissertation is held by the Author.

All rights reserved.
This work is protected against unauthorized copying under Title 17, United States Code
Microform Edition © ProQuest LLC.

ProQuest LLC.
789 East Eisenhower Parkway
P.O. Box 1346
Ann Arbor, MI 48106 – 1346

TL
B936

To Henry.

Abstract.

Oscillatory fluid flows arise naturally in many systems. Whether or not these systems are stable is an important question and external periodic forcing of the flow may result in rich and complicated behaviours. Here three distinct oscillatory fluid flows are examined in detail, with the stability of each being established using a range of analytical and computational methods.

The first system comprises standing surface capillary-gravity waves in second-harmonic resonance subject to Faraday excitation. Using the perturbation technique of multiple scales, the amplitude equations for the system are derived. At exact resonance, and with the absence of damping, the only fixed point of the equations is found to be the origin. A computational approach reveals that the amplitudes of the two waves remain either bounded or grow to infinity depending on initial data. With the introduction of detuning and damping into the system families of fixed points now exist and some special cases are considered.

The second class of flows are unbounded time-periodic flows with fixed ellipsoidal stream surfaces, and having spatially uniform but time-periodic strain rates. Using a recently developed method based on theoretical study of the Schrödinger equation with quasi-periodic potential, a computational approach is adopted which determines the stability of the flow to three-dimensional plane wave disturbances. Results for the growth rate and winding number of the disturbance clearly reveal the regions of instability. It is found that almost all these

flows are highly unstable.

The third class is another set of three-dimensional time-periodic flows with spatially uniform strain rates. These flows are non-axisymmetric and have sinusoidally-fluctuating rates of strain directed along the fixed coordinate axes. The same computational method is employed and it is found that instability increases along with the non-axisymmetric nature of the flow.

Declaration

1. I, Graham Keith Forster, hereby certify that this thesis, which is approximately 30,000 words in length, has been written by me, that it is a record of work carried out by me and that it has not been submitted in any previous application for a higher degree.

   date ...6/11/95.....signature of candidate .. ..

2. I was admitted as a research student in October 1992 and as a candidate for the degree of Ph.D. in October 1993; the higher study for which this is a record was carried out in the University of St. Andrews between 1992 and 1995.

   date ...6/11/95.....signature of candidate ... .

3. I hereby certify that the candidate has fulfilled the conditions of the Resolution and Regulations appropriate to the Degree of Ph.D. in the University of St. Andrews and that the candidate is qualified to submit this thesis in application for that degree.

   date ...6/11/95.....signature of supervisor ..

Copyright

1. In submitting this thesis to the University of St. Andrews I understand that I am giving permission for it to be made available for use in accordance with the regulations of the University Library for the time being in force, subject to any copyright vested in the work not being affected thereby. I also understand that the title and abstract will be published, and that a copy of the work may be made and supplied to any bona fide library or research worker.

date ..6/11/95..... signature of candidate .. ....

Acknowledgements.

I would like to take this opportunity to thank all my friends and colleagues for the years of enjoyment I have had in St. Andrews. I am especially grateful to Richard Ireland and Alan Johnston for the time they sacrificed in order to help me overcome my fear of computers, and to Tim Bungey and Tricia Heggie for their assistance with my programming. Special mention must go as well to Steve Decent, who, besides lending a willing ear to my problems and ideas, made an ideal and appreciated drinking partner at those conferences we attended around the globe.

My mother and father have been a constant source of support and encouragement over the years and to them I will always be indebted. Their understanding and tolerance of my lengthy student days will never be forgotten.

Most of all though, I wish to thank my supervisor Alex Craik. Above all else it is the invaluable advice and guidance that I have received off Alex over the last three years that has enabled me to overcome the pitfalls of research and complete this thesis.

Contents

Chapter 1

Introduction to parametrically forced resonant wave interactions.

1.1 Surface waves.

The classical study of water waves was concerned mainly with waves of infinitesimal amplitude in a non-viscous liquid. For such waves the surface boundary conditions can be linearized and the system reduces to a set of linear partial differential equations. The principle of superposition is then invoked and this enables the use of Fourier-series to describe the contributions of wave trains. Although highly developed, this approach is extremely restrictive since the equations of

fluid dynamics are inherently non-linear.

Stokes (1847) was the first to propose a weakly non-linear analysis. He obtained second-order corrections to the profile and frequency of waves whose amplitudes were no longer infintesimal, and showed that the frequency of such waves was dependent on the amplitude as well as the wave-number. This approximation was extended to third order by Harrison (1909) who again found that non-linearities distorted the wave profile of capillary-gravity waves whose wave numbers were less than a certain critical value $k^* = (g/2\gamma)^{\frac{1}{2}}$ (g being the acceleration due to gravity, γ the ratio of the surface coefficient to the density of the fluid). When the wave-number was exactly k^* this appoximation was found to break down and the analysis predicted a second harmonic distortion of the sinusoidal profile that had infinite amplitude. Carrying the same procedure to fifth order, Wilton (1915) found that the same singularity exists at all orders of the approximation and occurs for wave-numbers $k = (g/n\gamma)^{\frac{1}{2}}$, with $n = 2, 3, 4, ...$

At first, this type of approach was thought to have very little application apart from the distortion of wave profiles and, until the 1960's, such non-linear effects were generally ignored. Details of the mathematical treatment describing these effects can be found in the books by Lamb (1932), Kinsman (1969) and Whitham (1974), to name a few.

1.2 Resonant wave interactions.

While the non-linear terms contained within the governing equations were generally ignored, their existance could not be disputed. The question of whether such terms had a profound effect on wavefield evolution still remained unanswered.

Inspired by current work on turbulence, Phillips (1960, 1961) set out to discover whether non-linearities could be responsible for energy exchanges among different waves. A resonance mechanism was found to exist, and this provided evidence that energy transfer could occur between between two or more trains of progressive gravity waves. For gravity waves, such an interaction was found to be impossible at second order, but at third order the 'resonance conditions' could be satisfied for quartets of wavenumbers and frequencies.

Longuet-Higgins (1962) investigated this phenomenon further. Employing a method using a Taylor series expansion, he calculated the interaction between the four waves and obtained the interaction coefficients. To add support to the theory, Longuet-Higgins & Smith (1966) and McGoldrick *et al* (1966) undertook an experiment to demonstrate resonant interactions between wavetrains. Their results, published simultaneously, confirmed that resonant interactions did exist, and the experimental growth rates obtained were very close to those calculated analytically.

This physical verification enabled resonant interaction theory to became uni-

versally accepted. Further work by Benney (1962), who applied the theory to a variety of phenomena and derived the complete interaction equations, and by Longuet-Higgins & Phillips (1962), who examined phase velocity effects in tertiary wave interactions, also added strength to the argument.

While the early analysis of Phillips and Longuet-Higgins concentrated solely on gravity waves, the effects of capillarity become important when the wavelengths are sufficiently short. Using a classical Taylor series expansion and the perturbation method of multiple scales, McGoldrick (1965) showed that resonant interactions at second-order were possible among triads of waves with wavelengths in the capillary-gravity and pure capillary ranges. It was further shown that waves with slowly varying amplitudes have solutions that integrate directly in terms of Jacobian elliptic functions with real parameters. Viscous effects were also considered, with linear attenuation terms simply added onto the evolution equations as a first approximation. Here the amplitudes of the waves became quasi-periodic and were found to decay with time.

This development by McGoldrick was initially followed up by Simmons (1969), who examined weak second-order interactions among waves whose amplitudes and phases varied slowly with position and time. Unlike McGoldrick, Simmons did not use the common but labourous series expansion to derive his evolution equations, but instead modified a variational technique developed by Whitham (1965a,b,1967). An averaging process was used in which the rapidly varying terms

averaged to zero, and the slowly varying terms averaged (locally) as constants. A Lagrangian formulation was then developed to incorporate the dynamical equations and boundary conditions into the problem. The amplitude solutions were found in terms of Jacobi elliptic functions and hyperbolic trigonometric functions. Simmons also considered the case of second-harmonic resonance and the periodic permanent form solution found by Wilton (1915) was recovered.

The investigation into second-harmonic resonance was expanded further by McGoldrick (1970a). Concentrating on the temporal case, it was shown that when represented in polar form, the equations possessed an energy integral independent of relative phase. It was found that when the relative phase was $\pm\frac{\pi}{2}$ the modulation period of the amplitudes became infinite and the solutions degenerated to their limiting case of hyperbolic functions.

McGoldrick (1970b) conducted an experiment on second-order capillary-gravity wave interactions. Waves were excited on the surface of a fluid by means of a wedge shaped plunger and the depth of fluid was large enough to be considered infinite. When the frequency of the plunger was set at that determined for second-harmonic resonance, it was found that the wave propagation was at utter variance with the theory. This difference was due to a surface film which developed on the surface of the fluid and affected the surface tension. Upon correcting the value of the surface tension, the experiments clearly showed the existence of second-harmonic resonance and the measured data confirmed the growth of the

second-harmonic at the expense of the fundamental.

McGoldrick (1972) continued the investigation into second-harmonic resonance and extended the analysis to third-harmonic resonance among capillary-gravity waves. The analytical features of the these two cases were then generalized to fourth, fifth and higher-harmonic resonance. McGoldrick used similar equipment and techniques as in the earlier investigation, except this time the water surface was renewed every twenty minutes by flushing it over a weir. For third, fourth and sixth-harmonic resonances, the maximum amplitude responses were found to occur at slightly lower frequencies than theory suggested and the results also showed that resonance persisted even when there was substantial detuning.

The question of detuning was again addressed by Nayfeh (1973). Here he considered travelling capillary-gravity waves resonating at close to the second harmonic on the surface of a liquid of finite depth. The investigation was centred around the interaction of such waves with an airstream travelling across the fluid surface. It was found that above a certain air velocity, pure amplitude-modulated waves were only possible at perfect resonance. Such detuning effects have also been considered by Wersinger, Finn & Ott (1980) and Hughes and Proctor (1994).

Case and Chiu (1977) extended the analysis of McGoldrick (1965) to seek solutions to three-wave interaction equations in which the phases of the waves varied slowly with space and time. Neglecting viscosity and dispersion effects, two special classes of solution were found to exist. The first was when the three

waves propagated with a common group velocity, a consequence of which was no energy exchange between the waves. The second class involved the annihilation of one wave and creation of another two, or the annihilation of two waves and the creation of a third. In this type of solution it was obvious that energy exchange did occur between the waves.

Banerjee and Korpel (1982) investigated deep-water capillary waves for which sub-harmonic generation was observed due to non-collinear resonant three-wave interaction. In a brief analysis based on McGoldrick (1965), they developed the theory for second-harmonic quadratic interactions and confirmed experimentally the existence of sub-harmonic standing waves. Banerjee & Korpel found that their data and results did not totally agree and it was suggested that the difference was due to the fact that the dispersion curve was amplitude dependant through cubic non-linearities not considered in the analysis.

Hogan (1984) re-examined the results obtained by Banerjee and Korpel and showed that they were actually in better agreement with McGoldrick's theory than at first thought. After theoretical examination of the resonant triad for second-harmonic resonance, Hogan concluded that the Schlieren system used in Banerjee & Korpel's experiment could not track the very low-amplitude and slightly non-linear waves formed on the fluid surface. Taking this into account and an experimental error of at least 10%, Hogan re-examined the data and showed that it was in overall agreement with the earlier theoretical predictions.

Since the pioneering work of Phillips, many more questions about resonant wave interactions have been answered. Papers by Kaup (1981), McDougall & Craik (1991), Jones (1992) and Craik, Nagata & Moroz (1992), add further to the understanding of such phenomena. Many reviews of such work have also been written, including those by Phillips (1981), Yuen & Lake (1982) and Hammack & Henderson (1993), with comprehensive descriptions of such interactions being found in monographs by Phillips (1977), West (1981) and Craik (1985) amongst others.

1.3 Faraday excitation.

How are such resonant interactions affected when external forcing is added into the system? The case of a vertical oscillating container was studied experimentally by Faraday (1831), who noticed that the frequency of the liquid vibrations on the free surface was only half that of the container. Matthiessen (1868, 1870) also studied this same problem, but this time his results indicated that the two vibrations were synchronous. This disagreement led Lord Rayleigh (1883a,b) to further repeat the experiments, and his results were found to be in general agreement with those of Faraday.

The first theoretical work on Faraday resonance was conducted by Benjamin & Ursell (1954). In this study they examined the linear stability of the free

surface of a liquid contained in a cylindrical container of arbitrary cross-section, where the liquid in the vessel had a depth h, and the vessel itself was accelerated vertically in a simple harmonic motion. Using ideal-fluid theory they showed that the dynamical equations and boundary conditions could be expressed in the form of Mathieu's equation, and from this it was found that wave modes of frequency $\omega, 2\omega, 3\omega, 4\omega....$ result from an excitation of frequency 2ω. Three discrete regions of instability were found, and these different regions were interpreted to account for the conflicting views of Faraday/Lord Rayleigh and those of Matthiessen.

The early theoretical work on linear Faraday resonance was continued by Dodge *et al* (1965), who gave a finite-amplitude analysis for a circular basin, and Ockendon & Ockendon (1973) who extended the work of Benjamin & Ursell to small but finite wave amplitudes. Further studies were conducted by Henstock & Sani (1974) and Miles (1976).

Miles (1984) furthered the investigation into Faraday forcing by considering non-linear effects. Constructing the average Lagrangian and invoking Hamiltons principle, Miles calculated the interaction coefficients and analysed the local stability of fixed point solutions for the damped system. Perfectly tuned superharmonic resonance was also considered for the case $\omega_2 = 2\omega_1$. Here no Hopf bifurcation points existed and thus limit cycles and chaotic motions were found to be impossible. [Evolution equations for such problems are isomorphic to those found in the study of an internally resonant double pendulum. see work by Rott

(1970) and Miles (1985).]

Using an asymptotic method of averaging, Mitropolsky (1965), Gu & Sethna (1987) derived the detuned second-harmonic resonance equations. In the detuned case, Faraday forcing at the first harmonic was found to lead to Hopf bifurcation points in certain parameter ranges. The appearance of these introduced a subset into the parameter space in which no stable periodic or quasi-periodic motions occurred. Here chaotic phenomena were shown to exist and this was verified by numerical investigation.

Henderson & Miles (1991) investigated a similar problem, conducting experiments on Faraday waves in a circular cylinder. Here the waves were internally resonant with either the subharmonic or superharmonic mode. For the subharmonic, the equivalent case for an internally resonant double pendulum had been considered by Becker & Miles (1986) who found Hopf bifurcations, limit cycles and chaos. Experimental results obtained by Henderson & Miles for the neutral stability of the Faraday were in close agreement with the earlier theoretical predictions, and some of the measured attractors in phase space were found to be similar to two of the attractors obtained numerically in the Becker & Miles study.

1.4 Outline of the investigation.

For our investigation, we concentrate on the second-harmonic resonance equations for which Faraday forcing occurs at the second harmonic. The resonance conditions and governing equations of the system are introduced in Chapter 2, with the interaction coefficients for the resulting evolution equations being calculated explicitly. Primarily the study is centred around the undamped, perfectly tuned equations, with Chapter 3 containing analytic and numerical results for the four-dimensional autonomous system and a reduced three-dimensional non-autonomous case. The damped and off-resonance equations are considered in Chapter 4. Here we rediscover the fixed point solutions of Becker & Miles (1986) and investigate further the stability of such solutions in certain special cases.

Chapter 2

Derivation of the resonance equations.

2.1 Introduction.

2.1.1 Three wave resonance.

If two or more waves with wave-numbers $\boldsymbol{k}_1$ and $\boldsymbol{k}_2$ are present in the same region of space at some arbitrary instant $t = t_0$, then the non-linear interaction between them will tend to force a third 'wave' with wave-number $\boldsymbol{k}_3$ equal to the sum or difference between the original two wave-numbers $\boldsymbol{k}_1$ and $\boldsymbol{k}_2$: i.e.

$$\boldsymbol{k}_1 \pm \boldsymbol{k}_2 = \pm \boldsymbol{k}_3. \tag{2.1}$$

This forced third 'wave' has frequency ω_3 equal to the sum or difference between the frequencies of the original two waves and if ω_3 is close to the natural frequency of a linear wave with wavenumber $\pm\boldsymbol{k}_3$, then resonance can occur. The resonance condition is therefore

$$\omega_1 \pm \omega_2 = \pm\omega_3 \tag{2.2}$$

where $\omega_i(\boldsymbol{k}_i)$ is the frequency of the wave with wave-number $\boldsymbol{k}_i$ (i=1,2,3), and the $\pm$ signs occur together in equations (2.1) and (2.2).

The two equations essentially form a set of four closed resonant triads, (2.1) for wave-numbers and (2.2) for frequencies. It is these two equations that, if satisfied, enable resonance to occur at second order. Phillips (1960) found that these equations could not be satisfied among pure surface gravity waves in deep water, where $\omega_i = (g|\boldsymbol{k}_i|)^{\frac{1}{2}}$, at second order for any choice of sign, but by looking at capillary-gravity waves McGoldrick (1965) found that they could.

By the incorporation of surface tension, the frequency for each of the three irrotational capillary-gravity waves in a system of finite depth is given by the linear dispersion relation

$$\omega_i^2 = \left(g|\boldsymbol{k}_i| + T|\boldsymbol{k}_i|^3\right) \tanh |\boldsymbol{k}_i|h \tag{2.3}$$

where g is the gravitational acceleration, $T = \frac{T'}{\rho}$, (T' being the coefficient of surface tension), ρ the density of and h the depth of, the fluid. Here i=1,2,3.

It is equations (2.1), (2.2) and (2.3) that now constitute the set we refer to as the

resonance conditions for capillary-gravity waves.

2.1.2 Second-harmonic resonance.

The problem we are going to consider is that of second-harmonic resonance amongst standing capillary-gravity waves with external Faraday excitation. Here a vertical oscillation of small amplitude is incorporated into the system such that the system is driven at the second-harmonic. The resonance conditions can only be satisfied only for specific wave-numbers and frequencies and for second-harmonic resonance the two further conditions

$$\boldsymbol{k}_1 = \boldsymbol{k}_2$$

$$\omega_1 = \omega_2,$$

are imposed. This gives the wave-number, $\boldsymbol{k}_3$, and frequency, ω_3, of the generated wave as $2\boldsymbol{k}_1$ and $2\omega_1$ respectively and leads to the resonance conditions

$$\boldsymbol{k}_1 = \boldsymbol{k}_2 = \frac{1}{2}\boldsymbol{k}_3, \tag{2.4}$$

$$\omega_1 = \omega_2 = \frac{1}{2}\omega_3, \tag{2.5}$$

$$\omega_i^2 = \left(g|\boldsymbol{k}_i| + T|\boldsymbol{k}_i|^3\right)\tanh|\boldsymbol{k}_i|h \qquad (i = 1, 3), \tag{2.6}$$

the wave with wavenumber $\boldsymbol{k}_1$ and frequency ω_1 is now identical to the wave with wave-number $\boldsymbol{k}_2$ and frequency ω_2.

As the above resonance is only a two wave interaction, $\boldsymbol{k}_2$ and ω_2 may be ignored.

2.1.3 Near resonance

The equations (2.4), (2.5) and (2.6) represent the case of exact second-harmonic resonance, but problems of near resonance may also be considered. If as in the case of exact resonance the wave-numbers remain related by $\boldsymbol{k}_3 = 2\boldsymbol{k}_1$, but we allow a small frequency mis-match to be incoporated into equation (2.5), the near-resonance condition becomes

$$\omega_3 - 2\omega_1 = \varepsilon\Delta_3, \tag{2.7}$$

where ε represents a small parameter and Δ_3 an $0(1)$ frequency mis-match parameter.

2.1.4 The dynamical equations.

As the motion of the fluid is irrotational, there exists a velocity potential, $\phi(x, y, z, t)$, related to the velocity $\mathbf{u}$ of the fluid by

$$\mathbf{u} = \nabla\phi.$$

As the fluid is assumed incompressible, the velocity potential must satisfy Laplace's equation

$$\nabla^2\phi = 0 \qquad\qquad -h \leq z \leq \zeta,$$

within the fluid, where h is the depth of the fluid and $\zeta(x, y, t)$ is the elevation of the fluid surface, with z the vertical coordinate.

As the fluid is of finite depth h, we have the bottom boundary condition

$$\frac{\partial \phi}{\partial z} = 0 \qquad\qquad (z = -h).$$

This boundary condition becomes

$$\phi, \frac{\partial \phi}{\partial z} \to 0 \qquad\qquad (z \to -\infty)$$

for the infinite depth case.

There are still two more boundary conditions needed to set up the problem. These are the dynamic boundary condition and the kinematic boundary condition. The dynamic boundary condition is derived from the Bernoulli equation, with the pressure above the fluid surface assumed to be zero. By considering the continuity of the pressure across the free surface, (McGoldrick (1965)), and with the introduction of external forcing, (e.g. Nagata (1989)), the dynamic boundary condition at the free surface may be written as

$$\frac{\partial \phi}{\partial t} + \frac{1}{2}|\nabla \phi|^2 + g\zeta - f\cos\Omega t.\zeta + \mathrm{p} = 0 \qquad (z = \zeta),$$

where $\mathrm{p} = -T\kappa(x, y, t)$ and κ is the surface curvature. Since $\kappa = \nabla \cdot \boldsymbol{n}$, where $\boldsymbol{n}$ is the unit normal to the free surface $z = \zeta(x, y, t)$,

$$\kappa = \nabla \cdot \left(\frac{\nabla \mathrm{f}}{|\nabla \mathrm{f}|} \right)$$

with $\mathrm{f}(x, y, t) = \zeta(x, y) - z$. For small amplitude waves, κ may be approximated by conditions at the mean level $z = 0$. Thus

$$\kappa \simeq \nabla^2 \zeta,$$

giving the condition at the free surface as

$$\frac{\partial \phi}{\partial t} + \frac{1}{2}|\nabla \phi|^2 + g\zeta - f\cos\Omega t.\zeta - T\nabla^2\zeta = 0 \qquad (z = \zeta). \tag{2.8}$$

Here f is the acceleration of the forcing, and Ω is the frequency of the forcing oscillation.

The condition that $(z-\zeta)$ vanish following a particle located on the surface, leads to the kinematic boundary condition

$$\frac{\partial \zeta}{\partial t} - \frac{\partial \phi}{\partial z} + \nabla\phi.\nabla\zeta = 0 \qquad (z = \zeta). \tag{2.9}$$

It is the two equations, (2.8) and (2.9), that contain all non-linear terms arising in the following perturbation analysis.

2.2 Construction of the evolution equations.

2.2.1 Expansion of the dynamic and kinematic boundary conditions.

For simplicity, we restrict attention to two-dimensional motion by omitting the y-co-ordinate. The two boundary conditions (2.8) and (2.9) are expanded in a Taylor series about $z = 0$, and truncating the expansions at $0(\varepsilon^2)$, where ε is a measure of wave slope, we obtain

$$(\phi_t + \zeta.\phi_{zt}) + \frac{1}{2}|\nabla\phi|^2 + g\zeta - f\cos\Omega t.\zeta - T\nabla^2\zeta + O(\varepsilon^3) = 0, \tag{2.10}$$

where $\zeta, \nabla\phi$ are assumed $0(\varepsilon)$,

for the dynamic boundary condition, and

$$\zeta_t - (\phi_z + \zeta\phi_{zz}) + \zeta_x\phi_x + O(\varepsilon^3) = 0, \tag{2.11}$$

for the kinematic boundary condition. Both are evaluated at $z = 0$.

(Here the subscripts represent differentiation with respect to the appropriate variables.)

Next the velocity potential, $\phi = \phi(x, z, t)$, and the surface elevation, $\zeta = \zeta(x, t)$, are expanded in terms of the small parameter ε, again to second order, as

$$\phi = \varepsilon\phi^{(1)} + \varepsilon^2\phi^{(2)} + O(\varepsilon^3), \tag{2.12}$$

$$\zeta = \varepsilon\zeta^{(1)} + \varepsilon^2\zeta^{(2)} + O(\varepsilon^3). \tag{2.13}$$

A long time-scale, $T \cong \varepsilon t$, is now introduced in such a way that

$$\frac{\partial}{\partial t} \to \frac{\partial}{\partial t} + \varepsilon\frac{\partial}{\partial T}, \tag{2.14}$$

then substituting (2.12), (2.13) and (2.14) into (2.10) and (2.11), we obtain the $O(\varepsilon)$ equations for the kinematic and dynamic boundary conditions as

$$\zeta_t^{(1)} - \phi_z^{(1)} = 0 \qquad z = 0, \tag{2.15}$$

$$\phi_t^{(1)} + g\zeta^{(1)} - T\nabla^2\zeta^{(1)} = 0 \qquad z = 0. \tag{2.16}$$

Similarly, the $O(\varepsilon^2)$ equations become

$$\zeta_t^{(2)} + \zeta_T^{(1)} - \phi_z^{(2)} - \zeta^{(1)}\phi_{zz}^{(1)} + \zeta_x^{(1)}\phi_x^{(1)} = 0, \tag{2.17}$$

$$\phi_t^{(2)} + \phi_T^{(1)} + \zeta^{(1)}\phi_{zt}^{(1)} + \frac{1}{2}|\nabla\phi^{(1)}|^2 + g\zeta^{(2)} - f\cos\Omega t.\zeta^{(1)} - T\nabla^2\zeta^{(2)} = 0, \quad (2.18)$$

again both evaluated at $z = 0$, where $f = O(\varepsilon)$ for the problem concerned.

To first order, the surface elevation and velocity potential for 2-D second-harmonic standing gravity-capillary waves are known to have the form

$$\zeta^{(1)} = \mathrm{Re}[A_1 \cos kx.e^{i\omega_1 t} + A_2 \cos 2kx.e^{i\omega_2 t}] \quad (2.19)$$

and

$$\phi^{(1)} = \mathrm{Re}\left[\frac{\omega_1}{k}a_1\frac{\cosh k(z+h)}{\sinh kh}\cos kx.e^{i\omega_1 t} + \frac{\omega_2}{2k}a_2\frac{\cosh 2k(z+h)}{\sinh 2kh}\cos 2kx.e^{i\omega_2 t}\right], \quad (2.20)$$

respectively, where A_i and a_i, $(i = 1, 2)$ represent complex amplitudes and exact second-harmonic resonance is assumed for the wave-numbers. Also ω_3, used previously, is now replaced by ω_2.

We now seek a connection between the A_i and a_i through the linearized first order equations (2.15) and (2.16). If the surface elevation (2.19) and the velocity potential (2.20) are substituted into the linear equation for the kinematic boundary condition (2.15), then the resulting equation is

$$\mathrm{Re}\left[i\omega_1 A_1 \cos kx.e^{i\omega_1 t} + i\omega_2 A_2 \cos 2kx.e^{i\omega_2 t}\right] =$$

$$\mathrm{Re}\left[\omega_1 a_1 \cos kx.e^{i\omega_1 t} + \omega_2 a_2 \cos 2kx.e^{i\omega_2 t}\right].$$

Comparing terms in $\cos kx.e^{i\omega_1 t}$ and terms in $\cos 2kx.e^{i\omega_2 t}$, we then get the two

relations

$$iA_1 = a_1 \qquad \text{and} \qquad iA_2 = a_2,$$

which can be substituted back into (2.19).

Similarly, substitution of (2.19) and (2.20) into (2.16) leads to the linear dispersion relation (2.3).

The new form of (2.19), and (2.20), are now substituted into (2.17) to give

$$\zeta_t^{(2)} - \phi_z^{(2)} = \mathrm{Re}\left[i\dot{a}_1 \cos kx.e^{i\omega_1 t} + i\dot{a}_2 \cos 2kx.e^{i\omega_2 t}\right]$$

$$-\mathrm{Re}\left[ia_1 \cos kx.e^{i\omega_1 t} + ia_2 \cos 2kx.e^{i\omega_2 t}\right] \times \mathrm{Re}\left[\frac{\omega_1 k a_1}{\tanh kh} \cos kx.e^{i\omega_1 t}\right.$$

$$\left.+\frac{2\omega_2 k a_2}{\tanh 2kh} \cos 2kx.e^{i\omega_2 t}\right] + \mathrm{Re}\left[ia_1 k \sin kx.e^{i\omega_1 t} + 2ia_2 k \sin 2kx.e^{i\omega_2 t}\right] \times$$

$$\mathrm{Re}\left[\frac{\omega_1 a_1}{\tanh kh} \sin kx.e^{i\omega_1 t} + \frac{\omega_2 a_2}{\tanh 2kh} \sin 2kh.e^{i\omega_2 t}\right],$$

where $\dot{a}_i$ represents differentiation of a_i with respect to time T.

We now re-arrange the above equation using the complex identity

$$\mathrm{Re}A \cdot \mathrm{Re}B = \frac{1}{2}\mathrm{Re}(AB + AB^*), \tag{2.21}$$

where $*$ represents the complex conjugate.

If the resulting expression is now expanded out, then keeping in only those terms possibly leading to resonance, (i.e terms multiplied by exponentials of the form $e^{\pm 2i\omega_1 t}$ and $e^{\pm i(\omega_1 - \omega_2)t}$, we obtain the following equation:

$$\zeta_t^{(2)} - \phi_z^{(2)} = \mathrm{Re}\left[i\dot{a}_1 \cos kx.e^{i\omega_1 t} + i\dot{a}_2 \cos 2kx.e^{i\omega_2 t}\right]$$

$$-\frac{1}{2}\mathrm{Re}\left[\frac{i\omega_1 k}{\tanh kh} {a_1}^2 \cos^2 kx.e^{2i\omega_1 t} + \frac{i\omega_1 k}{\tanh kh} a_1^* a_2 \cos kx \cos 2kx.e^{i(\omega_2 - \omega_1)t}\right.$$

$$+\frac{2i\omega_2 k}{\tanh 2kh}a_1 a_2^* \cos kx \cos 2kx.e^{i(\omega_1-\omega_2)t} - \frac{i\omega_1 k}{\tanh kh}{a_1}^2 \sin^2 kx.e^{2i\omega_1 t}$$
$$-\frac{i\omega_2 k}{\tanh 2kh}a_1 a_2^* \sin kx \sin 2kx.e^{i(\omega_1-\omega_2)t}$$
$$-\frac{2i\omega_1 k}{\tanh kh}a_1^* a_2 \sin kx \sin 2kx.e^{i(\omega_2-\omega_1)t}\Big]. \quad (2.22)$$

Using trigonometric formulae to combine the trigonometric products in equation (2.22), and eliminating all remaining terms not giving rise to the forms $\cos kx.e^{\pm i\omega_1 t}$ or $\cos 2kx.e^{\pm i\omega_2 t}$, (remembering $\omega_2 = 2\omega_1$), the expression further simplifies to

$$\zeta_t^{(2)} - \phi_z^{(2)} = \mathrm{Re}\left[i\dot{a}_1 \cos kx.e^{i\omega_1 t} + i\dot{a}_2 \cos 2kx.e^{i\omega_2 t}\right]$$
$$-\mathrm{Re}\Big[\frac{i\omega_1 k}{4\tanh kh}{a_1}^2 \cos 2kx.e^{2i\omega_1 t} + \frac{i\omega_1 k}{4\tanh kh}a_1^* a_2 \cos kx.e^{i(\omega_2-\omega_1)t}$$
$$-\frac{i\omega_2 k}{2\tanh 2kh}a_1^* a_2 \cos kx.e^{-i(\omega_1-\omega_2)t} - \frac{i\omega_1 k}{4\tanh kh}{a_1}^2 \cos 2kx.e^{2i\omega_1 t}$$
$$+\frac{i\omega_2 k}{4\tanh 2kh}a_1^* a_2 \cos kx.e^{-i(\omega_1-\omega_2)t} - \frac{i\omega_1 k}{2\tanh kh}a_1^* a_2 \cos kx.e^{i(\omega_2-\omega_1)t}\Big]. \quad (2.23)$$

Next the near resonance condition $\omega_2 = 2\omega_1 + \varepsilon\Delta_3$ is substituted into equation (2.23) and, after decomposing the resulting expression into two separate equations that represent the first harmonic and the second harmonic, we are left with

$$\zeta_{1t}^{(2)} - \phi_{1z}^{(2)} = -\mathrm{Re}\left[\left(i\dot{a}_1 + \left(-\frac{i\omega k a_1^* a_2}{4\tanh kh} - \frac{i\omega k a_1^* a_2}{2\tanh 2kh}\right)e^{i\varepsilon\Delta_3 t}\right)\cos kx.e^{i\omega t}\right] \quad (2.24)$$

and

$$\zeta_{2t}^{(2)} - \phi_{2z}^{(2)} = \mathrm{Re}\left[\left(i\dot{a}_2 e^{i\varepsilon\Delta_3 t} - \frac{i\omega k {a_1}^2}{2\tanh kh}\right)\cos 2kx.e^{2i\omega t}\right], \quad (2.25)$$

where the subscripts 1 and 2 represent the first and second harmonics respectively, and the frequency ω_1 has simply been expressed as ω.

The above two equations were obtained from the second-order approximation for the kinematic boundary condition. A similar process now has to be undertaken for the second-order equation for the dynamic boundary condition, (2.18). So, substituting equations (2.19) and (2.20) into (2.18), we obtain the following expression:

$$\begin{aligned}\phi_t^{(2)} + g\zeta^{(2)} - T\nabla^2\zeta^{(2)} = &-\mathrm{Re}\left[\frac{\omega_1}{k\tanh kh}\dot{a}_1\cos kx.e^{i\omega_1 t} + \frac{\omega_2}{2k\tanh 2kh}\dot{a}_2\cos 2kx.e^{i\omega_2 t}\right] \\ &+\mathrm{Re}\left[ia_1\cos kx.e^{i\omega_1 t} + ia_2\cos 2kx.e^{i\omega_2 t}\right]\times\mathrm{Re}\left[i\omega_1^2 a_1\cos kx.e^{i\omega_1 t} + i\omega_2^2 a_2 cos2kx.e^{i\omega_2 t}\right] \\ &-\frac{1}{2}\Bigg[\left[\mathrm{Re}\left[-\frac{\omega_1 a_1}{\tanh kh}\sin kx.e^{i\omega_1 t} - \frac{\omega_2 a_2}{\tanh 2kh}\sin 2kx.e^{i\omega_2 t}\right]\right]^2 \\ &+\left[\mathrm{Re}\left[\omega_1 a_1\cos kx.e^{i\omega_1 t} + \omega_2 a_2\cos 2kx.e^{i\omega_2 t}\right]\right]^2\Bigg] \\ &-f\cos\Omega t.\mathrm{Re}\left[ia_1\cos kx.e^{i\omega_1 t} + ia_2\cos 2kx.e^{i\omega_2 t}\right].\end{aligned}$$

Now repeating the same process as before, using the complex relation (2.21), expanding, and simplifying using trigonometric formulae, then discarding the non-resonant terms, we are left with

$$\begin{aligned}\phi_t^{(2)} + g\zeta^{(2)} - T\nabla^2\zeta^{(2)} = &-\mathrm{Re}\Bigg[\frac{\omega}{k\tanh kh}\dot{a}_1\cos kx.e^{i\omega_1 t} \\ &+\frac{\omega}{k\tanh 2kh}\dot{a}_2\cos 2kx.e^{2i\omega t}e^{i\varepsilon\Delta_3 t}\Bigg] + \mathrm{Re}\Bigg[-\frac{\omega^2 {a_1}^2}{4}\cos 2kx.e^{2i\omega t} \\ &+\frac{\omega^2 a_1^* a_2}{4}\cos kx.e^{i\omega t}.e^{i\varepsilon\Delta_3 t} + \omega a_1^* a_2\cos kx.e^{i\omega t}.e^{i\varepsilon\Delta_3 t} + \frac{\omega^2 a_1^2}{8\tanh^2 kh}\cos 2kx.e^{2i\omega t} \\ &-\frac{\omega^2 a_1^* a_2}{4\tanh 2kh\tanh kh}\cos kx.e^{i\omega t}e^{i\varepsilon\Delta_3 t} - \frac{\omega^2 a_1^* a_2}{4\tanh kh\tanh 2kh}\cos kh.e^{i\omega t}.e^{i\varepsilon\Delta_3 t}\end{aligned}$$

$$-\frac{\omega^2 a_1^2}{8}\cos 2kx.e^{2i\omega t} - \frac{\omega^2 a_1^* a_2}{4}\cos kx.e^{i\omega t}.e^{i\varepsilon\Delta_3 t} - \frac{\omega^2 a_1^* a_2}{4}\cos kx.e^{i\omega t}.e^{i\varepsilon\Delta_3 t}\Big]$$
$$-f\cos\Omega t.\mathrm{Re}\left[ia_1\cos kx.e^{i\omega t} + ia_2\cos 2kx.e^{2i\omega t}.e^{i\varepsilon\Delta_3 t}\right].$$

This equation can also be split into two parts, giving an equation for the first harmonic and the second harmonic. These two equations are

$$\phi_{1t}^{(2)} + g\zeta_1^{(2)} - T\nabla^2\zeta_1^{(2)} = \mathrm{Re}\Big[\Big(-\frac{\omega}{k\tanh kh}\dot{a}_1$$
$$-\frac{\omega^2 a_1^* a_2}{2\tanh 2kh\tanh kh}e^{i\varepsilon\Delta_3 t} + \frac{3\omega^2 a_1^* a_2}{4}e^{i\varepsilon\Delta_3 t} - f\cos\Omega t.ia_1\Big)\cos kx.e^{i\omega t}\Big] \quad (2.26)$$

and

$$\phi_{2t}^{(2)} + g\zeta_2^{(2)} - T\nabla^2\zeta_2^{(2)} = \mathrm{Re}\Big[\Big(-\frac{\omega\dot{a}_2}{k\tanh 2kh}e^{i\varepsilon\Delta_3 t} - \frac{3\omega^2 {a_1}^2}{8}$$
$$+\frac{\omega^2 a_1^2}{8\tanh^2 kh} - f\cos\Omega t.ia_2\Big)\cos 2kx.e^{2i\omega t}\Big], \quad (2.27)$$

respectively.

2.2.2 Combining the dynamic and kinematic boundary expansions.

The four equations (2.24) to (2.27), can be looked upon as two sets of two equations, with (2.24) and (2.26) representing the first harmonic and, (2.25) and (2.27) representing the second harmonic. The next stage in the analysis is to now combine each set into one expression.

Before this is done the exact forcing frequencies have to be inserted into the above equations. As in the relationship between ω_1 and ω_2, we allow a slight

forcing mis-match to occur. When the forcing is close to twice the first harmonic frequency we let $\Omega = 2\omega_1 + \varepsilon\Delta_1$ and substitution of this into the forcing term in (2.26) gives

$$f\cos(2\omega_1 + \varepsilon\Delta_1)t.A_1.\cos kx.e^{i\omega_1 t}.$$

Next using the relation

$$\cos(2\omega_1 + \varepsilon\Delta_1)t = \frac{1}{2}\left(e^{i(2\omega_1+\varepsilon\Delta_1)t} + e^{-i(2\omega_1+\varepsilon\Delta_1)t}\right)$$

we obtain the expression

$$fA_1.\cos kx.\frac{1}{2}\left(e^{i(3\omega_1+\varepsilon\Delta_1)t} + e^{-i(\omega_1+\varepsilon\Delta_1)t}\right)$$

and as only the real part of this expression is required we can take the complex conjugate without loss. The only resonant term in (2.26) arising from forcing is therefore

$$\frac{1}{2}fA_1^* e^{i\varepsilon\Delta_1 t}\cos kx.e^{i\omega_1 t}, \tag{2.28}$$

with no such terms present in (2.27).

For the separate case of forcing close to twice the frequency of the second-harmonic, we must now let $\Omega = 2\omega_2 + \varepsilon\Delta_2$. This results in the forcing term in the first harmonic equation being ignored and that in (2.27), $f\cos\Omega t.A_2.\cos 2kx.e^{i\omega_2 t}$, becoming

$$\frac{1}{2}fA_2^* e^{i\varepsilon\Delta_2 t}.\cos 2kx.e^{i\omega_2 t}. \tag{2.29}$$

Returning back to the first-harmonic equation (2.26), we find that after the insertion of the forcing term (2.28), differentiation with respect to time and the substitution of $\zeta_{1t}^{(2)}$ from equation (2.24), (2.27) then becomes

$$\phi_{1tt}^{(2)} + g\phi_{1z}^{(2)} - T\nabla^2\phi_{1z}^{(2)} = \mathrm{Re}\Big[\Big(-\frac{i\omega^2}{k\tanh kh}\dot{a}_1 + \Big(\frac{3i\omega^3}{4} - \frac{i\omega^3}{2\tanh 2kh\tanh kh}\Big)e^{i\varepsilon\Delta_3 t}a_1^* a_2 - \frac{\omega f a_1^*}{2}e^{i\Delta_1 t}\Big)\cos kx.e^{i\omega t}\Big] - \Big(g + k^2T\Big).\mathrm{Re}\left[\left(ia_1 + \left(\frac{i\omega k}{4\tanh kh} + \frac{i\omega k}{\tanh 2kh}\right)a_1^* a_2.e^{i\varepsilon\Delta_3 t}\right)\cos kx.e^{i\omega t}\right] \quad (2.30)$$

This equation may be further simplified using the linear dispersion relation (2.3). For the first harmonic the dispersion relation is

$$\omega^2 = \Big(g + Tk^2\Big)\,k.\tanh kh,$$

and when substituted into equation (2.30), this yields

$$\phi_{1tt}^{(2)} + g\phi_{1z}^{(2)} - T\nabla^2\phi_{1z}^{(2)} = \mathrm{Re}\Big[\Big(-\frac{2i\omega^2}{k\tanh kh}\dot{a}_1 + \Big(\frac{3i\omega^3}{4} - \frac{i\omega^3}{\tanh 2kh\tanh kh}\Big)e^{i\varepsilon\Delta_3 t}a_1^* a_2 - \frac{\omega f a_1^*}{2}e^{i\Delta_1 t}\Big)\cos kx.e^{i\omega t}\Big] - \mathrm{Re}\left[\left(\left(\frac{i\omega^3}{4\tanh^2 kh}\right)a_1^* a_2 e^{i\varepsilon\Delta_3 t}\right)\cos kx.e^{i\omega t}\right]. \quad (2.31)$$

Similarly with use of the second-harmonic frequency relation

$$2\omega^2 = \Big(g + 4Tk^2\Big)\,k.\tanh 2kh + 0(\varepsilon),$$

the same process yields

$$\phi_{2tt}^{(2)} + g\phi_{2z}^{(2)} - T\nabla^2\phi_{2z}^{(2)} = \mathrm{Re}\Big[\Big(-\frac{4i\omega^2}{k\tanh 2kh}\dot{a}_2 e^{i\varepsilon\Delta_3 t}$$

$$+\left(\frac{i\omega^3}{4\tanh^2 kh} - \frac{3i\omega^3}{4}\right)a_1^2 - \omega f a_2^*.e^{i\varepsilon\Delta_2 t}\Big)\cos 2kx.e^{2i\omega t}\Big]$$
$$+\mathrm{Re}\left[\left(\frac{i\omega^3 a_1^2}{\tanh 2kh\tanh kh}\right)\cos 2kx.e^{2i\omega t}\right] \tag{2.32}$$

after the forcing term (2.29) has been substituted back into the second-harmonic equation (2.27).

If the right hand sides of (2.31) and (2.32) are now equated to zero, so that secular growth may be eliminated, and hyperbolic identities used, the following equations are then obtained:

$$\dot{a}_1 = -\frac{\omega k}{4}\left(\frac{\cosh 2kh + 2}{\sinh 2kh}\right)a_1^* a_2.e^{i\varepsilon\Delta_3 t}$$
$$+\frac{ikf\tanh kh}{4\omega}a_1^*.e^{i\varepsilon\Delta_1 t} \tag{2.33}$$

and

$$\dot{a}_2 = \frac{\omega k}{8}\left(\frac{\tanh 2kh(\cosh 2kh + 2)}{\cosh 2kh - 1}\right)a_1^2.e^{-i\varepsilon\Delta_3 t} \tag{2.34}$$

when the forcing at the first harmonic, and

$$\dot{a}_1 = -\frac{\omega k}{4}\left(\frac{\cosh 2kh + 2}{\sinh 2kh}\right)a_1^* a_2.e^{i\varepsilon\Delta_3 t} \tag{2.35}$$

and

$$\dot{a}_2 = \frac{\omega k}{8}\left(\frac{\tanh 2kh(\cosh 2kh + 2)}{\cosh 2kh - 1}\right)a_1^2.e^{-i\varepsilon\Delta_3 t}$$
$$+\frac{ifk\tanh 2kh}{4\omega}a_2^*.e^{i\varepsilon(\Delta_2-\Delta_3)t} \tag{2.36}$$

when the forcing at the second harmonic.

With $f = 0$, i.e. second-harmonic resonance with no forcing, the equations are equivalent to those derived by Nayfeh (1973) without an airstream; and for the case of no forcing, infinite depth and exact resonance, i.e. $h \to \infty$ and $\Delta_1 = \Delta_2 = \Delta_3 = 0$, they reduce to the equations derived by Simmons (1969) and McGoldrick (1970).

2.3 Reduction of forced second-harmonic standing wave equations.

2.3.1 The undamped equations.

Now that the two sets of equations, (2.33) and (2.34), and (2.35) and (2.36), have been derived for undamped second-harmonic standing waves, in a finite depth of liquid, being forced at either the first or second harmonic, the next thing to do is to reduce the equations into a form where they can be analysed. Before trying to examine the more difficult near-resonance case, we first restrict attention to the case of exact resonance, where $\Delta_1 = \Delta_2 = \Delta_3 = 0$. This then leaves us with the two sets of equations

$$\dot{a}_1 = \lambda_1 a_1^* a_2 + \mu a_1^* \tag{2.37}$$

$$\dot{a}_2 = \lambda_2 a_1^2 \tag{2.38}$$

and

$$\dot{a}_1 = \lambda_1 a_1^* a_2 \tag{2.39}$$

$$\dot{a}_2 = \lambda_2 a_1^2 + \mu a_2^* \tag{2.40}$$

where

$$\lambda_1 = -\frac{\omega k}{4}\left(\frac{\cosh 2kh + 2}{\sinh 2kh}\right),$$

$$\lambda_2 = \frac{\omega k}{8}\left(\frac{\tanh 2kh(\cosh 2kh + 2)}{\cosh 2kh - 1}\right)$$

and

$$\mu = \frac{ifk}{4\omega}$$

are just constants depending on the depth of the fluid. In all cases with $k, h > 0$, λ_1 is negative and λ_2 is positive.

The two sets of equations, (2.37) and (2.38), and (2.39) and (2.40), can be reduced into still simpler form. Setting

$$a_1 \equiv b_1, \qquad a_2 \equiv b_2 - \left(\frac{\mu}{\lambda_1}\right)$$

equations (2.37) and (2.38) reduce to

$$\dot{b}_1 = \lambda_1 b_1^* b_2 \tag{2.41}$$

and

$$\dot{b}_2 = \lambda_2 b_1^2 \tag{2.42}$$

respectively.

These two equations are now in the form of two coupled unforced, undamped, evolution equations whose properties have been extensively studied (e.g. McGoldrick (1970)) and will be re-examined in the next chapter.

The set of equations (2.39) and (2.40), however, provide us with more novel results. If we first use the substitutions

$$a_1 \equiv b_1 e^{i\frac{\pi}{8}}, \qquad a_2 \equiv b_2 e^{i\frac{\pi}{4}}, \qquad \mu \equiv \mu' e^{\frac{\pi}{2}},$$

these give the equations

$$\dot{b}_1 = \lambda b_1^* b_2 \qquad \text{and} \qquad \dot{b}_2 = \lambda_2 b_1^2 + \mu' b_2^*,$$

where μ' is the real quantity $\frac{fk}{4\omega}$. Next using the substitutions

$$b_1 \equiv \mu' \left(\frac{1}{-\lambda_1 \lambda_2}\right)^{\frac{1}{2}} B_1, \qquad\qquad b_2 \equiv \left(-\frac{\mu'}{\lambda_1}\right) B_2 \tag{2.43}$$

these two equations reduce to

$$\frac{dB_1}{dT_1} = -B_1^* B_2 \tag{2.44}$$

and

$$\frac{dB_2}{dT_1} = B_1^2 + B_2^* \tag{2.45}$$

respectively, where $T_1 = \mu' T$.

It is the two equations (2.44) and (2.45) that will form the nucleus of work in the next chapter.

Chapter 3

The second-harmonic resonance equations.

3.1 Investigation of the unforced, undamped equations.

3.1.1 The unforced solutions.

Simmons (1969) was the first to obtain a set of differential equations governing second-harmonic resonance using variational techniques. McGoldrick (1970) reconsidered this work by means of the asymptotic method of multiple time and space scales. Since these early studies much work has been done on the unforced system and here we revisit some of the key results in order to build up an

understanding of such systems.

The central equations for our study are the simple set of unforced evolution equations for exact second-harmonic resonance

$$\dot{A}_1 = -A_1^* A_2, \tag{3.1}$$

$$\dot{A}_2 = A_1^2. \tag{3.2}$$

Equations (3.1) and (3.2) are next expressed in polar form using the transformation

$$A_1 = r_1 \exp(i\phi_1), \tag{3.3}$$

$$A_2 = r_2 \exp(i\phi_2). \tag{3.4}$$

Substitution of (3.3) and (3.4) into (3.1) and (3.2), gives the system of equations

$$\frac{dr_1}{dt} = -r_1 r_2 \cos(\phi_2 - 2\phi_1), \tag{3.5}$$

$$\frac{dr_2}{dt} = r_1^2 \cos(\phi_2 - 2\phi_1), \tag{3.6}$$

$$\frac{d\phi_1}{dt} = -r_2 \sin(\phi_2 - 2\phi_1), \tag{3.7}$$

$$\frac{d\phi_2}{dt} = -\frac{r_1^2}{r_2} \sin(\phi_2 - 2\phi_1), \tag{3.8}$$

after real and imaginary parts have been equated. Combining (3.7) and (3.8) in such a way as to define a new variable Φ, the system (3.5)-(3.8) can be rewritten as

$$\frac{dr_1}{dt} = -r_1 r_2 \cos\Phi, \tag{3.9}$$

$$\frac{dr_2}{dt} = r_1^2 \cos\Phi, \tag{3.10}$$

$$\frac{d\phi_1}{dt} = -r_2 \sin\Phi, \tag{3.11}$$

$$\frac{d\Phi}{dt} = \left(2r_2 - \frac{r_1^2}{r_2}\right) \sin\Phi, \tag{3.12}$$

$$\Phi \equiv \phi_2 - 2\phi_1, \tag{3.13}$$

where (3.9), (3.10) and (3.12) form a closed 3-D system. Equation (3.11) may be solved afterwards for ϕ_1 and hence ϕ_2.

It can be seen from (3.9) and (3.10) that

$$\frac{d}{dt}(r_1^2 + r_2^2) = 0,$$

giving $r_1^2 + r_2^2$ as an invariant of the system. This means the energy in the system, $r_1^2 + r_2^2$, remains constant throughout time and the system is conservative.

It is also seen that

$$\frac{d}{dt}(r_1^2 r_2 \sin\Phi) = 0,$$

gives a second invariant.

Introducing

$$r_1^2 + r_2^2 \equiv E \tag{3.14}$$

$$r_1^2 r_2 \sin\Phi \equiv \Gamma \tag{3.15}$$

into the expression

$$\frac{dr_1^2}{dt} = -2r_1^2 r_2 \cos\Phi,$$

we obtain a single equation for $r_1^2(t)$,

$$\frac{dr_1^2}{dt} = -2(r_1^4(E - r_1^2) - \Gamma^2)^{\frac{1}{2}}. \tag{3.16}$$

With $z \equiv r_1^2$, this can be rewritten as

$$\frac{dz}{dt} = -2(z^2(E - z) - \Gamma^2)^{\frac{1}{2}}$$

and so

$$\int_0^z \frac{dz}{(-z^3 + Ez^2 - \Gamma^2)^{\frac{1}{2}}} = -2t + C,$$

which is expressed as

$$\int_0^z \frac{dz}{[-(z - z_1)(z - z_2)(z - z_3)]^{\frac{1}{2}}} = -2t + C. \tag{3.17}$$

Here z_1, z_2 and z_3 are roots of the cubic equation $z^3 - Ez^2 + \Gamma^2 = 0$ and satisfy the conditions

$$\begin{aligned} z_1 + z_2 + z_3 &= E, \\ z_1z_2 + z_1z_3 + z_2z_3 &= 0, \\ z_1z_2z_3 &= -\Gamma^2, \\ z_1 > z \geq z_2 &> z_3. \end{aligned}$$

The l.h.s of equation (3.17) is now in the form of an elliptic integral, and can be written as

$$\int_0^{z_1} \frac{dz}{[-(z - z_1)(z - z_2)(z - z_3)]^{\frac{1}{2}}} - \int_z^{z_1} \frac{dz}{[-(z - z_1)(z - z_2)(z - z_3)]^{\frac{1}{2}}} = -2t + c.$$

Using a handbook of elliptic integrals, Byrd and Friedman (1954), the above equation is expressed in terms of sn functions, i.e.

$$\mathrm{sn}^{-1}\left\{\left(\frac{z-z_1}{z_2-z_1}\right)^{\frac{1}{2}};k\right\} = (z_1-z_3)^{\frac{1}{2}}(t+c') + \mathrm{sn}^{-1}\left\{\left(\frac{z_1}{z_1-z_2}\right)^{\frac{1}{2}};k\right\}$$

where $c' = -\frac{c}{2}$. This gives

$$z = (z_2-z_1)\mathrm{sn}^2\{(z_1-z_3)^{\frac{1}{2}}(t+c') + \Xi; k\} + z_1,$$

where

$$\Xi = \mathrm{sn}^{-1}\left\{\left(\frac{z_1}{z_1-z_2}\right)^{\frac{1}{2}}\right\} \quad \text{and} \quad k^2 = \left(\frac{z_1-z_2}{z_1-z_3}\right).$$

3.1.2 Change of variables.

Another way of arriving at this elliptic integral form is to introduce the change of variables

$$X = r_2\cos\Phi, \tag{3.18}$$

$$Y = r_2\sin\Phi, \tag{3.19}$$

$$Z = r_1^2. \tag{3.20}$$

[c.f. Hughes and Proctor (1990)].

Substitution of (3.18)-(3.20) into the unforced equations (3.9)-(3.13), yields the system

$$\dot{X} = Z - 2Y^2, \tag{3.21}$$

$$\dot{Y} = 2XY, \tag{3.22}$$

$$\dot{Z} = -2XZ, \tag{3.23}$$

$$\dot{\phi}_1 = -Y, \tag{3.24}$$

$$\dot{\phi}_2 = \frac{ZY}{X^2+Y^2}, \tag{3.25}$$

where again $\Phi = \phi_2 - 2\phi_1$. The first three equations, (3.21)-(3.23), form a closed system which has a fixed point solution

$$X = 0, \qquad Y = \pm\left(\frac{E}{3}\right)^{\frac{1}{2}}, \qquad Z = \frac{2E}{3}. \tag{3.26}$$

This will be examined in detail later.

From (3.22) and (3.23) it follows that

$$\frac{d}{dt}(ZY) = 0,$$

which leads to the relation, [equivalent to (3.15)]

$$Y = \frac{\Gamma}{Z}. \tag{3.27}$$

Again Γ is a real constant.

Substitution of (3.27) into (3.21) yields

$$\frac{dX}{dt} = \frac{Z^3 - 2\Gamma^2}{Z^2}$$

and division by (3.23) gives

$$\frac{dX}{dZ} = -\frac{Z^3 - 2\Gamma^2}{2XZ^3} \qquad (X, Z \neq 0).$$

On separating the variables and integrating, we obtain

$$X^2 = -Z - \frac{\Gamma^2}{Z^2} + E \tag{3.28}$$

and since $\Gamma = YZ$, this gives energy equation

$$X^2 + Y^2 + Z = r_1^2 + r_2^2 = E,$$

where E is again the constant energy of the system.

On setting

$$X = \left(E - Z - \frac{\Gamma^2}{Z^2}\right)^{\frac{1}{2}},$$

from (3.28) and substituting into (3.23), we obtain

$$\frac{dZ}{dt} = -2(EZ^2 - Z^3 - \Gamma^2)^{\frac{1}{2}} \tag{3.29}$$

or

$$\frac{1}{2}\left(\frac{dZ}{dt}\right)^2 + \Pi(Z) = 0,$$

where

$$\Pi(Z) = 2(Z^3 - EZ^2 + \Gamma^2) = 2(Z - Z_1)(Z - Z_2)(Z - Z_3) \tag{3.30}$$

and $Z_1 \geq Z_2 \geq Z_3$ are real for the case concerned. Obviously, these are the same as the roots z_1, z_2 and z_3 above.

Here $\Pi(Z)$ can be thought of as analogous to 'potential energy' and $\frac{1}{2}\dot{Z}^2$ to a 'kinetic energy' of a conservative system with (3.16) being similarly interpreted. Since Z must be positive, from (3.20), E and Γ must be chosen in such a way

that Π has two positive roots and one negative root, thus enabling the solution to oscillate in the potential well between Z_1 and Z_2. From (3.30), we obtain

$$\Pi'(Z) = 2Z(3Z - 2E)$$

giving

$$Z = 0 \quad \text{and} \quad Z = \frac{2E}{3}$$

for $\Pi'(Z) = 0$.

Using the condition $\Pi(Z) \leq 0$, and taking the second root, gives

$$2\left(-\frac{4E^3}{27} + \Gamma^2\right) \leq 0,$$

or

$$\frac{27}{4}\Gamma^2 \leq E^3 \tag{3.31}$$

and this constrains the choice of E and Γ. If $\frac{27}{4}\Gamma^2 = E^2$, then we have equal roots and the solution corresponds to the fixed point (3.26), shown in figure (3.1). For more general E and Γ we get the form of solution as shown in figure (3.2).

Integration again yields result (3.17). Note also that the half period T of the oscillation between z_1 and z_2 is given by

$$T = \int_{Z_2}^{Z_1} \frac{dZ}{[-(Z - Z_1)(Z - Z_2)(Z - Z_3)]^{\frac{1}{2}}} = \frac{1}{(Z_1 - Z_3)^{\frac{1}{2}}} \mathrm{sn}^{-1}\left(1; \left(\frac{Z_1 - Z_2}{Z_1 - Z_3}\right)^{\frac{1}{2}}\right),$$

and the time period T_p of the Z-oscillation is $T_p = 2T$.

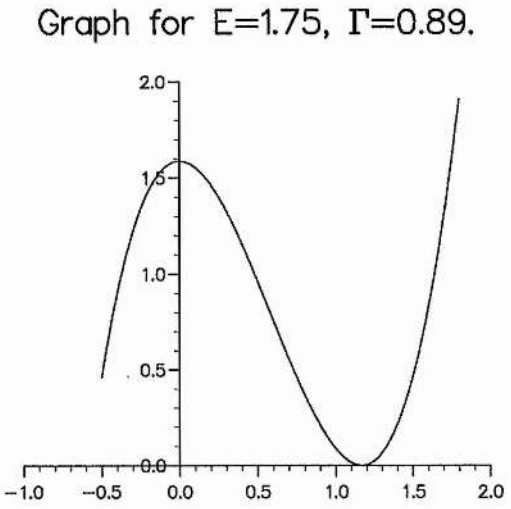

Figure 3.1: Graph showing the potential function $\Pi(x)$ when $E = 1.75$ and $\Gamma = 0.89$, for the case when $Z_1 = Z_2$.

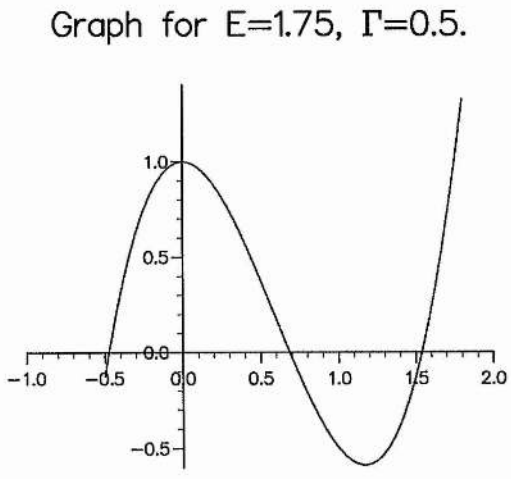

Figure 3.2: Graph showing a typical potential function $\Pi(x)$ when $E = 1.75$ and $\Gamma = 0.5$, where Z oscillates between the two larger roots Z_1 and Z_2.

3.2 The forced, undamped equations.

3.2.1 Forcing at the first harmonic.

Now that the behaviour of the unforced equations has been established, we can turn our attention to the corresponding evolution equations when the motion is subject to Faraday excitation. The most tractable case of this exists when the first-harmonic A_1 wave is subject to forcing, and the evolution equations become

$$\begin{aligned} \dot{A}_1 &= -A_1^* A_2 + A_1^* \\ \dot{A}_2 &= A_1^2. \end{aligned}$$

Here the system remains straightforward as the substitution

$$A_1 \equiv B_1, \qquad A_2 \equiv B_2 - 1$$

reduces the equations to

$$\begin{aligned} \dot{B}_1 &= -B_1^* B_2 \\ \dot{B}_2 &= B_1^2. \end{aligned}$$

This is now in the same form as the unforced system (3.1) and (3.2), [cf.(2.41),(2.42)] and solutions again exist in the form of elliptic integrals.

3.2.2 Forcing at the second harmonic.

A more complex case exists if we look at what happens when (3.1) and (3.2) are subjected to Faraday excitation at the second-harmonic. Here the A_2 wave is excited and the system becomes

$$\dot{A}_1 = -A_1^* A_2 \tag{3.32}$$

$$\dot{A}_2 = A_1^2 + A_2^*. \tag{3.33}$$

Unlike forcing at the first-harmonic, where the forcing term can be scaled out, the A_2^* term cannot be eliminated from the calculations. The resulting evolution equations are now irreducibly four dimensional and little analytical progress has yet been made. However, small inroads can be made by looking at special cases, but numerical work necessarily plays a large part in our study of these equations.

3.2.3 Cartesian representation.

With a simple cartesian representation

$$A_1 = x_1 + iy_1$$

$$A_2 = x_2 + iy_2,$$

equations (3.32) and (3.33) give the four real equations

$$\dot{x}_1 = -x_1 x_2 - y_1 y_2 \tag{3.34}$$

$$\dot{y}_1 = x_2 y_1 - x_1 y_2 \tag{3.35}$$

$$\dot{x}_2 = x_1^2 - y_1^2 + x_2 \tag{3.36}$$

$$\dot{y}_2 = 2x_1y_1 - y_2. \tag{3.37}$$

These are invariant under the following symmetry transformations

$$(x_1, y_1, x_2, y_2, t) \longleftrightarrow (-x_1, -y_1, x_2, y_2, t)$$

$$(x_1, y_1, x_2, y_2, t) \longleftrightarrow (-x_1, y_1, x_2, -y_2, t)$$

$$(x_1, y_1, x_2, y_2, t) \longleftrightarrow (y_1, x_1, -x_2, y_2, t)$$

$$(x_1, y_1, x_2, y_2, t) \longleftrightarrow (x_1, -y_1, x_2, -y_2, t)$$

$$(x_1, y_1, x_2, y_2, t) \longleftrightarrow (-y_1, x_1, -x_2, -y_2, t)$$

$$(x_1, y_1, x_2, y_2, t) \longleftrightarrow (y_1, -x_1, -x_2, -y_2, t)$$

$$(x_1, y_1, x_2, y_2, t) \longleftrightarrow \left(\frac{x_1 - y_1}{\sqrt{2}}, \frac{x_1 + y_1}{\sqrt{2}}, y_2, -x_2, -t\right)$$

$$(x_1, y_1, x_2, y_2, t) \longleftrightarrow \left(\frac{x_1 + y_1}{\sqrt{2}}, \frac{y_1 - x_1}{\sqrt{2}}, -y_2, x_2, -t\right)$$

and a consequence of these is that we need only look at initial values in one eighth of the (x_1, y_1) phase plane if (x_2, y_2) are arbitrary.

We next seek to isolate a few special solutions of (3.34), (3.35), (3.36) and (3.37) using specific values of initial data. In these cases, the system reduces to three or less dimensions. Even for these cases two distinct types of behaviour are found. Case 1 and case 2 below show unbounded solutions of the system, while case 3 shows bounded behaviour. Later, other initial values are considered numerically.

Case 1.

Here we examine the solution with initial conditions $x_1 = y_1 = 0$ (i.e. $A_1 = 0$). This corresponds to the system

$$\begin{aligned} \dot{x}_1 &= 0 \\ \dot{y}_1 &= 0 \\ \dot{x}_2 &= x_2 \\ \dot{y}_2 &= -y_2 \end{aligned}$$

from which it is clear that the A_1 wave remains zero for all time, while the A_2 wave is given by

$$A_2 = x_{20}e^t + iy_{20}e^{-t}. \tag{3.38}$$

Here the real part of the A_2 wave grows exponentially with time, while the imaginary part decays at the same rate. This is just the (near-trivial) case of a single, forced wave A_2.

Case 2.

When A_1 and A_2 are purely real, so that $y_{10} = y_{20} = 0$, this remains so for all times t. The system of equations is then

$$\begin{aligned} \dot{x}_1 &= -x_1x_2, \qquad (3.39) \\ \dot{y}_1 &= 0, \end{aligned}$$

$$\dot{x}_2 = x_1^2 + x_2, \tag{3.40}$$

$$\dot{y}_2 = 0.$$

Division of (3.40) by (3.39) gives

$$\frac{dx_2}{dx_1} = -\frac{x_1}{x_2} - \frac{1}{x_1} \qquad (x_1, x_2 \neq 0),$$

and letting $B_1 = A_1^2$ this equation becomes

$$2\frac{dx_2'}{dx_1'} = -\frac{1}{x_1'} - \frac{1}{x_2'}. \tag{3.41}$$

Equation (3.41) is of the same form as that studied by Craik, Nagata & Moroz (1992). It was found by Craik *et al* that $x_2' \to \infty$ as $t \to \infty$, while $x_1' \to 0$ as $t \to \infty$. Hence for our case, the real part of the A_2 wave tends to infinity as time tends to infinity, while the real part of the A_1 wave tends towards zero. For both waves the imaginary parts remain zero for all time. Corresponding solutions with A_1 pure imaginary and A_2 real, are obtained from the symmetry transformations.

Case 3.

In this case the A_1 wave has equal initial real and imaginary amplitudes, with the A_2 wave a purely imaginary amplitude i.e. $A_1 = a + ia$ and $A_2 = ib$. This then gives the set of equations

$$\dot{x}_1 = \dot{y}_1 = -x_1 y_2,$$

$$\dot{x}_2 = 0,$$

$$\dot{y}_2 = 2x_1^2 - y_2.$$

Here $x_1, y_1 \to 0$ and $y_2 \to 0$ as $t \to \infty$ and thus we have a bounded system in which both waves die as $t \to \infty$. An example of this is shown in figure (3.3).

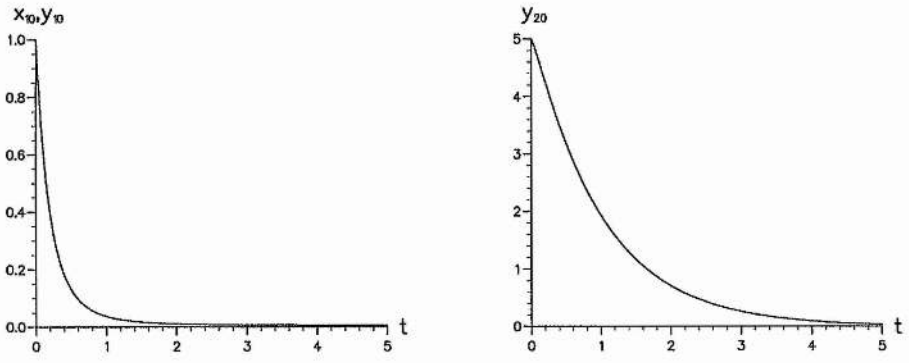

Figure 3.3: Degenerate solution for Case 3.

[It should be noted that the corresponding solutions for case 2 can be recovered using the negative time transformations].

3.2.4 Numerical results.

If we now proceed to look more closely at the cartesian system (3.34) to (3.37), it is seen that the solutions have a very complicated behaviour. In the previous section solutions have already been discovered for a few special cases, but a numerical approach is needed for more general initial data. With a numerical approach we are able to reveal further bounded solutions that appear to be periodic or

quasiperiodic in time. Here the amplitudes neither grow nor die away, but remain in a finite region of space and may exhibit space filling properties.

The properties of the system are first examined with the two real amplitudes (x_1, x_2) plotted against each other, and the two imaginary amplitudes (y_1, y_2) plotted likewise. Figures (3.4) to (3.12) show three seemingly distinct types of behaviour, with the final figure on each page showing the shape of the unforced system for the same initial data.

Figure (3.4) shows what seems to be a quasiperiodic orbit in real and imaginary space over a relatively short time evolution. After a slightly longer time, figure (3.5), it is clearly seen that the orbits exhibit space filling properties, with the solutions remaining bounded. If the time duration is then allowed to be much larger still, the orbits will maintain the shape depicted in (3.5), with the holes within the outer boundaries of the structure never filling in. Figure (3.6) compares the unforced and forced cases, with the forced system clearly shown to be a slight perturbation on the unforced system.

Looking now at a different set of initial data, we obtain a different form of bounded structure like that shown in figure (3.7). Here the spaces within the outer boundaries have clearly disappeared, and the structure takes on a more complicated appearance. Although figure (3.8) looks greatly different to figure (3.5), it is quite probable that they are both exhibiting the same type of behaviour, with any visual difference being due to initial conditions only. An examination

of the unforced equations, shown in figure (3.9), again suggests this may just be a perturbation of the unforced quasiperiodic motion.

A completely different type of behaviour is revealed by the unbounded growth represented in figure (3.10). Here the real amplitudes of the waves do successive semi-arcs of each half of the plane, with each being of greater radius than the last. In this case the amplitudes of the waves grow indefinitely, but it is noted that the imaginary part of the second wave appears to remain small in comparison to the rest of the amplitudes. This is highlighted particularly strongly as t gets large. In this case the unforced equations reveal a structure, figure (3.12), that bears no great resemblance to that of the unforced equations, as is to be expected when the former exhibits growth and the unforced system is a conservative one.

The evolution of the system is now described for a series of initial data in which only the x_1 value is changed. Increasing the value of x_1 in differing increments from 5 up to 3000, figures (3.13) to (3.20) clearly show the type of rich behaviour that system (3.34) to (3.37) exhibits, with figures (3.21) and (3.22) representing the unforced system for the specified initial data. In these diagrams it is seen how the system progresses from the unbounded state through a series of complex orbits to the bounded solution depicted in (3.20) for large x_1. This bounded solution closely resembles the unforced solution (3.21), with the linear terms in equations (3.36) and (3.37) becoming almost redundant at this large value of x_1. It is noted that the quasi-periodic orbits shown in figures (3.14) and (3.17) do

have space filling properties, but take a much longer time to show this than some of the other choices of initial data.

An interesting question arises over the behaviour of the system if initial data is chosen in a region where the trajectories do not penetrate. With data otherwise corresponding to that in figure (3.15), the initial value of y_2 is changed so that it coincides with the vacant area below the structure and figure (3.23) shows what happens if the corresponding y_2 value is negative. Here the right-hand diagram seems to have rotated by 180^o, while the left-hand one remains the same. This is not quite the case, as for this to happen the y_1 value would also need to take the negative value, as described by the fourth transformation in section 3.2.3. The fact that the initial value of y_1 is so close to zero in figures (3.15) and (3.23) means that the two diagrams have very similar trajectories, but if this value was allowed to increase this would not be the case. If the y_2 value now drops closer to that of y_1, unbounded growth again appears. Figure (3.24) shows what happens in this case and this state will exist for small negative or positive y_2.

Although interesting, these complex quasi-periodic orbits do not give us much mathematical information; but, by using a change of variable, see section 3.2.6, a much simpler system can be obtained. In this system diagrams are plotted for the corresponding initial data and this system will be looked at in more detail in due course.

3.2.5 Polar representation.

Another possible way forward is to transform the forced system of equations, (3.32) and (3.33), into a polar co-ordinate system. If we again use the polar transformation (3.3) and (3.4), as in section 1, we obtain

$$\frac{dr_1}{dt} = -r_1 r_2 \cos\Phi \tag{3.42}$$

$$\frac{dr_2}{dt} = r_1^2 \cos\Phi + r_2 \cos 2\phi_2 \tag{3.43}$$

$$\frac{d\Phi}{dt} = -\frac{r_1^2}{r_2}\sin\Phi + 2r_2 \sin\Phi - \sin 2\phi_2 \tag{3.44}$$

$$\frac{d\phi_1}{dt} = -r_2 \sin\Phi \tag{3.45}$$

where $\Phi = \phi_2 - 2\phi_1$.

This form is not as useful as for the unforced equations because the two phase variables cannot now be incorporated into a single variable Φ as before, and hence the problem remains strictly four dimensional. However it is helpful if we examine the energy of the system. From equations (3.42) and (3.43),

$$\frac{d}{dt}(r_1^2 + r_2^2) = 2r_2^2 \cos 2\phi_2$$

leading to the inequalities

$$-2(r_1^2 + r_2^2) \leq -2r_2^2 \leq \frac{d}{dt}(r_1^2 + r_2^2) \leq 2r_2^2 \leq 2(r_1^2 + r_2^2)$$

which give

$$(r_{10}^2 + r_{10}^2)e^{-2t} \leq r_1^2 + r_2^2 \leq (r_{10}^2 + r_{20}^2)e^{2t}. \tag{3.46}$$

This puts a bound on the energy growth of the system with time. Thus, the wave system cannot experience finite-time blow up, but any growth is bounded above by $E_0 e^{2t}$.

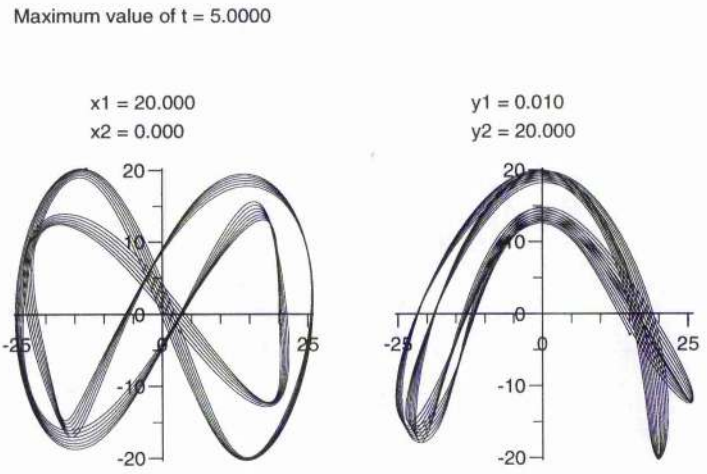

Figure 3.4: Short time evolution for the forced equations.

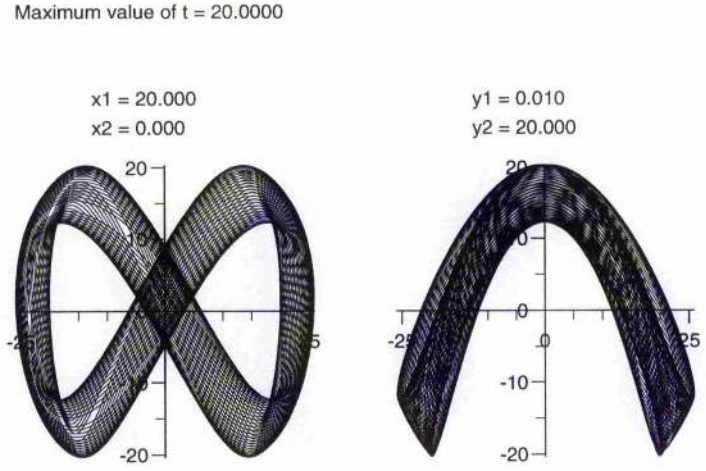

Figure 3.5: Long time evolution for the forced equations.

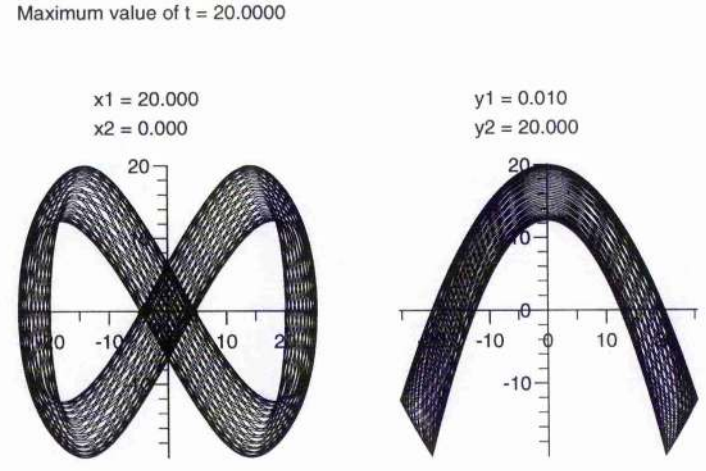

Figure 3.6: Long time evolution for the unforced equations.

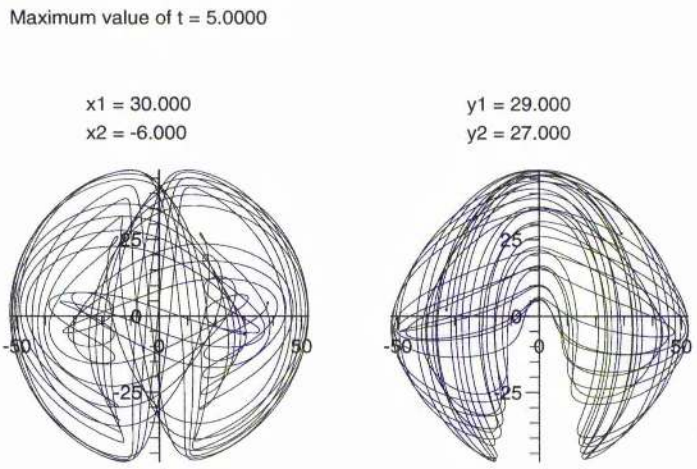

Figure 3.7: Short time evolution for the forced equations.

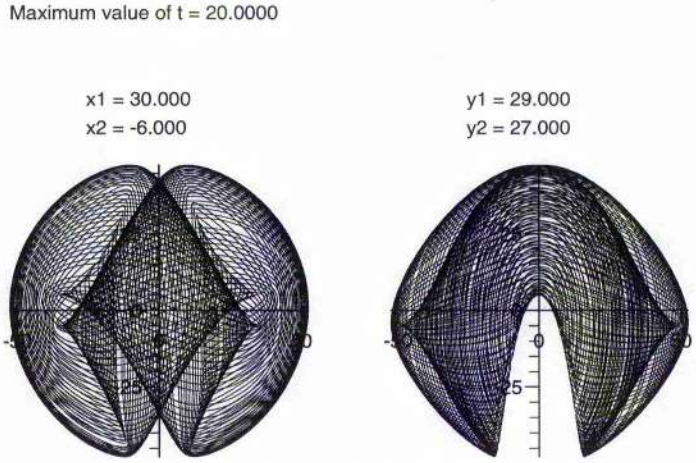

Figure 3.8: Long time evolution for the forced equations.

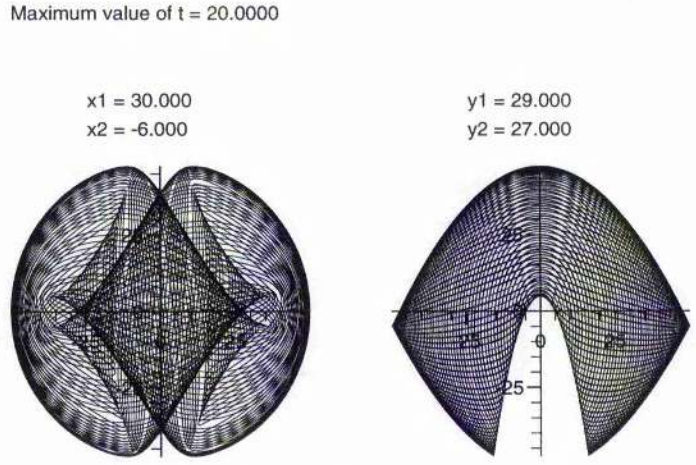

Figure 3.9: Long time evolution for the unforced equations.

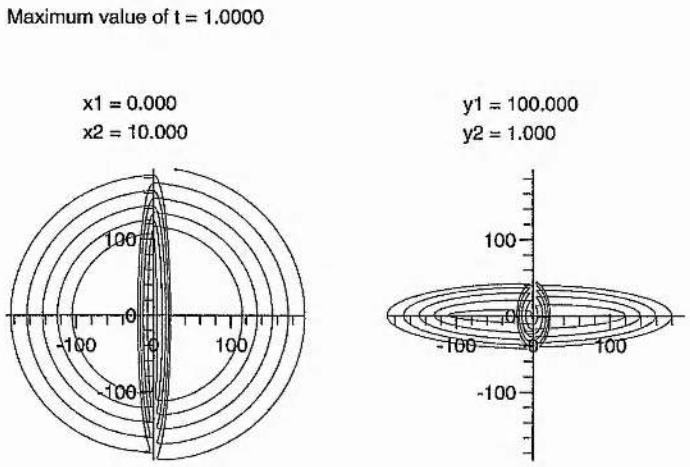

Figure 3.10: Time evolution for $t = 1$ of the forced equations.

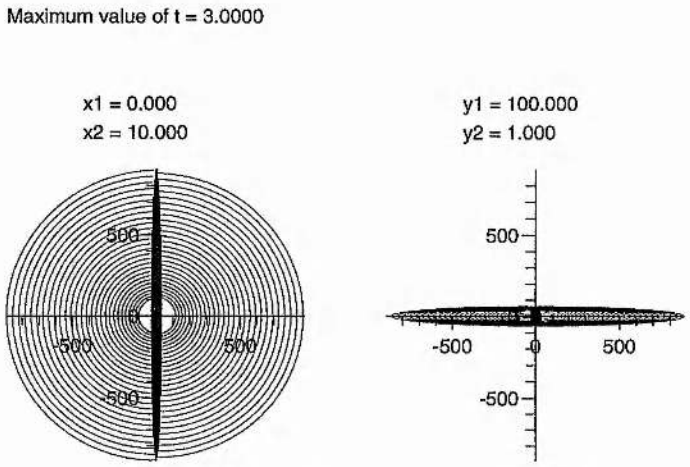

Figure 3.11: Time evolution for $t = 3$ of the forced equations.

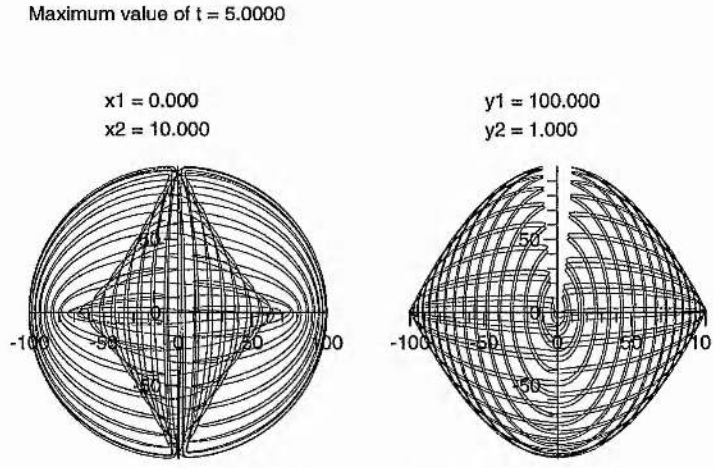

Figure 3.12: Time evolution for $t = 5$ of the unforced equations.

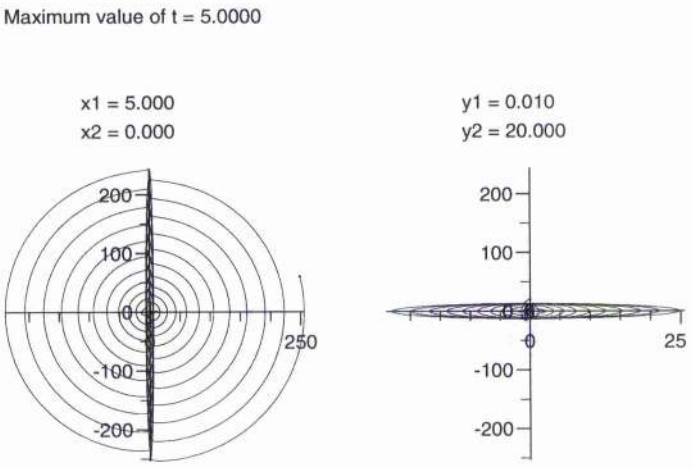

Figure 3.13: Time evolution for $t = 5$ for x1=5, y2=20.

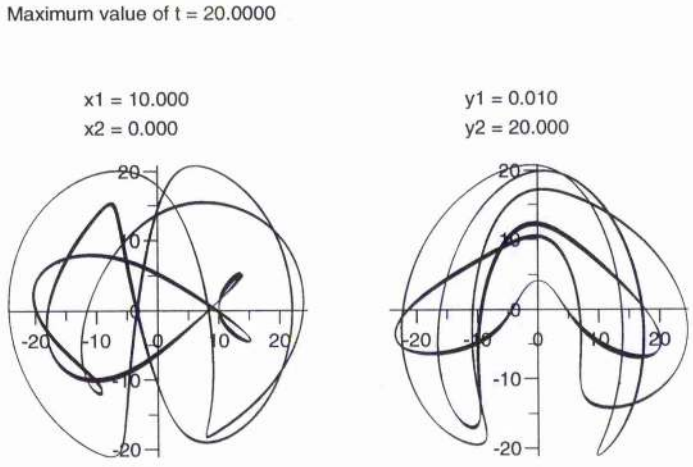

Figure 3.14: Time evolution for $t = 20$ for x1=10, y2=20.

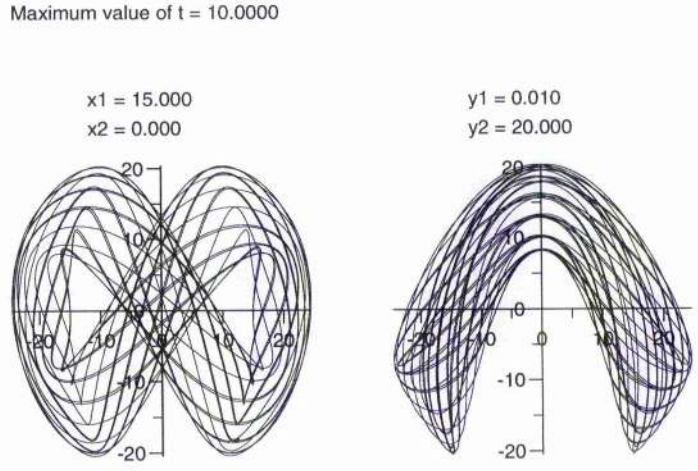

Figure 3.15: Time evolution for $t = 10$ for x1=15, y2=20.

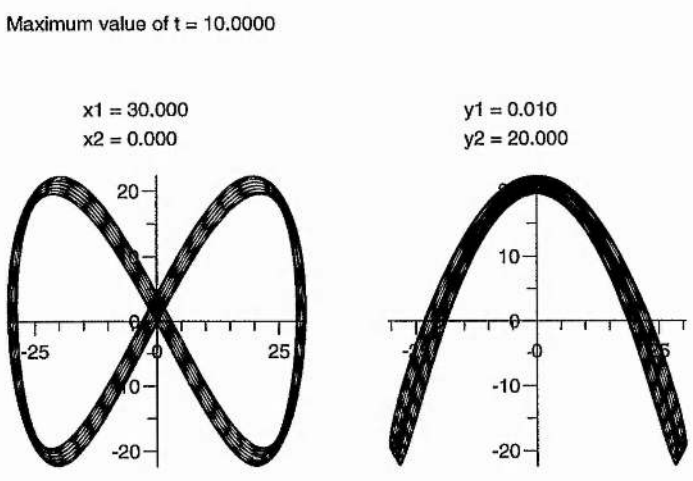

Figure 3.16: Time evolution for $t = 10$ for x1=30, y2=20.

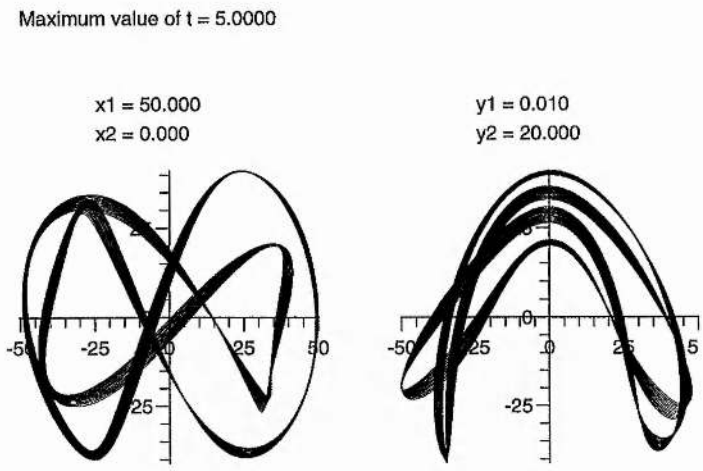

Figure 3.17: Time evolution for $t = 5$ for x1=50, y2=20.

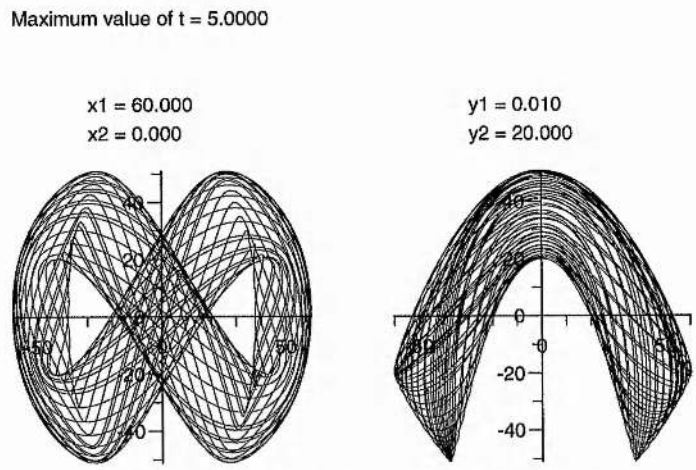

Figure 3.18: Time evolution for $t = 5$ for x1=60, y2=20.

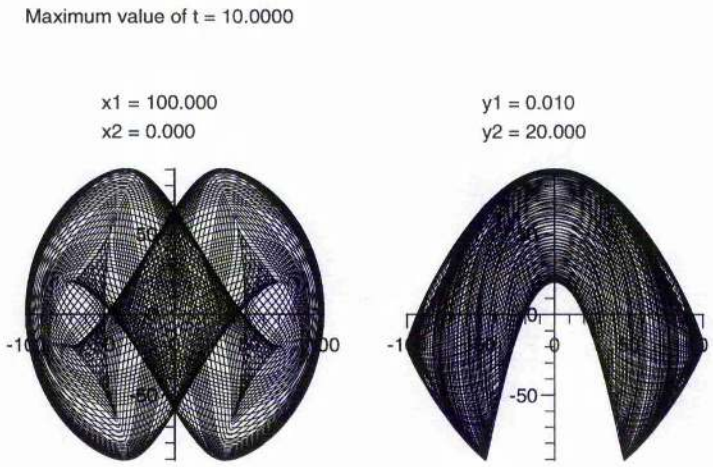

Figure 3.19: Time evolution for $t = 10$ for x1=100, y2=20.

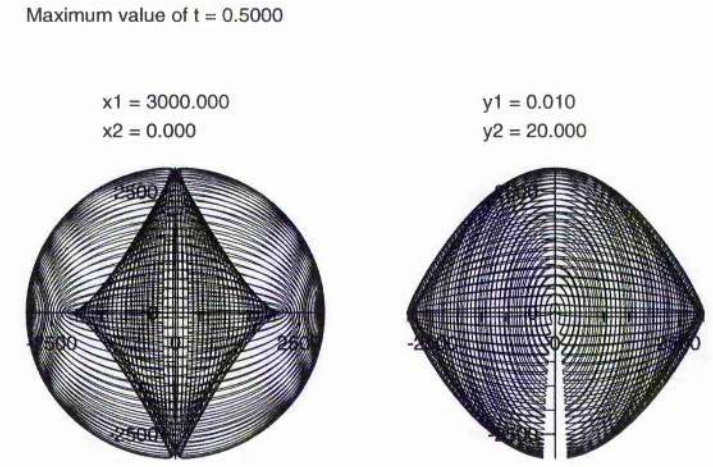

Figure 3.20: Forced solution for short time, large x1.

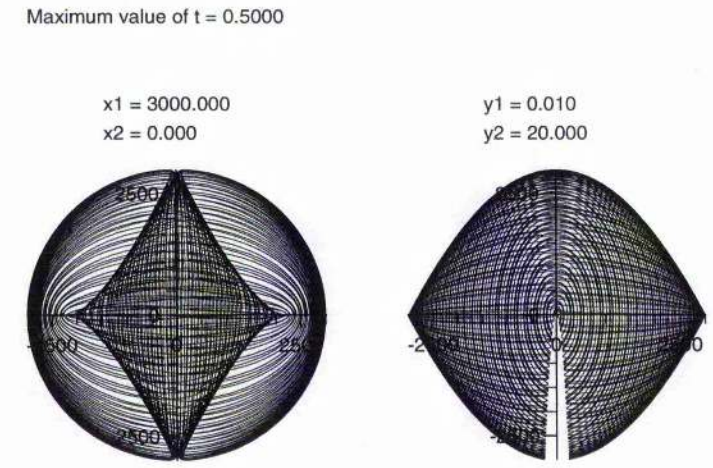

Figure 3.21: Unforced solution for short time, large x1.

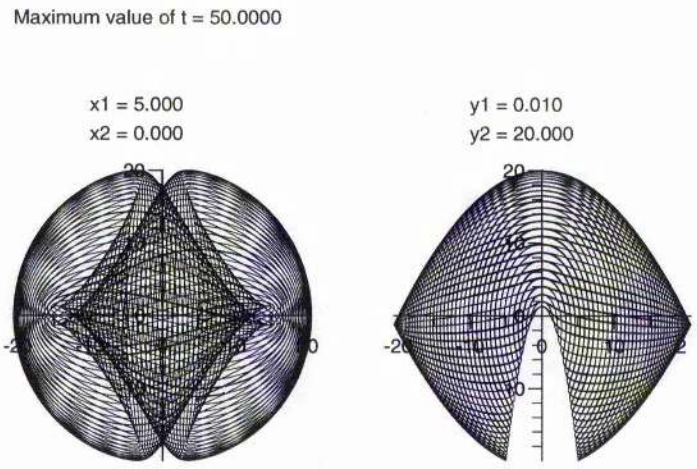

Figure 3.22: Unforced solution for long time, x1=5, y2=20.

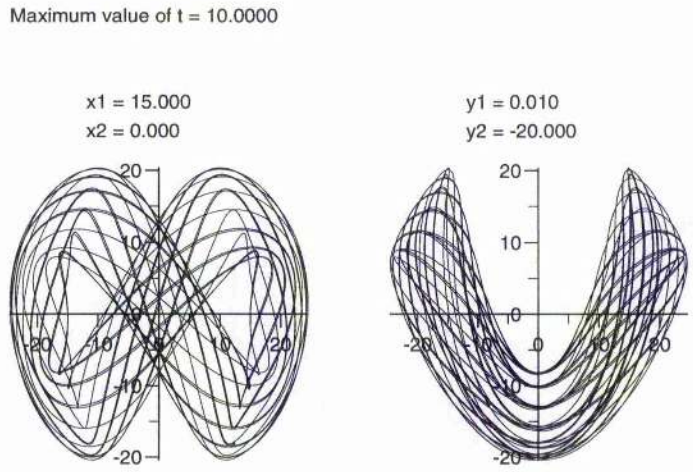

Figure 3.23: Forced solution for $t = 10$, x1=15, y2=-20.

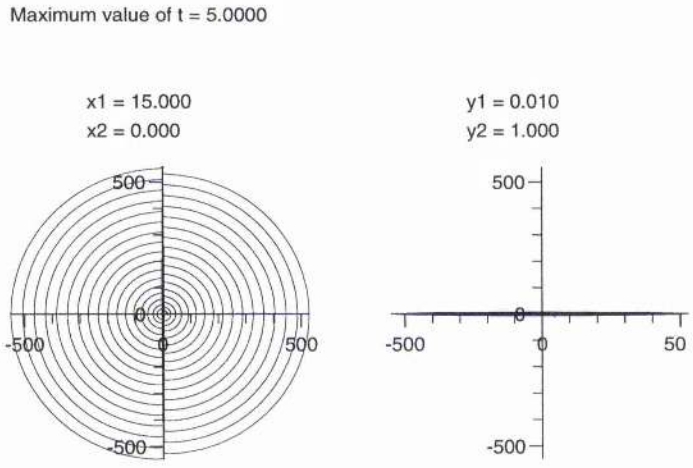

Figure 3.24: Forced solution for $t = 10$, x1=15, y2=1.

3.3 Equations with ϕ_1 dependence.

3.3.1 Reduction to ϕ_1 dependence equations.

With the change of variables (3.18), (3.19) and (3.20) used in section 1, the equations (3.42)-(3.45) can, after the use of trigonometric formulae, be rewritten as

$$\dot{X} = Z - 2Y^2 + (X\cos 4\phi_1 - Y\sin 4\phi_1) \tag{3.47}$$

$$\dot{Y} = 2XY + (-X\sin 4\phi_1 - Y\cos 4\phi_1) \tag{3.48}$$

$$\dot{Z} = -2XZ \tag{3.49}$$

$$\dot{\phi}_1 = -Y, \tag{3.50}$$

and the system is again 4-dimensional.

Examining the above system, it is noted from equation (3.50) that

$$d\phi_1 = -Y dt \tag{3.51}$$

If we now assume that Y does not change sign during the motion, then we can use a new independent variable $\phi_1 \equiv \int -Y dt$, and the system of equations (3.47) to (3.50) can now be expressed as

$$\frac{dX}{d\phi_1} = 2Y - \frac{Z}{Y} + \left(\sin 4\phi_1 - \frac{X}{Y}\cos 4\phi_1\right) \tag{3.52}$$

$$\frac{dY}{d\phi_1} = -2X + \left(\cos 4\phi_1 + \frac{X}{Y}\sin 4\phi_1\right) \tag{3.53}$$

$$\frac{dZ}{d\phi_1} = \frac{2XZ}{Y} \tag{3.54}$$

$$\frac{d\phi_1}{d\phi_1} = 1 \tag{3.55}$$

where $Y \neq 0$.

When X, Y and Z are all large, equations (3.52) and (3.53) can be thought of as a perturbation about the unforced equations

$$\begin{aligned} \frac{dX}{d\phi_1} &= 2Y - \frac{Z}{Y} \\ \frac{dY}{d\phi_1} &= -2X \\ \frac{dZ}{d\phi_1} &= \frac{2XZ}{Y} \end{aligned}$$

and this suggests an approximation procedure based on the scalings

$$\begin{aligned} Z &= \varepsilon^{-2}\zeta(\tau) \\ Y &= \varepsilon^{-1}\eta(\tau) \\ X &= \varepsilon^{-1}\xi(\tau) \end{aligned}$$

where

$$\zeta(\tau) = \zeta_0 + \varepsilon\zeta_1 + \dots \tag{3.56}$$

$$\eta(\tau) = \eta_0 + \varepsilon\eta_1 + \dots \tag{3.57}$$

$$\xi(\tau) = \xi_0 + \varepsilon\xi_1 + \dots \tag{3.58}$$

$$\phi_1(\tau) = \phi_{10} + \varepsilon\phi_{11} + \dots . \tag{3.59}$$

Substitution of these into the system (3.52), (3.53) and (3.54) gives a hierarchy of

sets of three equations. At leading order in ε, we recover the unforced equations

$$\xi_{0\phi_1} = 2\eta_0 - \frac{\zeta_0}{\eta_0} \tag{3.60}$$

$$\eta_{0\phi_1} = -2\xi_0 \tag{3.61}$$

$$\zeta_{0\phi_1} = \frac{2\xi_0\zeta_0}{\eta_0} \tag{3.62}$$

and these have a set of fixed points corresponding to

$$\xi_0 = 0, \qquad \zeta_0 = 2\eta_0^2.$$

3.3.2 The fixed points in cartesian coordinates.

Here we examine the family of fixed points

$$(\xi_0, \eta_0, \zeta_0) = (0, k, 2k^2),$$

where k is a constant.

In order to analyse their form in the cartesian system, we need to remind ourselves of the transformation

$$X = r_2 \cos\Phi$$

$$Y = r_2 \sin\Phi$$

$$Z = r_1^2.$$

After a little working, the family of points

$$X = 0, \qquad Y = \frac{k}{\varepsilon}, \qquad Z = 2\left(\frac{k}{\varepsilon}\right),$$

easily yields the relations

$$\begin{aligned} \Phi &= n\pi \pm \frac{\pi}{2} \\ \frac{r_1}{\sqrt{2}} &= r_2, \end{aligned}$$

where n is an integer.

This gives the family of points

$$\begin{aligned} x_{10} &= r_1 \cos\phi_1, \qquad x_{20} = \frac{r_1}{\sqrt{2}} \cos(2\phi_1 + n\pi \pm \frac{\pi}{2}) \\ y_{10} &= r_1 \sin\phi_1, \qquad y_{20} = \frac{r_1}{\sqrt{2}} \sin(2\phi_1 + n\pi \pm \frac{\pi}{2}), \end{aligned}$$

where $\phi_2 = \Phi + 2\phi_1$.

After further simplification we obtain the four initial values

$$\begin{aligned} x_{10} &= r_1 \cos\phi_1, \\ y_{10} &= r_1 \sin\phi_1, \\ x_{20} &= \mp\frac{r_1}{\sqrt{2}} \sin 2\phi_1, \\ y_{20} &= \pm\frac{r_1}{\sqrt{2}} \cos 2\phi_1, \end{aligned}$$

which represents a family of circles in the cartesian systems x_{10} v y_{10} and x_{20} v y_{20}. When plotting x_{10} v x_{20} and y_{10} v y_{20}, we obtain the curves shown in figure (3.25). These curves relate closely to those shown in figures (3.4)-(3.6).

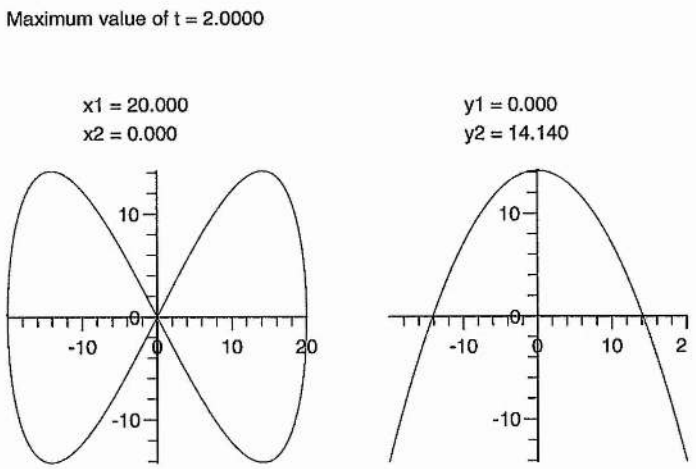

Figure 3.25: Fixed point family for $(x_{10}, y_{10}, x_{20}, y_{20}) = (20, 0, 0, 14.14)$.

3.3.3 Expansion of fixed points to next order.

Letting $\eta_0 = e$ where e is an $O(1)$ parameter, at next order the perturbation of the system about the fixed point becomes

$$\xi_{1\phi_1} = 4\eta_1 - \frac{\zeta_1}{e} + \sin 4\phi_1 \tag{3.63}$$

$$\eta_{1\phi_1} = -2\xi_1 + \cos 4\phi_1 \tag{3.64}$$

$$\zeta_{1\phi_1} = 4\xi_1 e \tag{3.65}$$

giving the matrix form

$$\begin{pmatrix} \xi_{1\phi_1} \\ \eta_{1\phi_1} \\ \zeta_{1\phi_1} \end{pmatrix} = \begin{pmatrix} 0 & 4 & -\frac{1}{e} \\ -2 & 0 & 0 \\ 4e & 0 & 0 \end{pmatrix} \begin{pmatrix} \xi_1 \\ \eta_1 \\ \zeta_1 \end{pmatrix} + \begin{pmatrix} \sin 4\phi_1 \\ \cos 4\phi_1 \\ 0 \end{pmatrix}.$$

We can now examine the stability of the system about the fixed point by looking to see if the values (ξ, η, ζ) grow indefinitely with time. To do this we seek a solution in terms of a complementary function and a particular integral. First for the complementary function we have

$$\begin{pmatrix} \xi_{1\phi_1} \\ \eta_{1\phi_1} \\ \zeta_{1\phi_1} \end{pmatrix} = \begin{pmatrix} 0 & 4 & -\frac{1}{e} \\ -2 & 0 & 0 \\ 4e & 0 & 0 \end{pmatrix} \begin{pmatrix} \xi_1 \\ \eta_1 \\ \zeta_1 \end{pmatrix}. \tag{3.66}$$

If this is tested for stability at the fixed point we obtain

$$\begin{vmatrix} -\lambda & 4 & -\frac{1}{e} \\ -2 & -\lambda & 0 \\ 4e & 0 & -\lambda \end{vmatrix} = 0, \tag{3.67}$$

or

$$\lambda(\lambda^2 + 12) = 0$$

for the three eigenvalues λ.

This gives

$$\lambda = 0 \qquad \lambda = \pm 2\sqrt{3}i.$$

Since the eigenvalues all have zero real part, the complementary function is neutrally stable about the fixed point. This result ought to have been expected, as the unforced equations are conservative and the forcing is represented by the

particular integral. The eigenvectors corresponding to the above eigenvalues are

$$\alpha \begin{pmatrix} 0 \\ 1 \\ 4e \end{pmatrix}, \qquad \beta \begin{pmatrix} \mp\sqrt{3}i \\ 1 \\ 2e \end{pmatrix}$$

which gives the real complementary function for (3.63)-(3.65) as

$$\begin{pmatrix} \xi_1 \\ \eta_1 \\ \zeta_1 \end{pmatrix} = \alpha_1 \begin{pmatrix} 0 \\ 1 \\ 4e \end{pmatrix} + \beta_1 \begin{pmatrix} \sqrt{3}i \\ 1 \\ -2e \end{pmatrix} \exp^{-2\sqrt{3}i\phi_1} + \beta_1^* \begin{pmatrix} -\sqrt{3}i \\ 1 \\ -2e \end{pmatrix} \exp^{2\sqrt{3}i\phi_1},$$

where α_1 is a real and β_1 a complex arbitrary constant.

Next we seek to look at the particular integral. To do this we look for solutions of the form

$$\begin{aligned} \xi_1 &= A\cos 4\phi_1 + B\sin 4\phi_1 \\ \eta_1 &= C\cos 4\phi_1 + D\sin 4\phi_1 \\ \zeta_1 &= F\cos 4\phi_1 + G\sin 4\phi_1 \end{aligned}$$

which give the 6 equations

$$\begin{aligned} 4A &= -4D + \frac{F}{e} - 1 \\ 4B &= 4C - \frac{E}{e} \\ 4C &= 2B \\ 4D &= -2A + 1 \end{aligned}$$

$$4E = -4eB$$

$$4F = 4eA$$

corresponding to a particular integral for of

$$\begin{pmatrix} -2\cos 4\phi_1 \\ \frac{5}{4}\sin 4\phi_1 \\ -2e\sin 4\phi_1 \end{pmatrix}.$$

If we now combine the above with the solutions for the complementary functions then we obtain the complete solution for the system about the fixed point at this order of approximation as

$$\begin{pmatrix} \xi_1 \\ \eta_1 \\ \zeta_1 \end{pmatrix} = \alpha_1 \begin{pmatrix} 0 \\ 1 \\ 4e \end{pmatrix} + \beta_1 \begin{pmatrix} 2\sqrt{3}\sin 2\sqrt{3}(\phi_1 - \phi_0) \\ 2\cos 2\sqrt{3}(\phi_1 - \phi_0) \\ -4e\cos 2\sqrt{3}(\phi_1 - \phi_0) \end{pmatrix} + \begin{pmatrix} -2\cos 4\phi_1 \\ \frac{5}{4}\sin 4\phi_1 \\ -2e\sin 4\phi_1 \end{pmatrix},$$

taking $\alpha_1, \alpha_2, \beta_1$ and β_2 as real, and introducing an arbitrary phase shift ϕ_0, which can be dropped without any loss of generality.

It is seen from the above solutions that no growth terms exist for this solution of ξ_1, η_1 and ζ_1. Thus the complete solution (ξ, η, ζ) is neutrally stable about the fixed point to this level of approximation.

The question still remains as to what mechanism drives the system unstable. The answer may lie in the higher order non-linear terms which arise in the next order of approximation. At the next order the equations become

$$\xi_{2\phi_1} = 4\eta_2 + \frac{\zeta_1\eta_1}{e^2} - \frac{\zeta_2}{e} - \frac{2\eta_1^2}{e} - \frac{\xi_1}{e}\cos 4\phi_1 \qquad (3.68)$$

$$\eta_{2\phi_1} = -2\xi_2 + \frac{\xi_1}{e}\sin 4\phi_1 \tag{3.69}$$

$$\zeta_{2\phi_1} = -4\xi_1\eta_1 + \frac{2\xi_1\zeta_1}{e} + 4\xi_2 e \tag{3.70}$$

giving the matrix form

$$\begin{pmatrix} \xi_{2\phi_1} \\ \eta_{2\phi_1} \\ \zeta_{2\phi_1} \end{pmatrix} = \begin{pmatrix} 0 & 4 & -\frac{1}{e} \\ -2 & 0 & 0 \\ 4e & 0 & 0 \end{pmatrix} \begin{pmatrix} \xi_2 \\ \eta_2 \\ \zeta_2 \end{pmatrix} + \begin{pmatrix} \frac{\zeta_1\eta_1}{e^2} - \frac{2\eta_1^2}{e} - \frac{\xi_1}{e}\cos 4\phi_1 \\ \frac{\xi_1}{e}\sin 4\phi_1 \\ -4\xi_1\eta_1 + \frac{2\xi_1\zeta_1}{e} \end{pmatrix}.$$

Upon substitution of the first order solutions into the above system we obtain the three equations

$$\begin{aligned} \xi_{2\phi_1} - 4\eta_2 + \frac{\zeta_2}{e} = \frac{2\alpha_1^2}{e} - \frac{8\beta_1^2}{e} - \frac{29}{16e} - \frac{4\alpha_1\beta_1}{e}\cos 2\sqrt{3}\phi_1 - \frac{2\alpha_1}{e}\sin 4\phi_1 \\ + \frac{61}{16e}\cos 8\phi_1 + \left(\frac{19}{2} - \sqrt{3}\right)\frac{\beta_1}{e}\sin(2\sqrt{3} - 4)\phi_1 \\ - \left(\frac{19}{2} + \sqrt{3}\right)\frac{\beta_1}{e}\sin(2\sqrt{3} + 4)\phi_1 - \frac{8\beta_1^2}{e}\cos 4\sqrt{3}\phi_1, \end{aligned}$$

$$\eta_{2\phi_1} + 2\xi_2 = \frac{\sqrt{3}\beta_1}{e}\cos(2\sqrt{3} - 4)\phi_1 - \frac{\sqrt{3}\beta_1}{e}\cos(2\sqrt{3} + 4)\phi_1 - \frac{1}{e}\sin 8\phi_1$$

and

$$\begin{aligned} \zeta_{2\phi_1} - 4e\xi_2 = 8\sqrt{3}\alpha_1\beta_1\sin 2\sqrt{3}\phi_1 - 16\sqrt{3}\beta_1^2\sin 4\sqrt{3}\phi_1 \\ + (16 - 9\sqrt{3})\beta_1\cos(2\sqrt{3} - 4)\phi_1 + (16 + 9\sqrt{3})\beta_1\cos(2\sqrt{3} + 4)\phi_1 \\ - 8\alpha_1\cos 4\phi_1 + 9\sin 8\phi_1. \end{aligned}$$

Since the complementary function at this next order is of exactly the same form as previously, it is necessary to discover whether the particular integral contains secular terms of the forms

$$A\phi_1 + B \qquad \text{or} \qquad (A_1\phi_1 + A_2)\cos 2\sqrt{3}\phi_1 + (B_1\phi_1 + B_2)\sin 2\sqrt{3}\phi_1.$$

Looking first at the constant terms on the r.h.s. of the equations and seeking a particular integral of the form

$$\begin{aligned} \xi_2 &= a\phi_1 + b \\ \eta_2 &= c\phi_1 + d \\ \zeta_2 &= e'\phi_1 + f \end{aligned}$$

we obtain the six equations

$$\begin{aligned} -4c + \frac{e'}{e} &= 0 \\ a - 4d + \frac{f}{e} &= \frac{2\alpha_1^2}{e} - \frac{8\beta_1^2}{e} - \frac{29}{16e} \\ 2a &= 0 \\ c + 2b &= 0 \\ e' - 4eb &= 0 \\ -4ea &= 0. \end{aligned}$$

This gives a solution

$$a = 0, b = 0, c = 0, d = 0, e' = 0, f = \frac{2\alpha_1^2}{e} - \frac{8\beta_1^2}{e} - \frac{29}{16e},$$

which leads to a particular integral for the constant terms of

$$\begin{pmatrix} \xi_2 \\ \eta_2 \\ \zeta_2 \end{pmatrix} = \begin{pmatrix} 0 \\ 0 \\ \frac{2\alpha_1^2}{e} - \frac{8\beta_1^2}{e} - \frac{29}{16e}. \end{pmatrix}$$

Obviously the constant terms cannot give secular growth, so attention is now turned towards seeking a particular integral of the form

$$\begin{aligned}
\xi_2 &= (A_1\phi_1 + A_2)\cos 2\sqrt{3}\phi_1 + (B_1\phi_1 + B_2)\sin 2\sqrt{3}\phi_1 \\
\eta_2 &= (C_1\phi_1 + C_2)\cos 2\sqrt{3}\phi_1 + (D_1\phi_1 + D_2)\sin 2\sqrt{3}\phi_1 \\
\zeta_2 &= (E_1\phi_1 + E_2)\cos 2\sqrt{3}\phi_1 + (F_1\phi_1 + F_2)\sin 2\sqrt{3}\phi_1,
\end{aligned}$$

for which secular growth occurs if any one of the 'ϕ-terms' is non-zero. Substituting these into the above system yields the 12 equations

$$\begin{aligned}
A_1 + 2\sqrt{3}B_2 - 4C_2 + \frac{E_2}{e} &= -\frac{4\alpha_1\beta_1}{e} \\
-2\sqrt{3}A_2 + B_1 - 4D_2 + \frac{F_2}{e} &= 0 \\
-2\sqrt{3}A_1 - 4D_1 + \frac{F_1}{e} &= 0 \\
2\sqrt{3}B_1 - 4C_1 + \frac{E_1}{e} &= 0 \\
C_1 + 2\sqrt{3}D_2 + 2A_2 &= 0 \\
-2\sqrt{3}C_2 + D_1 + 2B_1 &= 0 \\
-2\sqrt{3}C_1 + 2B_1 &= 0 \\
2\sqrt{3}D_1 + 2A_1 &= 0
\end{aligned}$$

$$
\begin{aligned}
E_1 + 2\sqrt{3}F_2 - 4eA_2 &= 0 \\
-2\sqrt{3}E_2 + F_1 - 4eB_2 &= 8\sqrt{3}\alpha_1\beta_1 \\
-2\sqrt{3}E_1 - 4eB_1 &= 0 \\
2\sqrt{3}F_1 - 4eA_1 &= 0
\end{aligned}
$$

which are satisfied when

$$A_1 = 0, B_1 = 0, C_1 = 0, D_1 = 0, E_1 = 0, F_1 = 0,$$

$$A_2 = 0, B_2 = 0, C_2 = 0, D_2 = 0, E_2 = -4\alpha_1\beta_1, F_2 = 0.$$

Hence a particular integral for the $\cos 2\sqrt{3}\phi_1$ and $\sin 2\sqrt{3}\phi_1$ terms is

$$
\begin{pmatrix} \xi_2 \\ \eta_2 \\ \zeta_2 \end{pmatrix} = \begin{pmatrix} 0 \\ 0 \\ -4\alpha_1\beta_1 \cos 2\sqrt{3}\phi_1 \end{pmatrix}
$$

and again this cannot give secular growth. Thus the fixed point solution at this order is again neutrally stable. Having discovered this, this analytical approach was taken no further.

3.3.4 Numerical investigation of the ϕ_1 equations.

The set of equations

$$\frac{dX}{d\phi_1} = 2Y - \frac{Z}{Y} + \left(\sin 4\phi_1 - \frac{X}{Y}\cos 4\phi_1\right) \tag{3.71}$$

$$\frac{dY}{d\phi_1} = -2X + \left(\cos 4\phi_1 + \frac{X}{Y}\sin 4\phi_1\right) \tag{3.72}$$

$$\frac{dZ}{d\phi_1} = \frac{2XZ}{Y} \tag{3.73}$$

$$\frac{d\phi_1}{d\phi_1} = 1 \tag{3.74}$$

are three dimensional, but they are dependent on Y not changing sign during the motion. Although this 3-D system is now non-autonomous, it is arguably better to use than a 4-D autonomous one. As before, these new equations are examined numerically, with (X, Z) plotted against each other and (ϕ_1, Y) plotted likewise. The second diagram in each set (3.26)-(3.29) is just an amplitude plot of Y and using initial data equivalent to figures (3.13), (3.14), (3.15) and (3.17), it is clearly seen that this new system exhibits far simpler behaviour than the old one. Here the unforced case, figures (3.30) and (3.31), consists of one closed periodic loop only and so has a far simpler structure than that of the cartesian system. Figure (3.26) represents initial data equivalent to that of figure (3.13) and in this case it is seen that the growing solutions occupy one-half of the phase-planes only. This must be so, as by using these equations we are governed by the conditions that Y does not change sign and Z is positive. The other figures showing bounded behaviour are clearly seen to be simple perturbations based on the unforced equations and these have similar space-filling properties to the cartesian system plotted in figures (3.14), (3.15) and (3.17).

Even with this system no criterion to separate the bounded solutions from

the unbounded has yet been isolated, so the boundary line has to be obtained numerically for different sets of initial data. Graphs are plotted in figures (3.32), (3.33) and (3.36) to (3.38) of Y against Z for different starting values of X and ϕ_1. Here the lines represent the partition between bounded and unbounded states of the system, with the area above the line corresponding to initial data giving bounded solutions and that below giving unbounded solutions.

The data points represented by the lines were computed numerically using the same program which provided the information depicted in figures (3.34) and (3.35). The necessary points were obtained by choosing an initial value of Y, and then estimating two values of Z, one which would give a bounded and the other an unbounded solution. This was done for set initial X and ϕ_1. Once these two different states were isolated, the corresponding Z values were then continually bisected until the partition value was reached to within an accuracy of 0.1 in Z. This process was then repeated for different Y until a sufficiently large data set was obtained to provide what was considered to be a smooth curve. The distinction between the unbounded and bounded states was determined by any excess of 10000 in X, Y or Z, this condition being built into the program. [Examples of the two different states are shown in figures (3.34) and (3.35)]. The obvious visual difference and the large change of scale on the Z-axis led to the conclusion that judgement in this way was an acceptable method of determining whether the diagrams showed an unbounded or bounded state.

Looking now at the graphs, figure (3.32) shows what happens when the initial values $\phi_1(0) = 0$ and $X(0) = 0, 5, 10$ are taken. When the starting value of X is increased, the value of $Z(0)$, represented on the partition line, also increases for given $Y(0)$. This is most prominent for $Y(0)$ between 3 and 20, but has less influence as $Y(0)$ gets large. The effect of increasing $X(0)$ in a positive direction appears to put some constraints on the value of $Z(0)$ needed for bounded solutions, indicating that some ratio between the two is needed to prevent the system growing. Certainly for initial data $X(0) = 10, \phi_1(0) = 0$, no bounded solutions exist if $Z(0)$ is less than 75, no matter what the value of $Y(0)$. Although obvious in a pictorial sense, no analytical relationship for the partition has been isolated.

In figures (3.33) and (3.36) boundary lines are now plotted for negative $X(0)$. The former figure shows the comparison between $X(0) = 10$ and $X(0) = -10$, while the latter compares $X(0) = 5$ and $X(0) = -5$. In both cases the curve for $X(0) = 0$ is shown. In figure (3.33) it is seen that for given $Y(0)$ greater than about 10 the initial value of Z needed for a bounded solution is now less than that for the curve $X(0) = 0$ and for all values of $Y(0)$ the $X(0) = -10$ curve lies below the $X(0) = 10$ curve. Similar results occur in figure (3.36) where this time the curve for $X(0) = -5$ drops below that for $X(0) = 0$ at around $Y(0) = 5$. These results seem to indicate that the appearance of bounded or unbounded solutions are not dependent on a simple energy ratio between individual components, but

that a more complicated phase-dependence must be at work.

The graphs for the case $\phi(0) = \frac{\pi}{4}$ are very similar to those with the initial value $\phi(0) = 0$, as shown in figures (3.36) and (3.37), but the same curves correspond to starting values of X with the sign reversed. This indicates that some invariant transformation must exist in these coordinates. Further examination of equations (3.71) to (3.74) reveals the transformations

$$\begin{aligned}
(X, Y, Z, \phi_1) &\longleftrightarrow (-X, -Y, Z, \phi_1 + \frac{\pi}{4}) \\
(X, Y, Z, \phi_1) &\longleftrightarrow (-X, Y, Z, \frac{\pi}{4} - \phi_1) \\
(X, Y, Z, \phi_1) &\longleftrightarrow (X, -Y, Z, \frac{\pi}{2} - \phi_1) \\
(X, Y, Z, \phi_1) &\longleftrightarrow (X, -Y, Z, -\phi_1).
\end{aligned}$$

It is the second of these that gives the correspondance between the data depicted in the two graphs. Figures (3.38) and (3.33) also show the same curves, but this time for $\phi_1(0) = 0, X(0) = -10$ and $\phi_1(0) = \frac{\pi}{4}, X(0) = 10$. With this information attention is now turned to the effect $\phi_1(0)$ has on the nature of the solutions. In figure (3.39) the value of $Z(0)$ needed for bounded solutions is investigated when $\phi_1(0)$ is varied between 0 and π. In this graph the initial values of X and Y remain set, and the data points are obtained as before. It is clearly seen from the curve produced that the values of $Z(0)$ needed for bounded states are periodic in ϕ_1 with a period $\frac{\pi}{2}$. This is to be expected due to the symmetry transformations described previously.

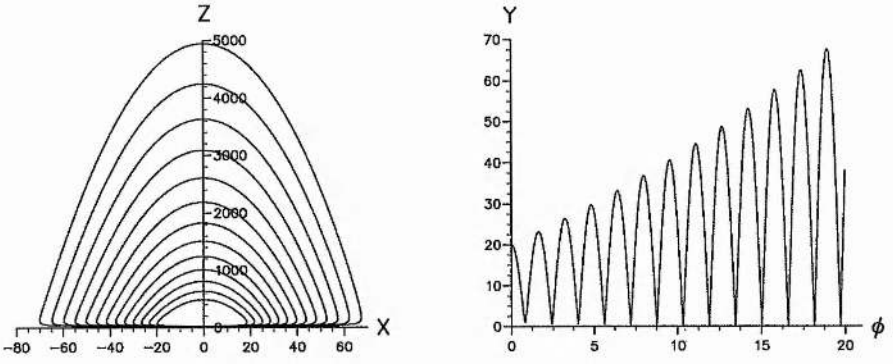

Figure 3.26: Diagram for forced phi dependence equations with initial data $(X, Y, Z, \phi) = (0.08, 20, 25, 0.002)$, equivalent to the cartesian system in figure (3.13).

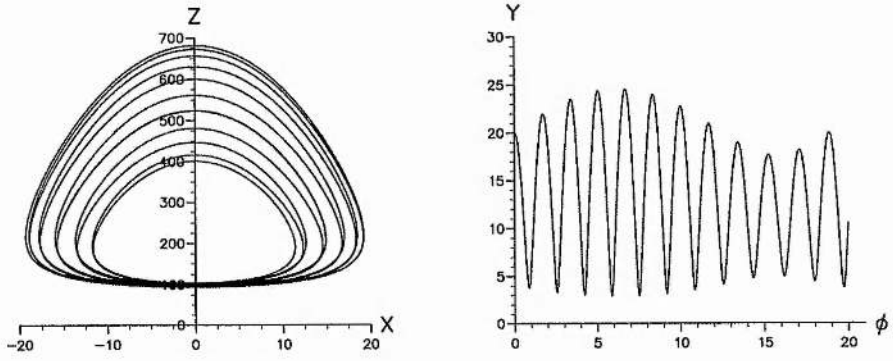

Figure 3.27: Diagram for forced phi dependence equations with initial data $(X, Y, Z, \phi) = (0.04, 20, 100, 0.001)$, equivalent to the cartesian system in figure (3.14).

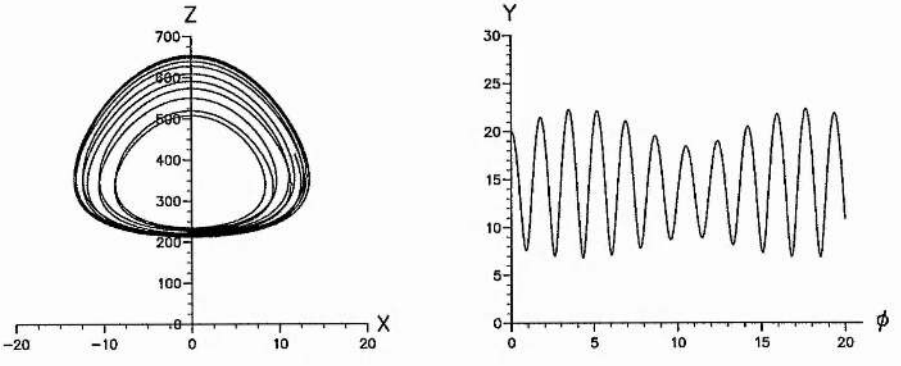

Figure 3.28: Diagram for forced phi dependence equations with initial data $(X, Y, Z, \phi) = (0.027, 20, 225, 0.001)$, equivalent to the cartesian system in figure (3.15).

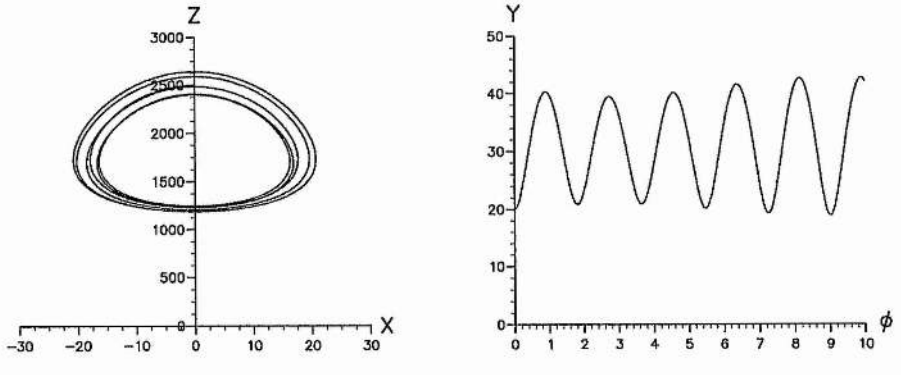

Figure 3.29: Diagram for forced phi dependence equations with initial data $(X, Y, Z, \phi) = (0.08, 20, 2500, 0.00)$, equivalent to the cartesian system in figure (3.17).

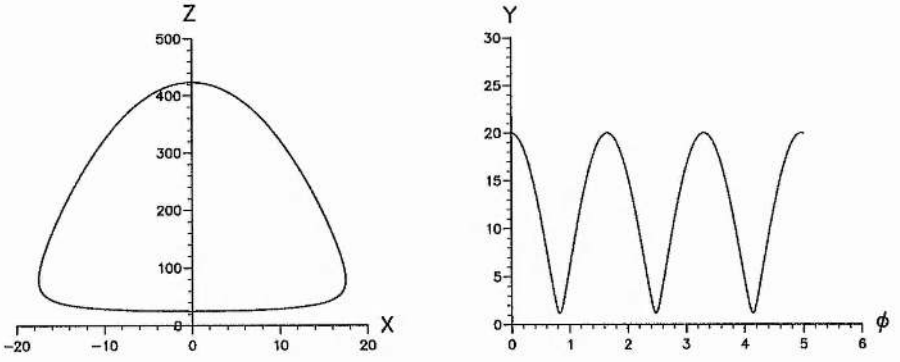

Figure 3.30: Diagram for unforced phi dependence equations with initial data $(X, Y, Z, \phi) = (0.08, 20, 25, 0.002)$, equivalent to the cartesian system in figure (3.22).

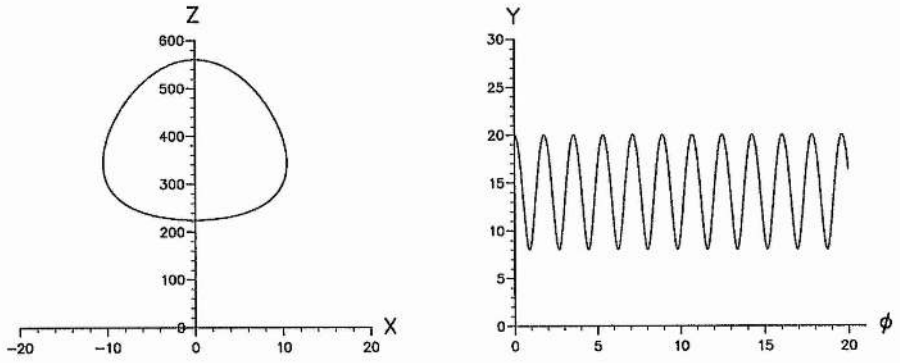

Figure 3.31: Diagram for unforced phi dependence equations with initial data $(X, Y, Z, \phi) = (0.027, 20, 225, 0.001)$.

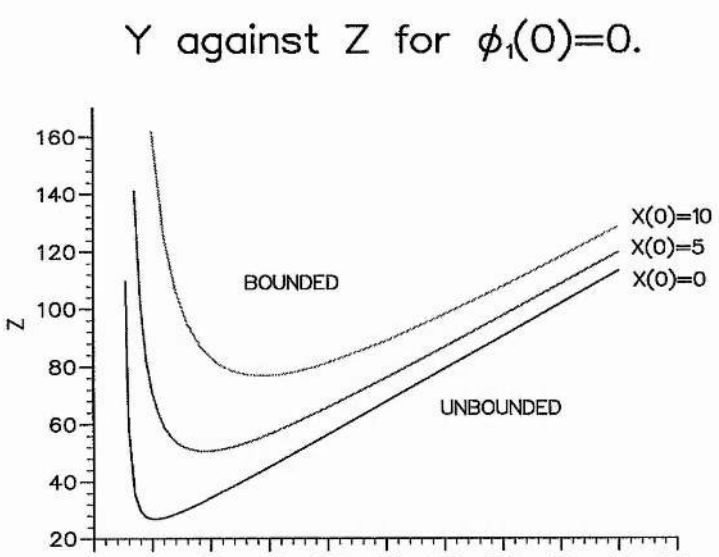

Figure 3.32: Graph showing the separation between bounded and unbounded states for initial values $\phi_1(0) = 0, X(0) = 0, X(0) = 5$ and $X(0) = 10$.

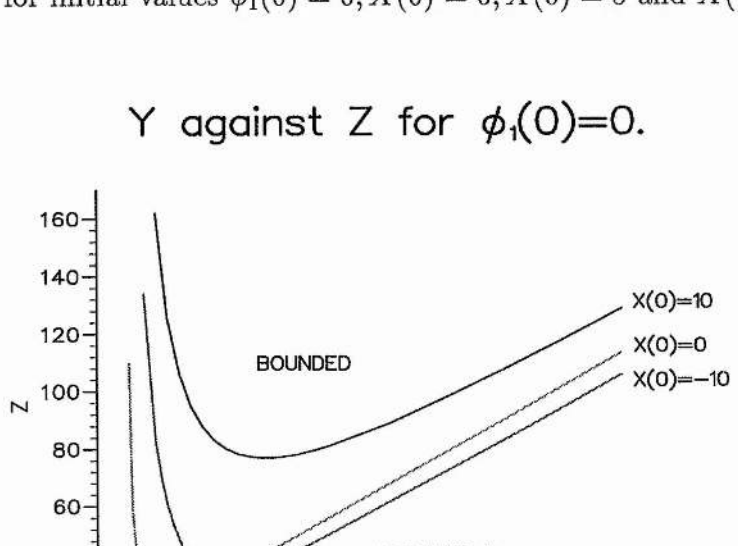

Figure 3.33: Graph showing the separation between bounded and unbounded states for initial values $\phi_1(0) = 0, X(0) = 0, X(0) = 10$ and $X(0) = -10$.

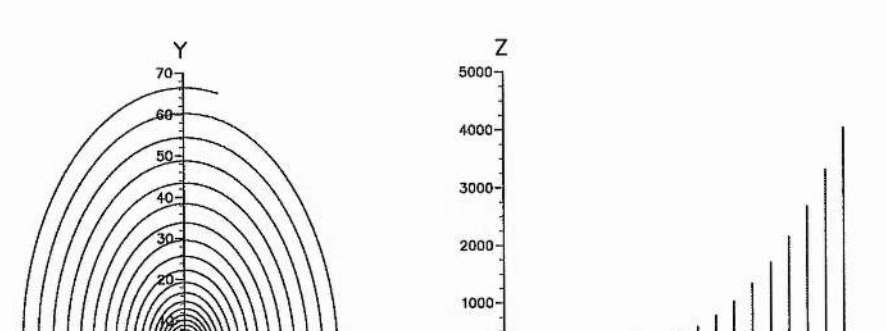

Figure 3.34: Diagram for phi dependence equations showing unbounded behaviour for initial data $(X, Y, Z, \phi) = (0.0, 5, 20, 0.0)$.

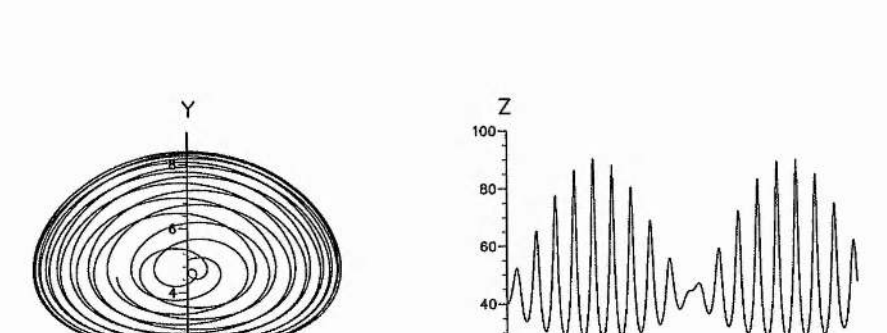

Figure 3.35: Diagram for phi dependence equations showing bounded behaviour for initial data $(X, Y, Z, \phi) = (0.0, 5, 40, 0.0)$.

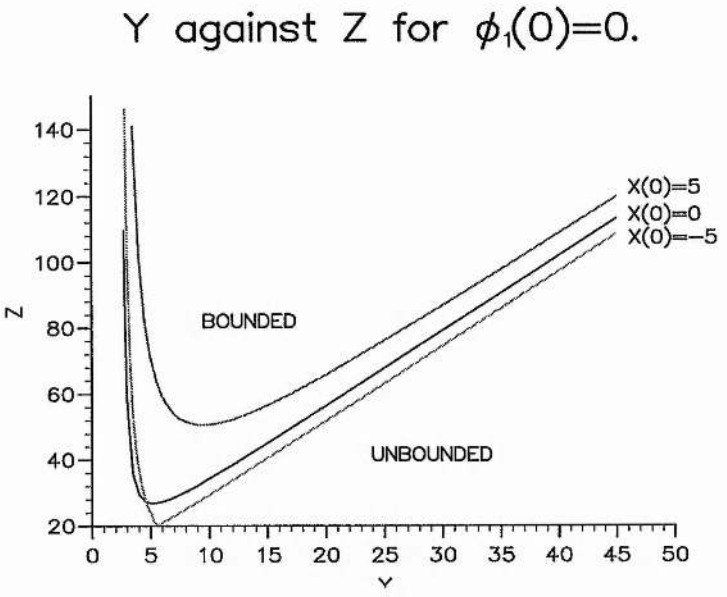

Figure 3.36: Graph showing the separation between bounded and unbounded states for initial values $\phi_1(0) = 0, X(0) = 0, X(0) = 5$ and $X(0) = -5$.

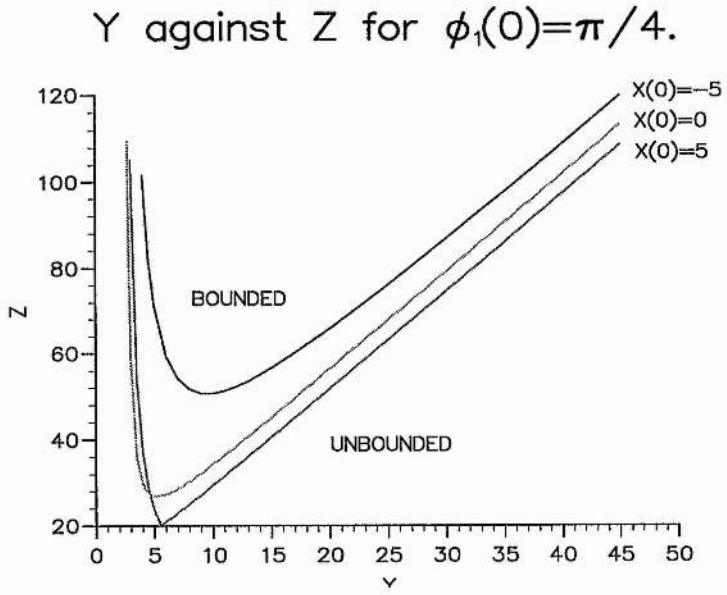

Figure 3.37: Graph showing the separation between bounded and unbounded states for initial values $\phi_1(0) = \pi/4, X(0) = 0, X(0) = 5$ and $X(0) = -5$.

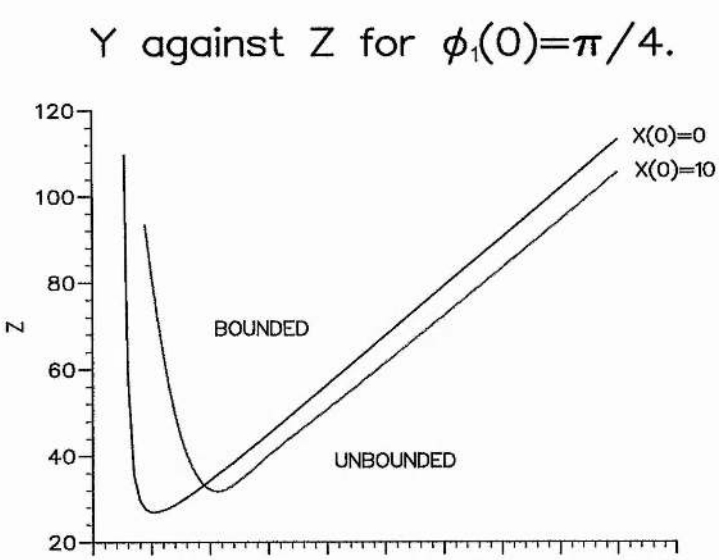

Figure 3.38: Graph showing the separation between bounded and unbounded states for initial values $\phi_1(0) = \pi/4, X(0) = 0$ and $X(0) = 10$.

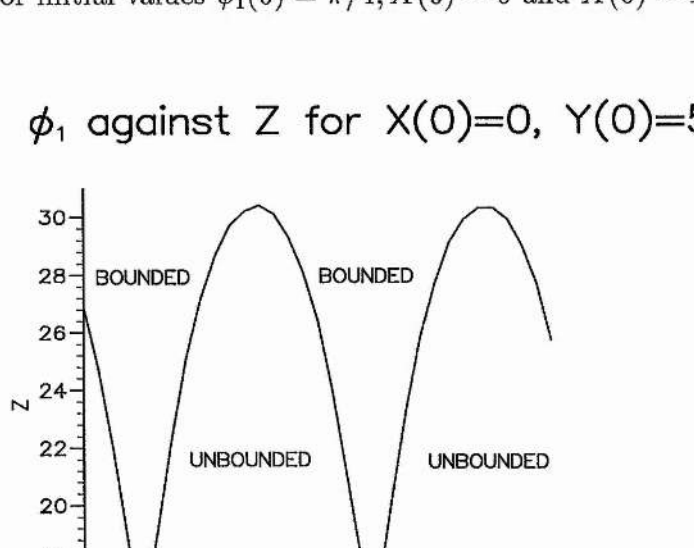

Figure 3.39: Graph showing the separation between bounded and unbounded states for initial values $X(0) = 0$ and $Y(0) = 5$.

3.4 Hamiltonian formulation.

Since the system (3.34)-(3.37) contains no damping terms, it is therefore conservative. This being the case, a Hamiltonian for the system exists. On setting

$$\begin{pmatrix} x_1 \\ y_1 \end{pmatrix} = \frac{1}{\sqrt{2}} \begin{pmatrix} X_1 \\ Y_1 \end{pmatrix},$$

(3.34)-(3.37) can be rewritten as

$$\dot{X}_1 = -X_1 x_2 - Y_1 y_2 \tag{3.75}$$

$$\dot{Y}_1 = Y_1 x_2 - X_1 y_2 \tag{3.76}$$

$$\dot{x}_2 = \frac{1}{2}(X_1^2 - Y_1^2) + x_2 \tag{3.77}$$

$$\dot{y}_2 = X_1 Y_1 - y_2. \tag{3.78}$$

The Hamiltonian, H, satisfys

$$\dot{X}_1 = -\frac{\partial H}{\partial Y_1}, \quad \dot{Y}_1 = \frac{\partial H}{\partial X_1}, \quad \dot{x}_2 = -\frac{\partial H}{\partial y_2}, \quad \dot{y}_2 = \frac{\partial H}{\partial x_2},$$

giving

$$H \equiv X_1 Y_1 x_2 + \frac{1}{2}(Y_1^2 - X_1^2) y_2 - x_2 y_2.$$

The velocity vector for the system is given by

$$\boldsymbol{v} \equiv (\dot{X}_1, \dot{Y}_1, \dot{x}_2, \dot{y}_2),$$

with the normal to the Hamiltonian surfaces H =constant given by

$$\boldsymbol{n} = \frac{(H_{X_1}, H_{Y_1}, H_{x_2}, H_{y_2})}{|(H_{X_1}, H_{Y_1}, H_{x_2}, H_{y_2})|} \equiv \frac{\nabla H}{|\nabla H|}.$$

It is easily seen that $\boldsymbol{v} \cdot \nabla H = 0$, thus showing that the velocity streamlines follow orbits on the four dimensional surfaces H =constant. If H is now fixed, then a family of orbits is selected. Thus one of X_1, Y_1, x_2, y_2, can be obtained explicitly. e.g. Choosing y_2, gives us

$$y_2 = \frac{H - X_1 Y_1 x_2}{\frac{1}{2}(Y_1^2 - X_1^2) - x_2},$$

where $\frac{1}{2}(Y_1^2 - X_1^2) - x_2 \neq 0$, and H is a parameter. From (3.75), (3.76) and (3.77), we obtain

$$\dot{X}_1 = -X_1 x_2 - \frac{Y_1(H - X_1 Y_1 x_2)}{\frac{1}{2}(Y_1^2 - X_1^2) - x_2}, \tag{3.79}$$

$$\dot{Y}_1 = Y_1 x_2 - \frac{X_1(H - X_1 Y_1 x_2)}{\frac{1}{2}(Y_1^2 - X_1^2) - x_2}, \tag{3.80}$$

$$\dot{x}_2 = \frac{1}{2}(X_1^2 - Y_1^2) + x_2, \tag{3.81}$$

which is a 3-D system for $(\dot{X}_1, \dot{Y}_1, \dot{x}_2)$.

Although the system has been reduced to three dimensions, this has been achieved at the expense of introducing a new parameter H. Accordingly, we still have four variables, but one of these (H) now remains constant with time. The system appears no more amenable to a full three-dimensional analysis than before; but we have not pursued this line of enquiry.

3.5 Conclusions.

In this chapter we have considered the undamped second-harmonic resonance equations at exact tuning. For the case of no Faraday forcing, the results of McGoldick (1970) are recovered and solutions in the form of elliptic integrals are obtained. When Faraday forcing occurs at the first harmonic, a substitution has been found that reduces the system to the unforced case and thus results in elliptic integral solutions as before. For forcing at the second-harmonic, no such reduction can be found and the system appears irreducibly four dimensional.

Such four dimensional systems remain extremely resistant to analysis and apart from a few special cases little progress has been made. Even so, these special cases still give a good insight into the varying behaviour of the system, with growing and degenerate solutions being found for the simplest of initial data. For more general cases an analytical approach was found to be impossible, with the system requiring numerical investigation. Again bounded and unbounded behaviours were discovered, with the bounded solutions appearing to be a slight perturbation on the unforced case. For the unbounded solutions a relationship was isolated that puts an exponential bound on the energy growth and thus shows that the system cannot experience finite time blow-up.

To gain more insight into the properties of the equations, new independent variables were introduced resulting in the system reducing to a three dimensional

non-autonomous set of equations. An approximation procedure yields a family of fixed point solutions at first order, with it being found that these solutions are neutrally stable to at least third order. Numerical simulation again reveals bounded and unbounded behaviour, with the solution trajectories taking a much simplier form than before. Regions where bounded and unbounded behaviours occur are calculated for specific parameter ranges, with it being found that no bounded solutions exist when the amplitude of the first wave is small enough.

On the whole such four dimensional systems remain intractable to analytical investigation. Introducing a time dependency into the equations can result in a three dimensional system, but it is then found that restrictions are placed on certain parameters. A Hamiltonian formulation also reduces the system to three equations, but once more this is achieved at the expense of introducing a new variable. Until further theory becomes available, numerical simulation will remain the only viable way of investigating such high order, non-linear systems.

Chapter 4

The damped and off-resonance equations.

4.1 Reduction of the equations.

In this chapter we examine the evolution equations that arise when off-resonance and viscous damping effects are included. The system becomes more amenable to local mathematical analysis than in the exact resonance undamped case, due to the appearance of families of fixed points. Becker & Miles (1986) were the first to isolate these fixed points for the case of a parametrically excited double pendulum. In their analysis they obtained the stability criteria for the general case and found Hopf bifurcations, and thus chaos, were possible for certain parameter regimes. In our study we rediscover these fixed point solutions and investigate in detail

some special cases that arise.

We first recall how off-resonance and viscous damping are added to the system. Allowing for off-resonance, so that the waves are close to resonating at the second-harmonic, the frequency mis-match is

$$\omega_2 - 2\omega_1 = \varepsilon\Delta_3$$

where ε is a small parameter and Δ_3 the mis-match. A frequency mis-match in the Faraday forcing is also incorporated, with the system being forced at close to twice the second-harmonic frequency. This gives

$$\Omega = 2\omega_2 + \varepsilon\Delta_2$$

where Δ_2 represents the forcing mis-match and Ω is the forcing frequency.

With the inclusion of the above terms and the allowance for viscous damping, the evolution equations become

$$\dot{a}_1 = \lambda_1 a_1^* a_2 e^{i\Delta_3 T} - \sigma_1 a_1 \tag{4.1}$$

$$\dot{a}_2 = \lambda_2 a_1^2 e^{-i\Delta_3 T} + \mu a_2^* e^{i\Delta_2 T} - \sigma_2 a_2, \tag{4.2}$$

where λ_1, λ_2 are real and μ is pure imaginary. Here σ_1 and σ_2, taken to be real and positive, are the respective linear damping coefficients attributable to viscous effects neglected in our earlier inviscid analysis.

Equations (4.1) and (4.2) are now reduced in two stages. Setting

$$a_1 \equiv b_1 e^{\frac{i\Delta_3 T}{2}} e^{\frac{i\Delta_2 T}{4}}, \qquad a_2 \equiv b_2 e^{\frac{i\Delta_2 T}{2}},$$

gives the autonomous equations

$$\begin{aligned}\dot{b}_1 &= \lambda_1 b_1^* b_2 - i\left(\frac{\Delta_2}{4} + \frac{\Delta_3}{2}\right) b_1 - \sigma_1 b_1 \\ \dot{b}_2 &= \lambda_2 b_1^2 - \frac{i\Delta_2}{2} b_2 + \mu b_2^* - \sigma_2 b_2,\end{aligned}$$

where the exponential terms have been eliminated. Then, scaling

$$b_1 \equiv \mu' \left(-\frac{1}{\lambda_1\lambda_2}\right)^{\frac{1}{2}} e^{i\frac{\pi}{8}} c_1, \qquad b_2 \equiv \left(-\frac{\mu'}{\lambda_1}\right) e^{i\frac{\pi}{4}} c_2, \qquad \mu \equiv \mu' e^{i\frac{\pi}{2}},$$

and recalling $\lambda_1 < 0$ and $\lambda_2 > 0$, we obtain

$$\begin{aligned}\frac{dc_1}{dT_1} &= -c_1^* c_2 - i\left(\frac{\Delta_2}{4\mu'} + \frac{\Delta_3}{2\mu'}\right) c_1 - \sigma_1' c_1 \\ \frac{dc_2}{dT_1} &= c_1^2 - \frac{i\Delta_2}{2\mu'} c_2 + c_2^* - \sigma_2' c_2,\end{aligned}$$

where $\sigma_1' = \frac{\sigma_1}{\mu'}$, $\sigma_2' = \frac{\sigma_2}{\mu'}$, $\mu' = \frac{fk}{4\omega}$ and $T_1 = \mu' T$, are all real and positive.

Dropping the primes and expressing c_1 and c_2 as

$$c_1 = x_1 + iy_1, \qquad c_2 = x_2 + iy_2,$$

we obtain the four dimensional system

$$\dot{x}_1 = -x_1(x_2 + \sigma_1) + y_1(\beta + \gamma - y_2) \tag{4.3}$$

$$\dot{y}_1 = y_1(x_2 - \sigma_1) - x_1(y_2 + \beta + \gamma) \tag{4.4}$$

$$\dot{x}_2 = x_1^2 - y_1^2 + 2\beta y_2 + x_2(1 - \sigma_2) \tag{4.5}$$

$$\dot{y}_2 = 2x_1 y_1 - 2\beta x_2 - y_2(1 + \sigma_2) \tag{4.6}$$

where $\beta = \frac{\Delta_2}{4\mu'}$ and $\gamma = \frac{\Delta_3}{2\mu'}$.

[Because of our chosen scalings, equations (4.3)-(4.6) take a different form from

those of the Becker & Miles study. Substituting for $c_1 \equiv e^{-\frac{3i\pi}{8}} b_1$ and $c_2 \equiv e^{-\frac{i\pi}{4}} b_2$, then $b_1 = p_1 + iq_1$ and $b_2 = p_1 + iq_2$, our (4.3)-(4.6) become their (2.7a)-(2.7d) after letting $(p_1, q_1) = \frac{1}{\sqrt{2}}(p_1', q_1')$.]

4.2 Fixed point solutions.

Fixed point solutions to the system (4.3)-(4.6) require

$$\dot{x}_1 = \dot{y}_1 = \dot{x}_2 = \dot{y}_2 = 0,$$

giving the four relations

$$x_1(x_2 + \sigma_1) = y_1(\beta + \gamma - y_2) \tag{4.7}$$

$$x_1(y_2 + \beta + \gamma) = y_1(x_2 - \sigma_1) \tag{4.8}$$

$$y_1^2 - x_1^2 = 2\beta y_2 + x_2(1 - \sigma_2) \tag{4.9}$$

$$2\beta x_2 = 2x_1 y_1 - y_2(1 + \sigma_2). \tag{4.10}$$

On rearranging, so that quadratic terms appear on the l.h.s., equations (4.7)-(4.10) are rewitten

$$x_1 x_2 + y_1 y_2 = -\sigma_1 x_1 + (\beta + \gamma) y_1 \tag{4.11}$$

$$x_1 y_2 - y_1 x_2 = -\sigma_1 y_1 - (\beta + \gamma) x_1 \tag{4.12}$$

$$x_1^2 - y_1^2 = -2\beta y_2 - x_2(1 - \sigma_2) \tag{4.13}$$

$$2x_1 y_1 = 2\beta x_2 + y_2(1 + \sigma_2). \tag{4.14}$$

On setting

$$x_1 + iy_1 = r_1 e^{i\theta_1}, \qquad x_2 + iy_2 = r_2 e^{i\theta_2},$$

equation (4.11) becomes

$$r_1 \left[r_2 \cos(\theta_1 - \theta_2) + \sigma_1 \cos\theta_1 - (\beta + \gamma) \sin\theta_1 \right] = 0, \tag{4.15}$$

with (4.12) becoming

$$r_1 \left[r_2 \sin(\theta_2 - \theta_1) + \sigma_1 \sin\theta_1 + (\beta + \gamma) \cos\theta_1 \right] = 0. \tag{4.16}$$

To satisfy (4.15) and (4.16) we require either

$$r_1 = 0, \tag{4.17}$$

which we will refer to as Case 1, or both

$$r_2 = \frac{(\beta + \gamma) \sin\theta_1 - \sigma_1 \cos\theta_1}{\cos(\theta_1 - \theta_2)} \tag{4.18}$$

and

$$r_2 = -\left(\frac{\sigma_1 \sin\theta_1 + (\beta + \gamma) \cos\theta_1}{\sin(\theta_2 - \theta_1)} \right), \tag{4.19}$$

which we will refer to as Case 2.

Expressing (4.13) and (4.14) in polar form, we obtain

$$r_1^2 \cos 2\theta_1 = -r_2 \left[2\beta \sin\theta_2 + (1 - \sigma_2) \cos\theta_2 \right] \tag{4.20}$$

and

$$r_1^2 \sin 2\theta_1 = r_2 \left[2\beta \cos\theta_2 + (1 + \sigma_2) \sin\theta_2 \right]. \tag{4.21}$$

respectively. Cases 1 and 2, respectively satisfying (4.17) and (4.18)-(4.19), are investigated individually and these, together with the relations (4.20) and (4.21), allow us to examine all the fixed point solutions.

Case 1.

From equations (4.20) and (4.21), with $r_1 = 0$, Case 1 gives

$$r_2 = 0,$$

or

$$\tan\theta_2 = \frac{(\sigma_2 - 1)}{2\beta} \quad \text{and} \quad \tan\theta_2 = -\frac{2\beta}{(1+\sigma_2)}$$

The first of these yields the origin as a solution, with the second giving a family of points for which $\beta = \pm\frac{1}{2}(1-\sigma_2^2)^{\frac{1}{2}}$. This second solution requires $0 \leq \sigma_2 \leq 1$ for β to be real. Three families of fixed points can thus be written down:

1. $x_1 = y_1 = x_2 = y_2 = 0, \qquad$ with $\sigma_1, \sigma_2, \gamma, \beta$ arbitrary, (4.22)

2. $x_1 = y_1 = y_2 = \beta = 0, \quad \sigma_2 = 1, \qquad$ with σ_1, γ, x_2 arbitrary, (4.23)

3. $x_1, y_1 = 0, \quad \beta = \pm\frac{1}{2}(1-\sigma_2^2)^{\frac{1}{2}}, \quad x_2 = \frac{2\beta}{(\sigma_2 - 1)}y_2, \quad 0 \leq \sigma_2 < 1,$ (4.24)
with σ_1, γ arbitrary.

Family 2 corresponds to the special case when the forcing equals the damping. The stability of all three families is examined analytically in due course.

Case 2.

For Case 2 we require $r_1 \neq 0$. Setting (4.18) and (4.19) equal gives the consistency relation

$$\tan(\theta_2 - 2\theta_1) = \frac{(\beta+\gamma)}{\sigma_1}, \tag{4.25}$$

with the expression

$$\tan 2\theta_1 = -\left(\frac{2\beta + (1+\sigma_2)\tan\theta_2}{2\beta\tan\theta_2 + (1-\sigma_2)}\right) \tag{4.26}$$

obtained by dividing (4.20) by (4.21). Equation (4.25) now gives

$$\begin{aligned} \theta_2 - 2\theta_1 &= \tan^{-1}\left(\frac{\beta+\gamma}{\sigma_1}\right) \pm n\pi \\ &\equiv \delta \pm n\pi, \end{aligned}$$

where $\delta = \tan^{-1}\left(\frac{\beta+\gamma}{\sigma_1}\right)$ and n is any integer. Hence

$$\tan 2\theta_1 = \tan(\theta_2 - \delta) \tag{4.27}$$

with solutions for θ_1 given by

$$\theta_1 = \frac{1}{2}(\theta_2 - \delta \pm n\pi). \tag{4.28}$$

Substitution of (4.27) into (4.26) gives the solution of the resulting quadratic equation as

$$\tan\theta_2 = \frac{-\sigma_1 \pm \sqrt{\sigma_1^2 - 4\beta^2\sigma_1^2 - 4\beta\sigma_1\sigma_2(\beta+\gamma) + (1-\sigma_2^2)(\beta+\gamma)^2}}{(2\beta\sigma_1 + (1+\sigma_2)(\beta+\gamma))} \tag{4.29}$$

where

$$\sigma_1^2 - 4\beta^2\sigma_1^2 - 4\beta\sigma_1\sigma_2(\beta+\gamma) + (1-\sigma_2^2)(\beta+\gamma)^2 \geq 0 \tag{4.30}$$

must be satisfied for real solutions to exist. If (4.30) holds, values of θ_2 can be calculated from

$$\theta_2 = \tan^{-1}\left(\frac{-\sigma_1 \pm \sqrt{\sigma_1^2 - 4\beta^2\sigma_1^2 - 4\beta\sigma_1\sigma_2(\beta+\gamma) + (1-\sigma_2^2)(\beta+\gamma)^2}}{(2\beta\sigma_1 + (1+\sigma_2)(\beta+\gamma))}\right) \pm m\pi,$$

where m is any integer; with θ_1 following from (4.28).

To calculate the amplitudes of the two waves, r_2 is first simplified. By writing

$$\cos(\theta_1 - \theta_2) = \cos(2\theta_1 - \theta_2 - \theta_1),$$

giving

$$\cos(\theta_1 - \theta_2) = \cos(\theta_2 - 2\theta_1)\cos\theta_1 - \sin(\theta_2 - 2\theta_1)\sin\theta_1,$$

and taking

$$\sin(\theta_2 - 2\theta_1) = \frac{(\beta+\gamma)}{\sqrt{\sigma_1^2 + (\beta+\gamma)^2}} \quad \text{and} \quad \cos(\theta_2 - 2\theta_1) = \frac{\sigma_1}{\sqrt{\sigma_1^2 + (\beta+\gamma)^2}}$$

from (4.25), (4.18) and (4.19) become

$$r_2 = \left[\sigma_1^2 + (\beta+\gamma)^2\right]^{\frac{1}{2}}$$

where the appropriate square root has been taken.

The value of r_1 can also be written down and satisfies

$$r_1^2 = r_2\left(\frac{2\beta\cos\theta_2 + (1+\sigma_2)\sin\theta_2}{\sin 2\theta_1}\right) \quad \text{and} \quad r_1^2 = -r_2\left(\frac{2\beta\sin\theta_2 + (1-\sigma_2)\cos\theta_2}{\cos 2\theta_1}\right).$$

Real solutions require $r_1 \geq 0$.

The solutions arising from Cases 1 and 2 are next examined in more detail.

4.3 The fixed points of Case 1.

4.3.1 Location of the families.

For Case 1 three specific families of points were found above, (4.22)-(4.24). The relatively simple nature of these families allows us to describe the conditions needed for their existence. In all cases σ_1 and γ may take any value, but for families 2 and 3 values of σ_2 and β are restricted. (It should be noted that family 2 is the limiting case of family 3 and the two cannot appear together).

An easy way to picture the conditions required is to examine the $\sigma_2 - \beta$ plane. Families 1 and 2 give straightforward results, with the origin existing over the entire plane and family 2 existing only at the point (1,0). Family 3 proves a little more complicated, existing only along the curve $\beta = \pm\frac{1}{2}(1-\sigma_2^2)^{\frac{1}{2}}$, with $0 \leq \sigma_2 < 1$. Figure (4.1) shows graphically the curve $\beta = \pm\frac{1}{2}(1-\sigma_2^2)^{\frac{1}{2}}$ in the $\sigma_2 - \beta$ plane with the point $(\sigma_2, \beta) = (1, 0)$ being indicated.

Another method of examination is to consider where the families exist in the Cartesian coordinate planes. Since Case 1 required $r_1 = 0$, we can ignore the $x_1 - y_1$ plane, but consideration of the $x_2 - y_2$ plane is useful. This is portrayed in figure (4.2). By definition the origin exists only at the point (x_2, y_2)=$(0, 0)$, but for families 2 and 3 we discover an infinite number of possibilities. Family 2 is found to exist anywhere along the x_2 axis, with family 3 existing along a line $x_2 = my_2$ with gradient given by the reciprocal of $m = \frac{2\beta}{(\sigma_2-1)}$, where m depends

on the values of β and σ_2 chosen. It should be remembered that β and σ_2 are given by the curve shown in figure (4.1): this requires the gradient m^{-1} of the lines to satisfy $\left|\frac{y_2}{x_2}\right| < 1$, since $\frac{y_{20}}{x_{20}} = \pm\left(\frac{1-\sigma_2}{1+\sigma_2}\right)^{\frac{1}{2}}$ with $0 \leq \sigma_1 < 1$.

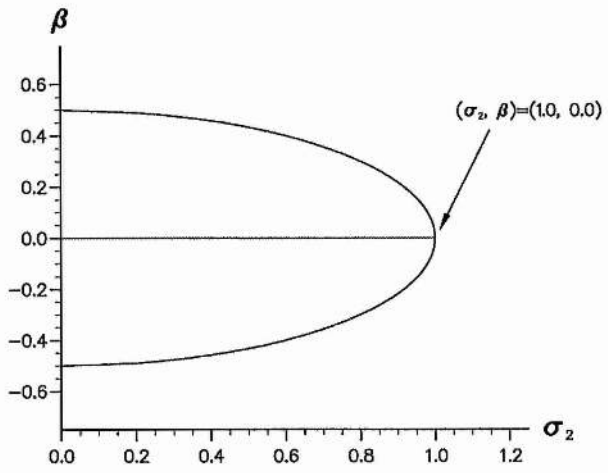

Figure 4.1: The $\sigma_2 - \beta$ plane for arbitrary σ_1 and γ.

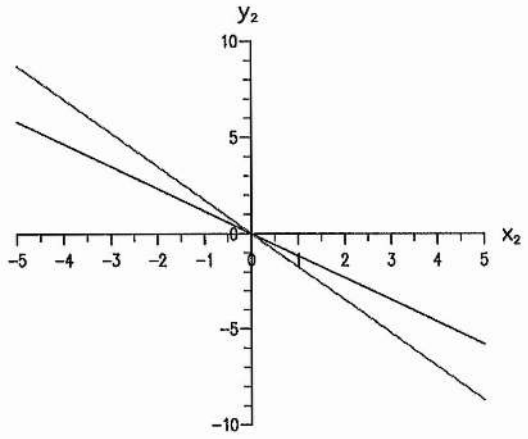

Figure 4.2: The $x_{20} - y_{20}$ plane for arbitrary σ_1 and γ.

4.3.2 Stability of the Case 1 solutions.

The fixed points of Case 1 are now subject to a local stability analysis. The evolution equations are linearized about the fixed points and their stability in the immediate region determined.

Family 1.

Here we study the stability of the origin

$$x_{10} = x_{20} = y_{10} = y_{20} = 0.$$

The linearized equations become

$$\begin{aligned}
\dot{P}_1 &= -P_1\sigma_1 + Q_1(\beta+\gamma), \\
\dot{Q}_1 &= -Q_1\sigma_1 - P_1(\beta+\gamma), \\
\dot{P}_2 &= 2\beta Q_2 + P_2(1-\sigma_2), \\
\dot{Q}_2 &= -2\beta P_2 - Q_2(1+\sigma_2),
\end{aligned}$$

giving the characteristic equation

$$\begin{vmatrix}
-\sigma_1-\lambda & (\beta+\gamma) & 0 & 0 \\
-(\beta+\gamma) & -\sigma_1-\lambda & 0 & 0 \\
0 & 0 & (1-\sigma_2)-\lambda & 2\beta \\
0 & 0 & -2\beta & -(1+\sigma_2)-\lambda
\end{vmatrix} = 0.$$

The quartic

$$(\lambda^2 + 2\lambda\sigma_2 + \sigma_2^2 - 1 + 4\beta^2)(\lambda^2 + 2\lambda\sigma_1 + \sigma_1^2 + \beta^2 + \gamma^2 + 2\beta\gamma) = 0,$$

is obtained, yielding the eigenvalues

$$\lambda = -\sigma_2 \pm \sqrt{1 - 4\beta^2} \quad \text{and} \qquad \lambda = -\sigma_1 \pm (\beta + \gamma)i.$$

These eigenvalues give the following possibilities:

Case	σ_1	σ_2	Condition	Eigenvalues
1.	$\sigma_1 > 0$	$\sigma_2 = 0$	$1 = 4\beta^2$	2 zero, 1 neg c.c.pair.
2.	$\sigma_1 > 0$	$\sigma_2 = 0$	$1 > 4\beta^2$	1 pos, 1 neg, 1 neg c.c.pair.
3.	$\sigma_1 > 0$	$\sigma_2 = 0$	$1 < 4\beta^2$	1 c.c.pair, 1 neg c.c.pair.
4.	$\sigma_1 > 0$	$\sigma_2 > 0$	$1 = 4\beta^2$	2 neg, 1 neg c.c.pair.
5.	$\sigma_1 > 0$	$\sigma_2 > 0$	$1 < 4\beta^2$	2 neg c.c.pairs.
6.	$\sigma_1 > 0$	$\sigma_2 > 0$	$1 - 4\beta^2 = \sigma_2^2$	1 zero, 1 neg, 1 neg c.c.pair.
7.	$\sigma_1 > 0$	$\sigma_2 > 0$	$0 < 1 - 4\beta^2 < \sigma_2^2$	2 neg, 1 neg c.c.pair.
8.	$\sigma_1 > 0$	$\sigma_2 > 0$	$\sigma_2^2 < 1 - 4\beta^2$	1 pos, 1 neg, 1 neg c.c.pair.

It is clear that the origin is generally attractive and acts as a sink in all cases except 2 and 8 where it acts as a saddle. The nature of the point is entirely independent of γ, with the parameter acting only to enhance the oscillatory nature in complex conjugate cases. (It should be noted that when $\sigma_1 = 0$ we obtain a

complex conjugate pair of eigenvalues with zero real part.)

Family 2.

Here we have the family of points

$$x_{10} = y_{10} = y_{20} = \beta = 0, \quad \sigma_2 = 1, \qquad \text{with} \quad x_{20}, \sigma_1, \gamma \quad \text{arbitrary.}$$

Linearization gives

$$\begin{aligned}
\dot{P}_1 &= -P_1\sigma_1 + Q_1\gamma - P_1 x_{20}, \\
\dot{Q}_1 &= -Q_1\sigma_1 - P_1\gamma + Q_1 x_{20}, \\
\dot{P}_2 &= 0, \\
\dot{Q}_2 &= -2Q_2,
\end{aligned}$$

yielding the characteristic equation

$$\begin{vmatrix}
-\lambda - \sigma_1 - x_{20} & \gamma & 0 & 0 \\
-\gamma & -\sigma_1 + x_{20} - \lambda & 0 & 0 \\
0 & 0 & -\lambda & 0 \\
0 & 0 & 0 & -2-\lambda
\end{vmatrix} = 0.$$

This gives

$$\lambda(\lambda+2)(\lambda^2 + 2\lambda\sigma_1 - x_{20}^2 + \sigma_1^2 + \gamma^2) = 0,$$

from which the eigenvalues

$$\lambda = 0, \quad \lambda = -2, \quad \lambda = -\sigma_1 \pm \sqrt{x_{20}^2 - \gamma^2}.$$

are obtained. These have the following stability properties:

Case	σ_1	Condition	Eigenvalues
1.	$\sigma_1 = 0$	$x_{20}^2 < \gamma^2$	1 zero, 1neg, 1 c.c.pair.
2.	$\sigma_1 = 0$	$x_{20}^2 > \gamma^2$	2 neg, 1 zero, 1 pos.
3.	$\sigma_1 = 0$	$x_{20}^2 = \gamma^2$	3 zero, 1 neg.
4.	$\sigma_1 > 0$	$x_{20}^2 < \gamma^2$	1 zero, 1 neg, 1 neg c.c.pair.
5.	$\sigma_1 > 0$	$0 \leq x_{20}^2 - \gamma^2 < \sigma_1^2$	3 neg, 1 zero.
6.	$\sigma_1 > 0$	$\sigma_1^2 = x_{20}^2 - \gamma^2$	2 neg, 2 zero.
7.	$\sigma_1 > 0$	$\sigma_1^2 < x_{20}^2 - \gamma^2$	2 neg, 1 pos, 1 zero.

Here, the zero root arises since there is always a family of solutions with x_{20} arbitrary. As for the other three roots, the point is predominantly stable, with all cases except 2 and 7 acting as sinks. When $\sigma_1^2 + \gamma^2 < x_{20}^2$, (i.e. the initial value of x_2 is large enough), the point becomes unstable and a saddle point results.

Family 3.

The family of points

$$x_1 = y_1 = 0, \quad \beta = \pm\frac{1}{2}(1-\sigma_2^2)^{\frac{1}{2}}, \quad x_2 = \frac{2\beta}{(\sigma_2 - 1)}y_2, \quad 0 \leq \sigma_2 < 1,$$

$$\sigma_1, \gamma \quad \text{arbitrary},$$

give the linearized equations

$$\begin{aligned}
\dot{P}_1 &= -P_1\left(\frac{2\beta}{(\sigma_2-1)}y_{20}+\sigma_1\right)+Q_1\left(\beta+\gamma-y_{20}\right),\\
\dot{Q}_1 &= Q_1\left(\frac{2\beta}{(\sigma_2-1)}y_{20}-\sigma_1\right)-P_1\left(y_{20}+\beta+\gamma\right),\\
\dot{P}_2 &= 2\beta Q_2+P_2(1-\sigma_2),\\
\dot{Q}_2 &= -2\beta P_2-Q_2(1+\sigma_2).
\end{aligned}$$

These are rewritten in the matrix form

$$\begin{pmatrix}\dot{P}_1\\ \dot{Q}_1\\ \dot{P}_2\\ \dot{Q}_2\end{pmatrix}=\begin{pmatrix}-\frac{2\beta}{(\sigma_2-1)}y_{20}-\sigma_1 & \beta+\gamma-y_{20} & 0 & 0\\ -(y_{20}+\beta+\gamma) & \frac{2\beta}{(\sigma_2-1)}y_{20}-\sigma_1 & 0 & 0\\ 0 & 0 & (1-\sigma_2) & 2\beta\\ 0 & 0 & -2\beta & -(1+\sigma_2)\end{pmatrix}\begin{pmatrix}P_1\\ Q_1\\ P_2\\ Q_2\end{pmatrix},$$

giving the characteristic equation

$$\begin{vmatrix}-\frac{2\beta}{(\sigma_2-1)}y_{20}-\sigma_1-\lambda & \beta+\gamma-y_{20} & 0 & 0\\ -(y_{20}+\beta+\gamma) & \frac{2\beta}{(\sigma_2-1)}y_{20}-\sigma_1-\lambda & 0 & 0\\ 0 & 0 & (1-\sigma_2)-\lambda & 2\beta\\ 0 & 0 & -2\beta & -(1+\sigma_2)-\lambda\end{vmatrix}=0.$$

This yields the quartic

$$\left(\lambda^2+2\sigma_1\lambda+\sigma_1^2-\frac{4\beta^2}{(\sigma_2-1)^2}y_{20}^2-y_{20}^2+(\beta+\gamma)^2\right)\left(\lambda^2+2\sigma_2\lambda+\sigma_2^2-1+4\beta^2\right)=0,$$

giving four eigenvalues

$$\lambda = -\sigma_2 \pm \sqrt{1-4\beta^2}, \tag{4.31}$$

$$\lambda = -\sigma_1 \pm \sqrt{\frac{(4\beta^2+(\sigma_2-1)^2)}{(\sigma_2-1)^2}y_{20}^2 - (\beta+\gamma)^2}. \tag{4.32}$$

Using the condition $\beta^2 = \frac{1}{4}(1-\sigma_2^2)$, (4.31) becomes

$$\lambda = 0, \qquad \lambda = -2\sigma_2, \tag{4.33}$$

with (4.32) giving

$$\lambda = -\sigma_1 \pm \sqrt{\frac{2y_{20}^2}{(1-\sigma_2)} - (\beta+\gamma)^2}. \tag{4.34}$$

These eigenvalues can be catagorised as follows:

Case	σ_1	σ_2	Condition	Eigenvalues
1.	$\sigma_1 = 0$	$\sigma_2 = 0$	$2y_{20}^2 > (\beta+\gamma)^2$	2 zero, 1 pos, 1 neg.
2.	$\sigma_1 = 0$	$\sigma_2 = 0$	$2y_{20}^2 = (\beta+\gamma)^2$	4 zero.
3.	$\sigma_1 = 0$	$\sigma_2 = 0$	$2y_{20}^2 < (\beta+\gamma)^2$	2 zero, 1 c.c.pair.
4.	$\sigma_1 = 0$	$0 < \sigma_2 < 1$	$2y_{20}^2 > (\beta+\gamma)^2(1-\sigma_2)$	1 zero, 2 neg, 1 pos.
5.	$\sigma_1 = 0$	$0 < \sigma_2 < 1$	$2y_{20}^2 = (\beta+\gamma)^2(1-\sigma_2)$	3 zero, 1 neg.
6.	$\sigma_1 = 0$	$0 < \sigma_2 < 1$	$2y_{20}^2 < (\beta+\gamma)^2(1-\sigma_2)$	1 zero, 1 neg, 1 c.c.pair.
7.	$\sigma_1 > 0$	$\sigma_2 = 0$	$2y_{20}^2 < (\beta+\gamma)^2$	2 zero, 1 neg c.c.pair.
8.	$\sigma_1 > 0$	$\sigma_2 = 0$	$0 \leq 2y_{20}^2 - (\beta+\gamma)^2 < \sigma_1^2$	2 zero, 2 neg.
9.	$\sigma_1 > 0$	$\sigma_2 = 0$	$\sigma_1^2 = 2y_{20}^2 - (\beta+\gamma)^2$	3 zero, 1 neg.
10.	$\sigma_1 > 0$	$\sigma_2 = 0$	$\sigma_1^2 < 2y_{20}^2 - (\beta+\gamma)^2$	2 zero, 1 neg, 1 pos.
11.	$\sigma_1 > 0$	$0 < \sigma_2 < 1$	$2y_{20}^2 < (\beta+\gamma)^2(1-\sigma_2)$	1 zero, 1 neg, 1 neg c.c.pair.
12.	$\sigma_1 > 0$	$0 < \sigma_2 < 1$	$0 \leq \frac{2y_{20}^2-(1-\sigma_2)(\beta+\gamma)^2}{(1-\sigma_2)}$	1 zero, 3 neg.
13.	$\sigma_1 > 0$	$0 < \sigma_2 < 1$	$\sigma_1^2 = \frac{2y_{20}^2-(1-\sigma_2)(\beta+\gamma)^2}{(1-\sigma_2)}$	2 zero, 2 neg.
14.	$\sigma_1 > 0$	$0 < \sigma_2 < 1$	$\sigma_1^2 < \frac{2y_{20}^2-(1-\sigma_2)(\beta+\gamma)^2}{(1-\sigma_2)}$	1 zero, 1 pos, 2 neg.

This point again is predominantly attractive, with cases 1, 4, 10 and 14 the only ones showing growth. This indicates that these points act as saddles with all others acting as sinks. In fact 1,4 and 10 are limiting cases of the more general 14, and as these cases show, if y_{20}^2 is sufficiently large the system becomes unstable. From 14, the threshold value needed for growth is found to be $y_{20}^2 >$

$\left(\frac{1-\sigma_2}{2}\right)[\sigma_1^2 + (\beta+\gamma)]^2$.

4.3.3 The neutral stability curve.

For the three families of case 1, $x_1 = y_1 = 0$ and we obtain a linear equation for $c_2 = x_2 + iy_2$ with damping and frequency mis-match terms only. This gives the linear stability of the flat surface to the c_2-Faraday mode, on ignoring its subharmonic. For our system the linearized Faraday equations are

$$\frac{dc_2}{dT_1} = -i2\beta c_2 + c_2^* - \sigma_2' c_2, \tag{4.35}$$

with the neutral curve, that curve separating regions where the flat surface is stable or unstable, given by

$$4\beta^2 = 1 - \sigma_2'^2.$$

For the original, unreduced system, it is found that the neutral curve is given by

$$\mu'^2 = 4\beta'^2 + \sigma_2^2,$$

where $\beta' = \frac{\Delta_2}{4}$. Figure (4.3) shows the neutral curve for $-0.5 < \beta' < 0.5$, with the flat surface being stable below the curve and unstable above it.

The first family studied in case 1, the fixed point at the origin, is just an analysis of the flat surface, with families 2 and 3 being a stability analysis of non-zero solutions on the neutral curve itself. [It should be noted that family 2 is the limiting case of family 3.]

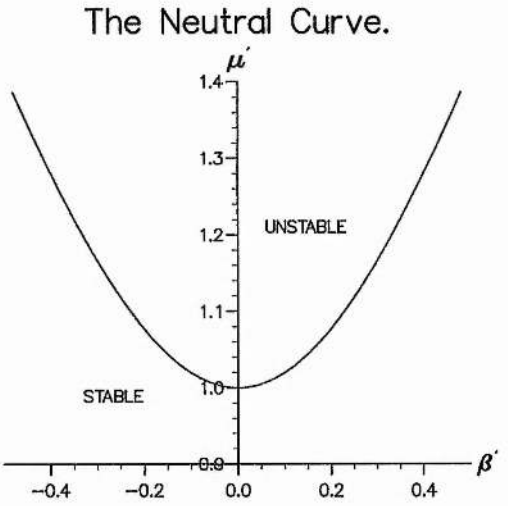

Figure 4.3: Graph showing the stability of the flat surface.

4.4 The fixed points of Case 2.

Case 2 is considerably more complicated than Case 1, with many fixed points existing in a variety of parameter ranges. It would be impractical to analyse the whole range, so attention is restricted to a few special analytical cases, together with a briefly numerical study. Two special situations we examine are the exact resonance and the undamped cases.

4.4.1 The exact resonance case.

For exact resonance we require $\beta = \gamma = 0$. The condition (4.30) holds with $\sigma_1^2 \geq 0$ always. Calculating the phases θ_1 and θ_2, (4.27) gives

$$\tan 2\theta_1 = \tan \theta_2, \tag{4.36}$$

and substitution into (4.26) yields

$$(1-\sigma_2)\tan\theta_2 = -(1+\sigma_2)\tan\theta_2.$$

The solution is

$$\theta_2 = n\pi \qquad \text{with} \qquad n \quad \text{integer},$$

and from (4.36) it follows that

$$\theta_1 = \frac{m\pi}{2} \qquad \text{with} \qquad m \quad \text{integer}.$$

To satisfy the relations for r_2 and r_1^2 we have two possibilities:

i.) m is odd with n even,

ii.) m is even with n odd.

These give the two families

A: $\theta_1 = \frac{(2M+1)\pi}{2}, \quad \theta_2 = 2N\pi, \quad r_1^2 = \sigma_1(1-\sigma_2), \quad r_2 = \sigma_1,$

B: $\theta_1 = M\pi, \quad \theta_2 = (2N+1)\pi, \quad r_1^2 = \sigma_1(1-\sigma_2), \quad r_2 = \sigma_1,$

where M and N are integers. Rewritten in the original 4-D variables, A and B become

$$\text{A}': \qquad x_{10} = y_{20} = \beta = \gamma = 0, \quad x_{20} = \sigma_1, \quad y_{10}^2 = \sigma_1(1-\sigma_2)$$

and

$$\text{B}': \qquad y_{10} = y_{20} = \beta = \gamma = 0, \quad x_{20} = -\sigma_1, \quad x_{10}^2 = \sigma_1(1-\sigma_2)$$

respectively. In both cases $\sigma_1 \geq 0$ and $0 \leq \sigma_2 \leq 1$.

From the study of Becker & Miles these families of points are known to be unstable. We found that the eigenvalues for both families are in fact identical and these can be listed as:

Case	σ_1	Conditions		Eigenvalues
1.	$\sigma_1 = 0$	N/A		2 zero, 1 neg, 1 pos.
2.	$\sigma_1 > 0$	$8\sigma_1 \leq (1-\sigma_2)$,	$16\sigma_1 \leq (2\sigma_1+\sigma_2+1)^2$	2 pos, 2 neg.
3.	$\sigma_1 > 0$	$8\sigma_1 > (1-\sigma_2)$,	$16\sigma_1 \leq (2\sigma_1+\sigma_2+1)^2$	2 neg, 1 pos c.c.pair.
4.	$\sigma_1 > 0$	$8\sigma_1 \leq (1-\sigma_2)$,	$16\sigma_1 > (2\sigma_1+\sigma_2+1)^2$	2 pos, 1 neg c.c.pair.
5.	$\sigma_1 = 0$	$8\sigma_1 > (1-\sigma_2)$,	$16\sigma_1 > (2\sigma_1+\sigma_2+1)^2$	1 pos c.c.pair, 1 neg c.c.pair.

where $0 \leq \sigma_2 < 1$.

Our stability analysis reveals that the system always has at least 1 positive and 1 negative eigenvalue. Thus in all cases we have a saddle point with stable and unstable manifolds.

4.4.2 Detuning only.

We now consider the case where the system is undamped and we have detuning only. This requires $\sigma_1 = \sigma_2 = 0$. Fixed points are possible since $(\beta+\gamma)^2 \geq 0$

satisfies (4.30). From (4.29) we obtain

$$\tan\theta_2 = \pm 1,$$

yielding

$$\tan 2\theta_1 = \mp 1$$

from (4.36). These give two distinct sets of solutions. First, when $\tan\theta_2 = 1$

$$\theta_2 = \frac{\pi}{4}, \frac{5\pi}{4} \quad \text{with} \quad \theta_1 = \frac{3\pi}{8}, \frac{7\pi}{8}, \frac{11\pi}{8}, \frac{15\pi}{8},$$

and second, when $\tan\theta_2 = -1$

$$\theta_2 = \frac{3\pi}{4}, \frac{7\pi}{4} \quad \text{with} \quad \theta_1 = \frac{\pi}{8}, \frac{5\pi}{8}, \frac{9\pi}{8}, \frac{13\pi}{8}.$$

The points within these sets now need to satisfy both

$$r_1^2 = -r_2\left(\frac{2\beta\sin\theta_2 + \cos\theta_2}{\cos 2\theta_1}\right) \quad \text{and} \quad r_1^2 = r_2\left(\frac{2\beta\cos\theta_2 + \sin\theta_2}{\sin 2\theta_1}\right),$$

such that $r_1 \geq 0$, with $r_2 = |\beta + \gamma|$.

We next consider various possibilities that satisfy these conditions. If $(\beta+\gamma) > 0$ we obtain the three cases:

1a. For $2\beta > 1$ we have 8 fixed points divided into two sets.

(i) $r_1^2 = (\beta+\gamma)(2\beta+1), \quad r_2 = (\beta+\gamma)$

$$(\theta_1, \theta_2) = \left(\tfrac{3\pi}{8}, \tfrac{\pi}{4}\right), \left(\tfrac{7\pi}{8}, \tfrac{5\pi}{4}\right), \left(\tfrac{11\pi}{8}, \tfrac{\pi}{4}\right), \left(\tfrac{15\pi}{8}, \tfrac{5\pi}{4}\right).$$

(ii) $r_1^2 = (\beta+\gamma)(2\beta-1), \quad r_2 = (\beta+\gamma)$

$$(\theta_1, \theta_2) = \left(\tfrac{\pi}{8}, \tfrac{7\pi}{4}\right), \left(\tfrac{5\pi}{8}, \tfrac{3\pi}{4}\right), \left(\tfrac{9\pi}{8}, \tfrac{7\pi}{4}\right), \left(\tfrac{13\pi}{8}, \tfrac{3\pi}{4}\right).$$

2a. For $-1 < 2\beta < 1$ we have the four fixed points given by 1a.(i),

3a. When $2\beta < -1$ we have no fixed points.

When $(\beta + \gamma) < 0$, we also obtain three cases:

1b. If $2\beta < -1$ we have 8 fixed points again divided into 2 sets.

(i) $r_1^2 = -|\beta + \gamma|(2\beta + 1), \quad r_2 = |\beta + \gamma|$

$$(\theta_1, \theta_2) = \left(\tfrac{3\pi}{8}, \tfrac{5\pi}{4}\right), \left(\tfrac{7\pi}{8}, \tfrac{\pi}{4}\right), \left(\tfrac{11\pi}{8}, \tfrac{5\pi}{4}\right), \left(\tfrac{15\pi}{8}, \tfrac{\pi}{4}\right).$$

(ii) $r_1^2 = |\beta + \gamma|(1 - 2\beta), \quad r_2 = |\beta + \gamma|$

$$(\theta_1, \theta_2) = \left(\tfrac{\pi}{8}, \tfrac{3\pi}{4}\right), \left(\tfrac{5\pi}{8}, \tfrac{7\pi}{4}\right), \left(\tfrac{9\pi}{8}, \tfrac{3\pi}{4}\right), \left(\tfrac{13\pi}{8}, \tfrac{7\pi}{4}\right).$$

2b. If $-1 < 2\beta < 1$, we obtain the four fixed points given in 1b.(ii).

3b. If $1 < 2\beta$ then we have no fixed points.

The two sets of fixed points 1a and 2a, and 1b and 2b, are plotted in figures (4.4) and (4.5), and (4.6) and (4.7) respectively. It is seen that the second set of solutions are mirror images of the first in the y_1- and x_2-axes.

It is known from the results of Becker & Miles, that points of differing energy vary in the stability properties they portray. For the case $\beta = \gamma = 1$, results from their study reveal that we would expect the points with the higher energies, 1a(i) and 1b(ii), to be stable and those with lower energies, 1a(ii) and 1b(i), to be unstable. The exact nature of this stability is considered in the next section.

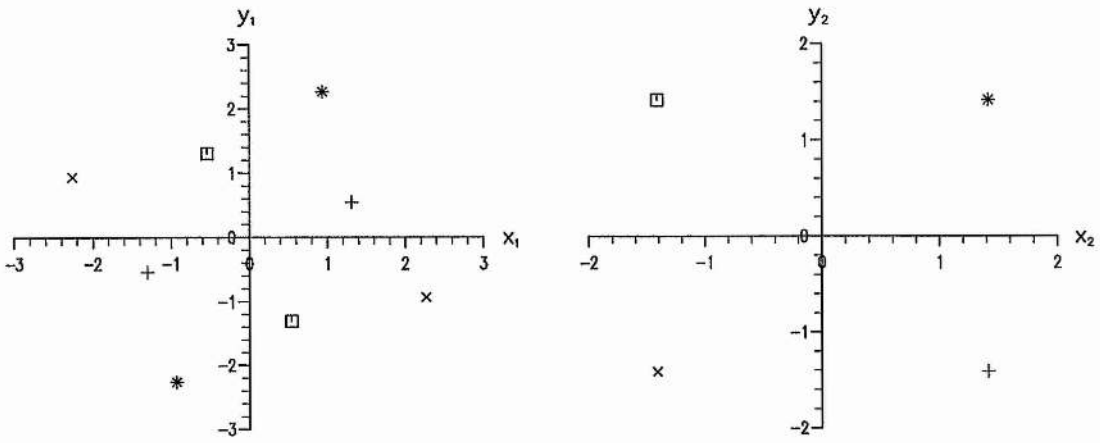

Figure 4.4: Fixed point solutions for $\sigma_1 = \sigma_2 = 0$, $\beta = 1$, $\gamma = 1$.

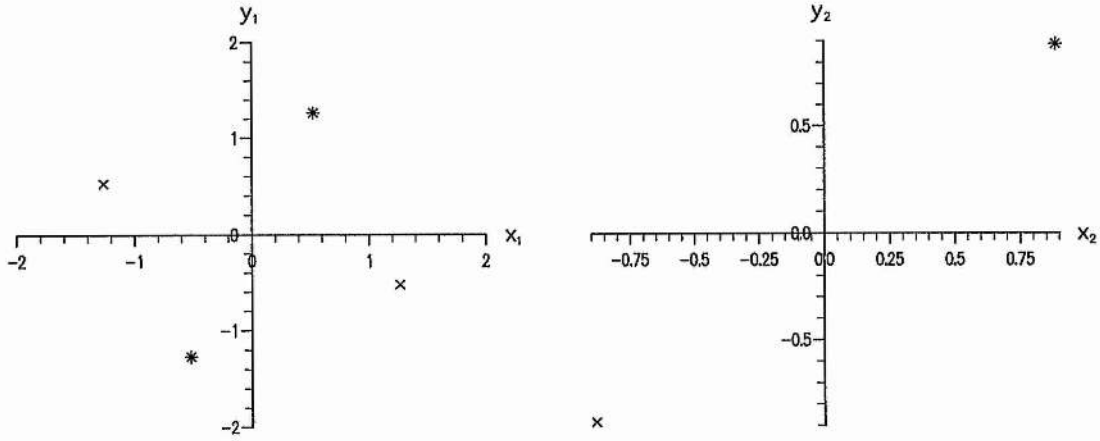

Figure 4.5: Fixed point solutions for $\sigma_1 = \sigma_2 = 0$, $\beta = 0.25$, $\gamma = 1$.

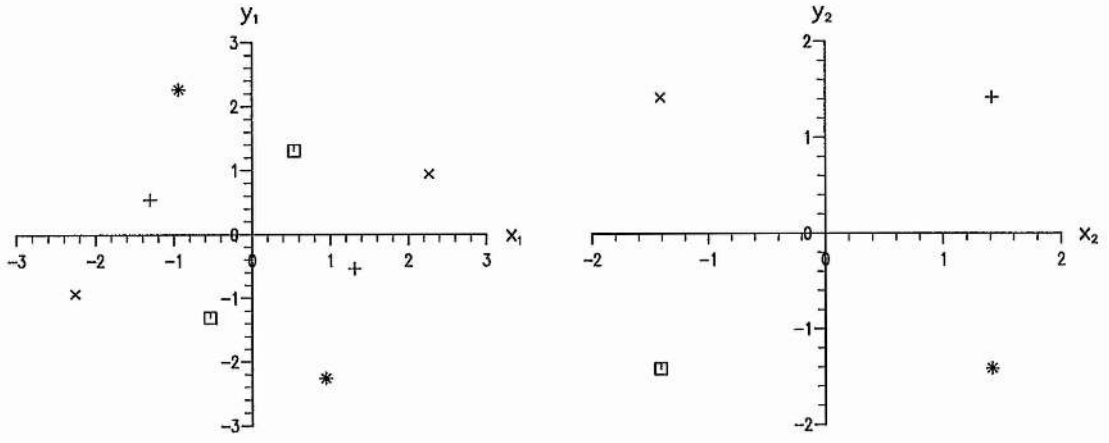

Figure 4.6: Fixed point solutions for $\sigma_1 = \sigma_2 = 0$, $\beta = -1$, $\gamma = -1$.

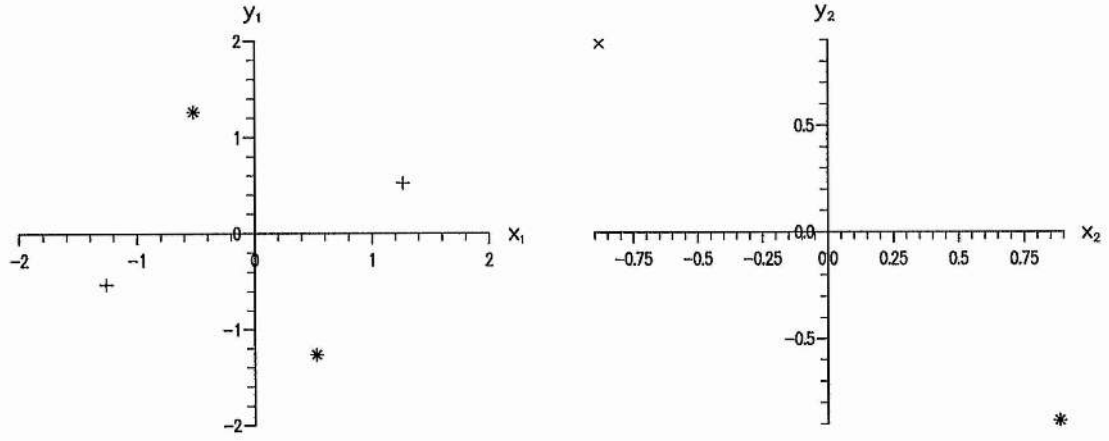

Figure 4.7: Fixed point solutions for $\sigma_1 = \sigma_2 = 0$, $\beta = -0.25$, $\gamma = -1$.

4.4.3 Stability of the above points.

Due to the nature of these points, their stability is best examined numerically. For the case $\beta = \gamma = 1$, initial coordinates are chosen close to a fixed point, with the effect of the point on the solution trajectories being determined. Examples of such trajectories are portrayed in figures (4.8) and (4.9). Examining points from 1a(i), it is found that any solution trajectory starting close to a fixed point remains so for all time. The trajectories orbit around the fixed point attracted towards it. This suggests that the system has pure complex conjugate eigenvalues, which is to be expected due to the absence of damping. The point $(x_1, y_1) = (0.9374, 2.2630)$, $(x_2, y_2) = (1.4142, 1.4142)$ is shown in figure (4.8), but all points of 1a(i) studied displayed the same behaviour.

Points from set 1a(ii) show very different properties to those of 1a(i). An example of this behaviour is pictured in figure (4.9). Here the points are clearly saddles with stable and unstable manifolds. For initial data $(x_1, y_1, x_2, y_2) = (1.5, 0.5, 1.5, -1.5)$, solution trajectories were found to leave the vicinity of a point along an unstable manifold and approach another of the points along its stable manifold. This process is repeated for all four points of 1a(ii), resulting in a closed heteroclinic orbit.

As the saddle points exist in four dimensional space, it would be expected that two other manifolds, one stable and one unstable, would be present for the

fixed points of 1a(ii). Choosing different initial data for the point examined in figure (4.9) we do indeed find such manifolds. Figure (4.10) shows trajectories for initial data $(x_1, y_1, x_2, y_2) = (1.4, 0.5, 1.4, -1.5)$. Here the trajectories do not result in closed heteroclinic orbits as before, but instead exhibit space filling properties. This is presumably due to the influence exerted by the fixed point at the origin, which strongly affects any trajectories close by. [This influence is shown more clearly in figure (4.11) for trajectories which begin at the point $(x_1, y_1, x_2, y_2) = (0.5, 0.5, 0.5, 0.5)$.]

The stationary points of 1b(i) and 1b(ii) were also examined and found to display the same properties as 1a(ii) and 1a(i) respectively. These results have therefore been omitted.

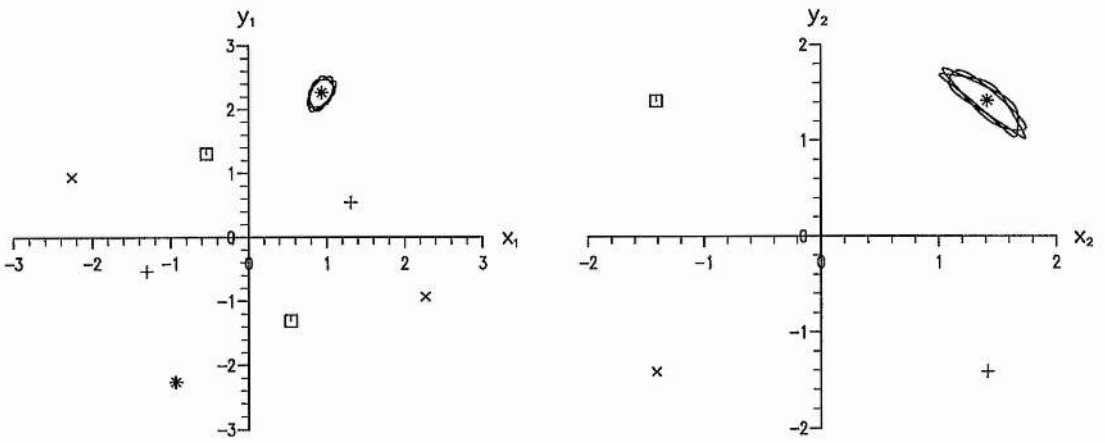

Figure 4.8: Stability of the point $(x_1, y_1) = (0.9374, 2.2630)$, $(x_2, y_2) = (1.4142, 1.4142)$ when $\sigma_1 = \sigma_2 = 0$ and $\beta = \gamma = 1$.

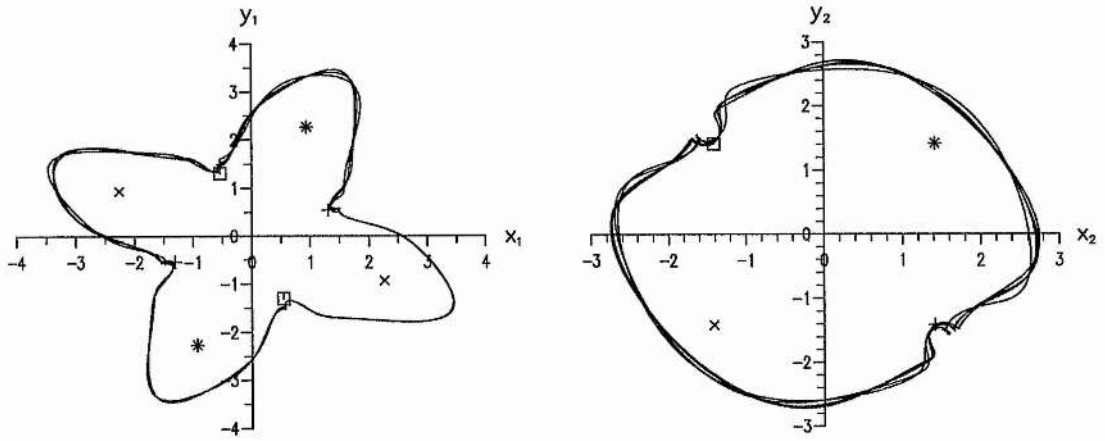

Figure 4.9: Stability of the point $(x_1, y_1) = (1.3066, 0.5412)$, $(x_2, y_2) = (1.4142, -1.4142)$ when $\sigma_1 = \sigma_2 = 0$ and $\beta = \gamma = 1$, for initial coordinates (1.5,0.5,1.5,-1.5).

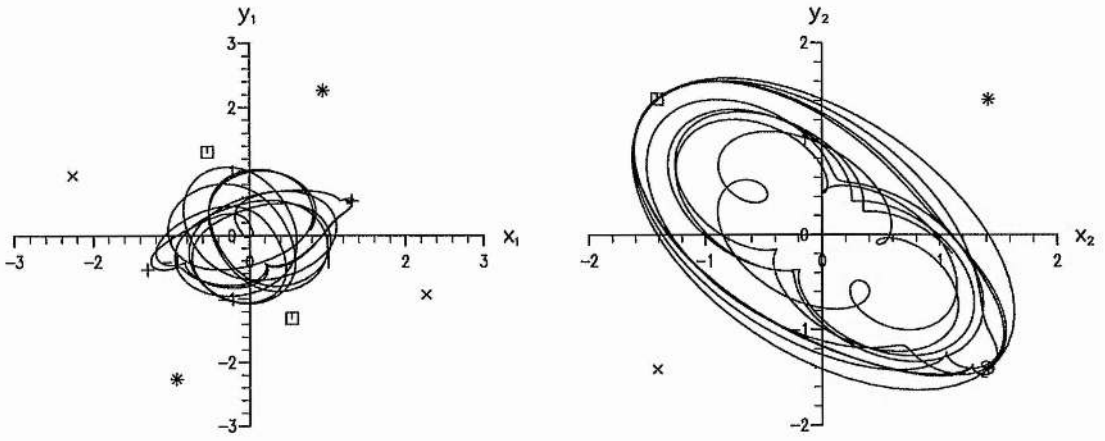

Figure 4.10: Stability of the point $(x_1, y_1) = (1.3066, 0.5412)$, $(x_2, y_2) = (1.4142, -1.4142)$ when $\sigma_1 = \sigma_2 = 0$ and $\beta = \gamma = 1$, for initial coordinates (1.4,0.5,1.4,-1.5).

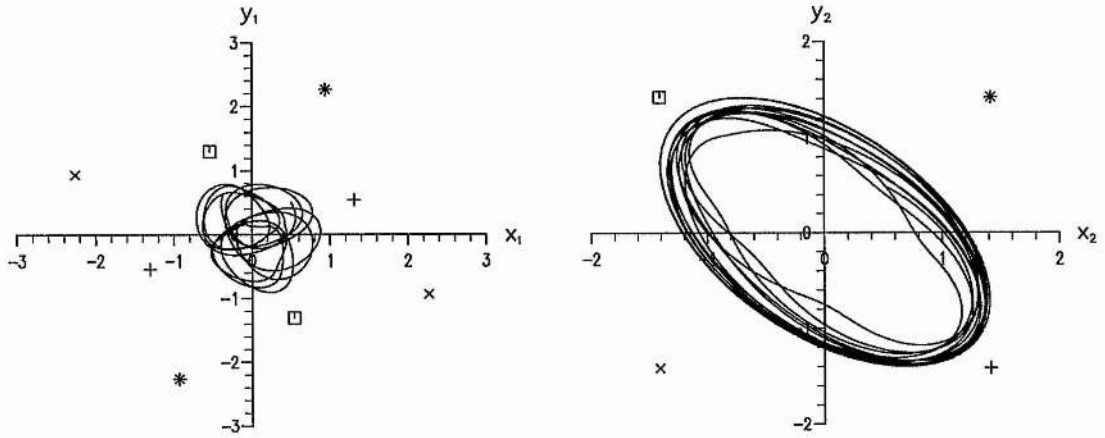

Figure 4.11: Influence of the origin when $\sigma_1 = \sigma_2 = 0$ and $\beta = \gamma = 1$, with initial coordinates (0.5,0.5,0.5,0.5).

4.5 More numerical results.

The full equations (4.3)-(4.6) are now examined numerically in cases with both detuning and damping. Due to the complexity of the points arising from Case 2, and the difficulty in isolating them, an extensive investigation would prove lengthy. Because of this the fixed points calculated for the undamped case are first used and the effects of introducing damping into the system are then considered.

As seen, the fixed points in the undamped case have both attractive and repellant properties. The absence of damping suggests that wandering chaotic trajectories may result and this is found to be so. From figures (4.12) and (4.13), it is clear that the trajectories are influenced by individual fixed points and this happens when initial data falls within the respective quarter planes and is of comparable magnitude with these points. The pair denoted by $*$ is shown to influence the solutions in figure (4.12), while the pair denoted by $\times$ influences the trajectories in figure (4.13). Initial data falling outwith corresponding quarter planes, give trajectories less-obviously effected by the points, with the chaotic appearance exaggerated.

Choosing initial data a long distance from the fixed points results in the ordered structure shown in figures (4.14) and (4.15). The points still influence the general shape of the trajectories, but on the whole this effect is small. It should be noted that we have now chosen to display graphical data in the $x_1 - y_1$

and $x_2 - y_2$ planes instead of the $x_1 - x_2$ and $y_1 - y_2$ planes as in the previous chapter. This is a natural choice as the damping coefficients to be introduced act on individual waves and not the system as a whole, also the previous graphical advantage gained will no longer apply due to the presence of fixed points.

Weak damping is now introduced into the system. The points portrayed in figure (4.16) are those which arise when $\sigma_1 = \sigma_2 = 0.1$ and $\beta = \gamma = 1$. (It should be remembered that the origin also exists as a fixed point and acts as a sink for the chosen parameters as seen in figure (4.17)). These points are found to be slightly offset from those obtained when $\sigma_1 = \sigma_2 = 0$, and a comparison between the two sets can be clearly seen in figure (4.16).

Besides the difference in location, we may also expect a change in the stability of the points. Figures (4.18) and (4.19) show the stability of two of the points when initial data is chosen to lie close to them. Figure (4.18) shows the point $(x_1, y_1, x_2, y_2) = (1.01824, 2.21738, 1.58212, 1.22756)$ and this is found act as a sink. This is not surprising, since the equivalent point in the undamped case, figure (4.8), was seen to have pure imaginary c.c. eigenvalues. All the points marked $\bullet$ in figure (4.18) were found to display similar behaviour.

A different type of behaviour is shown by the point portrayed in figure (4.19). The corresponding point in figures (4.9) and (4.10) was found to act as a saddle and that in figures (4.19) and (4.20) shows similar instability. In figure (4.19) we have a case with chosen initial data equivalent to that of figure (4.10). The

trajectories are found to spiral in towards the origin, which is not surprising since any trajectory passing close to a stable point is bound to be drawn into it. The oscillatory nature of the trajectories suggest that the eigenvalues for the origin take the form of two complex conjugate pairs with negative real part, and this is confirmed from the table on page 95. Using slightly different initial data $(x_1, y_1, x_2, y_2) = (1.5, 0.7, 1.6, -1.5)$ we seek to find similarities with the heteroclinic orbits in figure (4.9). As figure (4.20) shows, the damping is too strong for any such similarity to exist, and the trajectories are quickly attracted to the nearest stable point. On decreasing the damping considerably, figure (4.21), vestiges of such orbits can again be found. In figure (4.21) both damping coefficients have been reduced to 0.001. For a short time the type of behaviour seen in figure (4.9) is again found, but after visiting three saddle points the orbits break become attracted to the origin after long enough time. Again all points marked by $\times$ were found to have the same properties.

More general initial coordinates are portrayed in figures (4.22) and (4.23). Figure (4.22) corresponds to the same initial data as figure (4.12). As seen the wandering trajectories are no longer as persistent as before, since they are attracted strongly to the origin. With damping a similar result is found to occur for the initial data used in figure (4.13). For different initial values, the solution trajectories may again be attracted to one of the other fixed points. In figure (4.23) the solutions at first wander exotically around a fixed point, but as en-

ergy is removed from the system due to damping, they become attracted to it. Although attractive, further numerics suggest that this point is not as strong an attractor as the origin, but as seen, the destination of solution trajectories in the damped case depend largely on initial values.

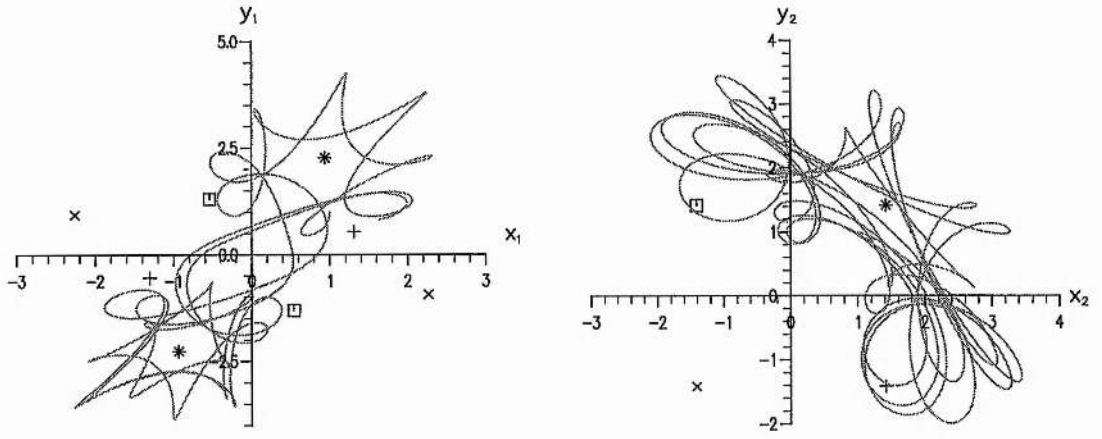

Figure 4.12: Solution trajectories for initial $(x_{10}, y_{10}, x_{20}, y_{20}) = (1, 1, 1, 1)$ when $\sigma_1 = \sigma_2 = 0$ and $\beta = \gamma = 1$.

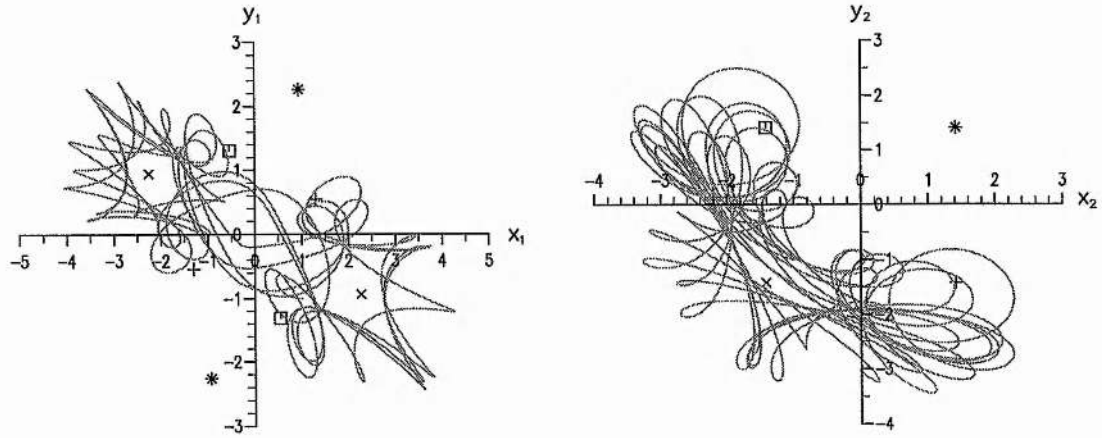

Figure 4.13: Solution trajectories for initial $(x_{10}, y_{10}, x_{20}, y_{20}) = (1, -1, -1, -1)$ when $\sigma_1 = \sigma_2 = 0$ and $\beta = \gamma = 1$.

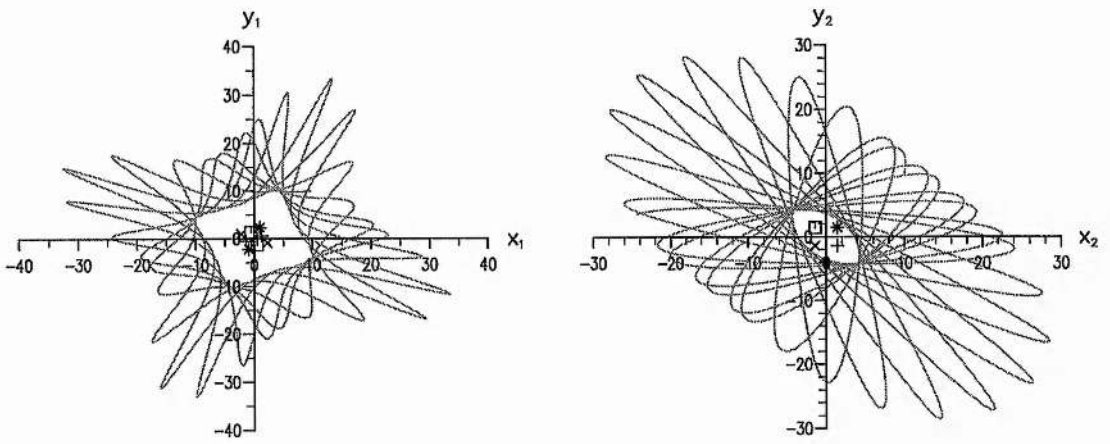

Figure 4.14: Solution trajectories for initial $(x_{10}, y_{10}, x_{20}, y_{20}) = (10, 10, 10, 10)$ when $\sigma_1 = \sigma_2 = 0$ and $\beta = \gamma = 1$.

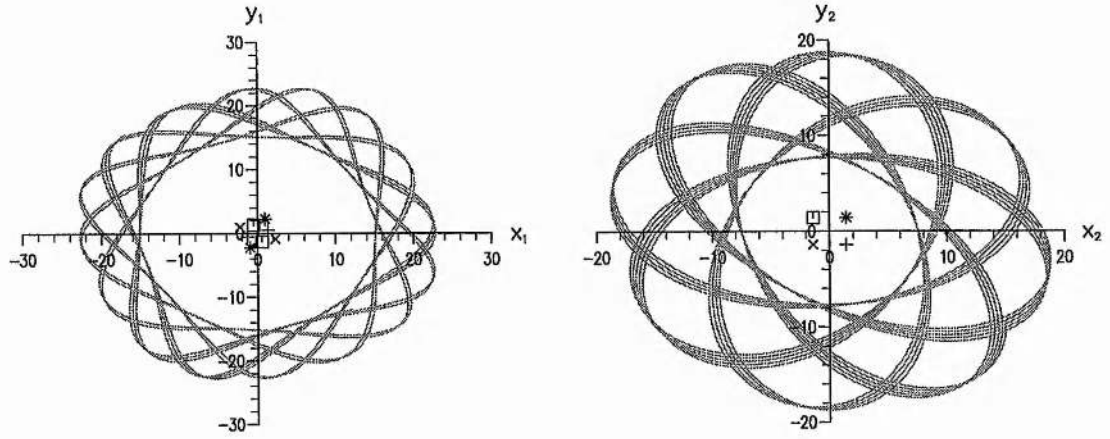

Figure 4.15: Solution trajectories for initial $(x_{10}, y_{10}, x_{20}, y_{20}) = (12, -12, 15, -10)$ when $\sigma_1 = \sigma_2 = 0$ and $\beta = \gamma = 1$.

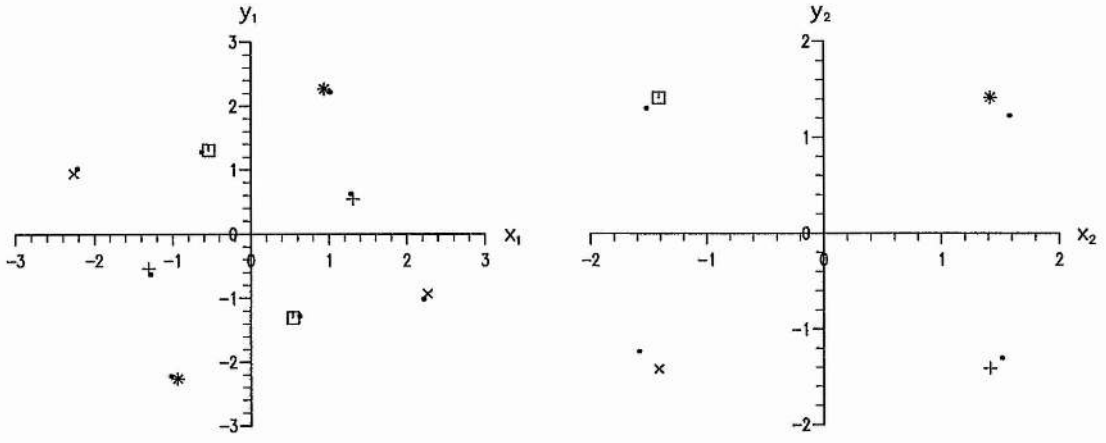

Figure 4.16: Comparison of fixed point solutions between $\sigma_1 = \sigma_2 = 0$ (as before) and $\sigma_1 = \sigma_2 = 0.1$ (shown by the small dot) when $\beta = 1 = \gamma = 1$.

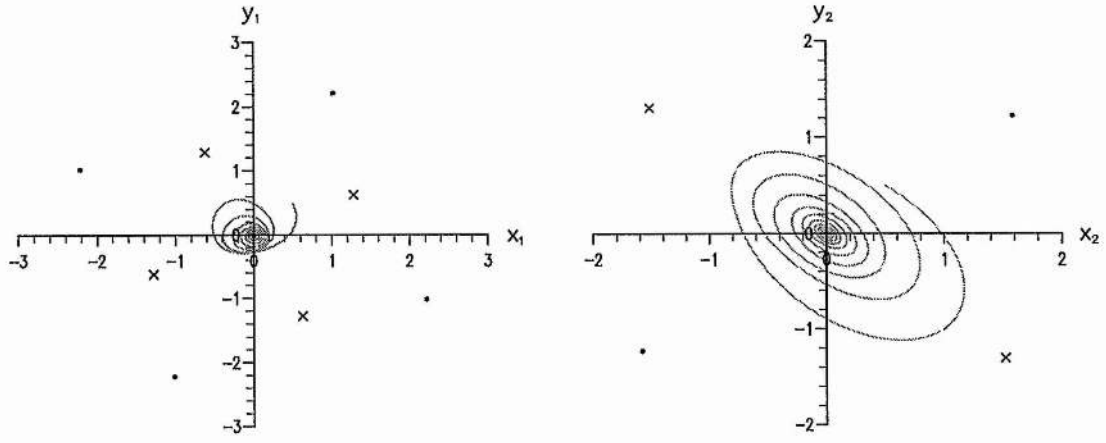

Figure 4.17: Stability of the fixed point at the origin for $\sigma_1 = \sigma_2 = 0.1$ when $\beta = \gamma = 1$.

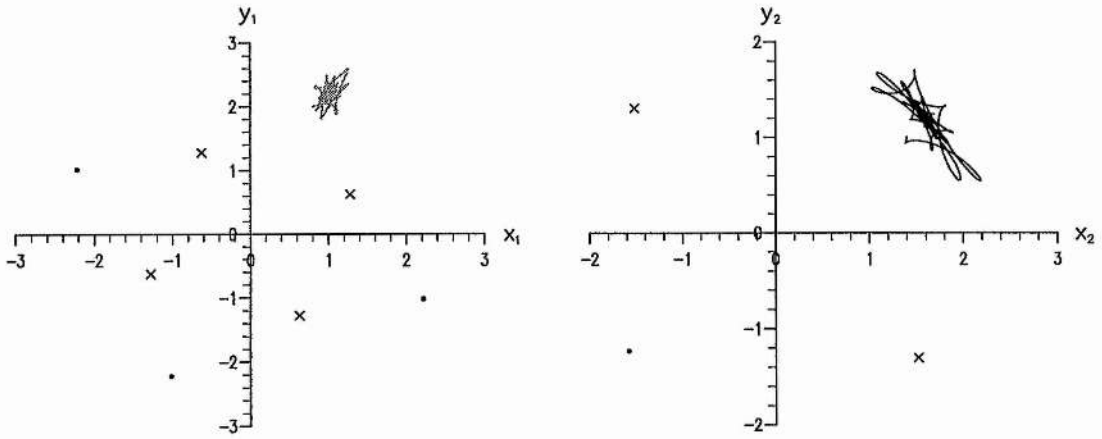

Figure 4.18: Stability of the fixed point $(x_1, y_2) = (1.01824, 2.21738)$, $(x_2, y_2) = (1.58212, 1.22756)$ when $\sigma_1 = \sigma_2 = 0.1$ and $\beta = \gamma = 1$.

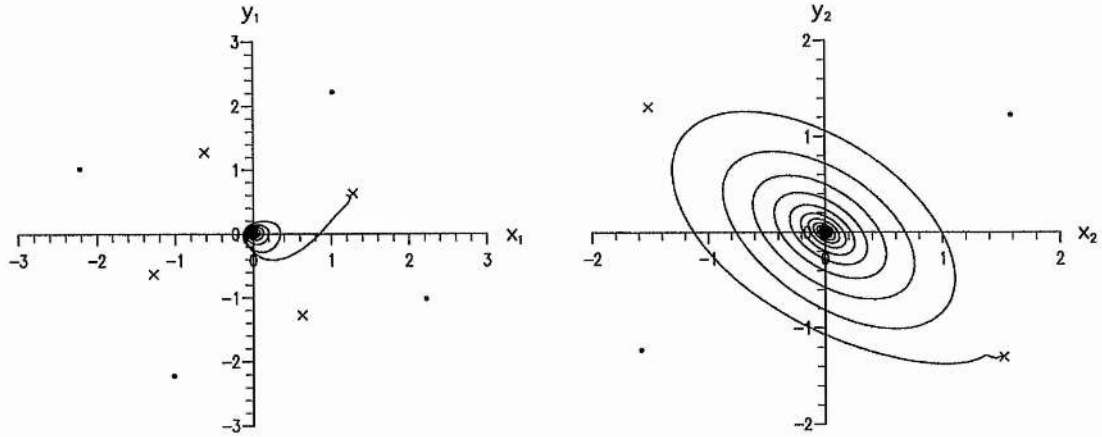

Figure 4.19: Stability of the fixed point $(x_1, y_2) = (1.27880, 0.6264)$, $(x_2, y_2) = (1.51885, -1.30503)$ when $\sigma_1 = \sigma_2 = 0.1$ and $\beta = \gamma = 1$, with initial coordinates (1.2,0.6,1.5,-1.3)

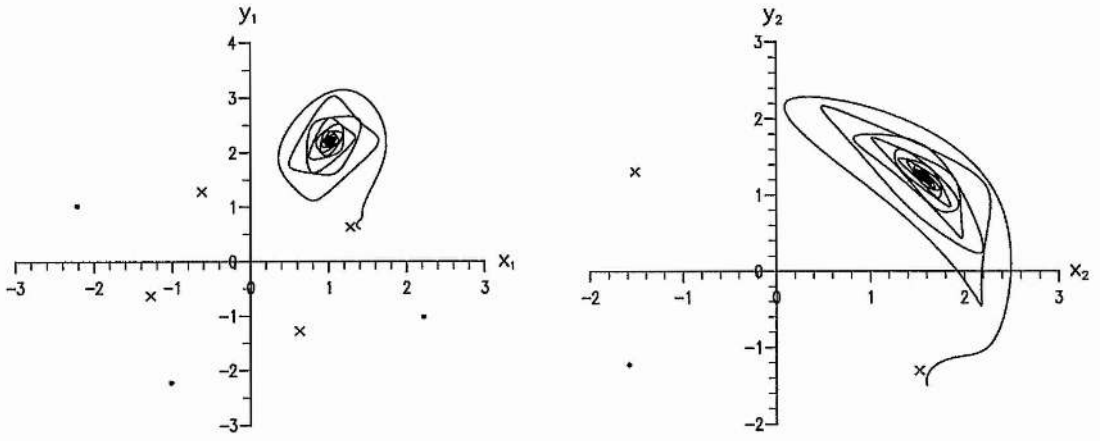

Figure 4.20: Stability of the fixed point $(x_1, y_2) = (1.27880, 0.6264)$, $(x_2, y_2) = (1.51885, -1.30503)$ when $\sigma_1 = \sigma_2 = 0.1$ and $\beta = \gamma = 1$, with initial coordinates (1.5,0.7,1.6,-1.5)

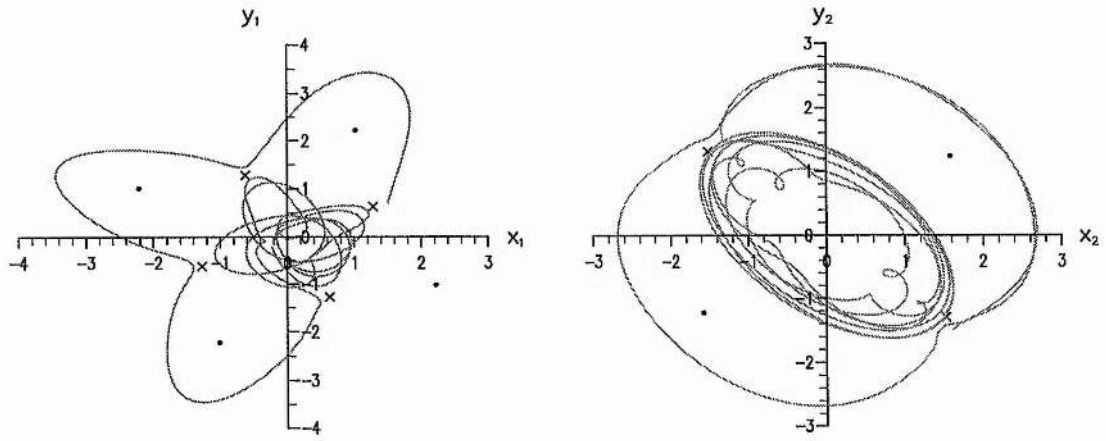

Figure 4.21: Stability of the fixed point $(x_1, y_2) = (1.27880, 0.6264)$, $(x_2, y_2) = (1.51885, -1.30503)$ when $\sigma_1 = \sigma_2 = 0.001$ and $\beta = \gamma = 1$, with initial coordinates (1.4,0.7,1.6,-1.5).

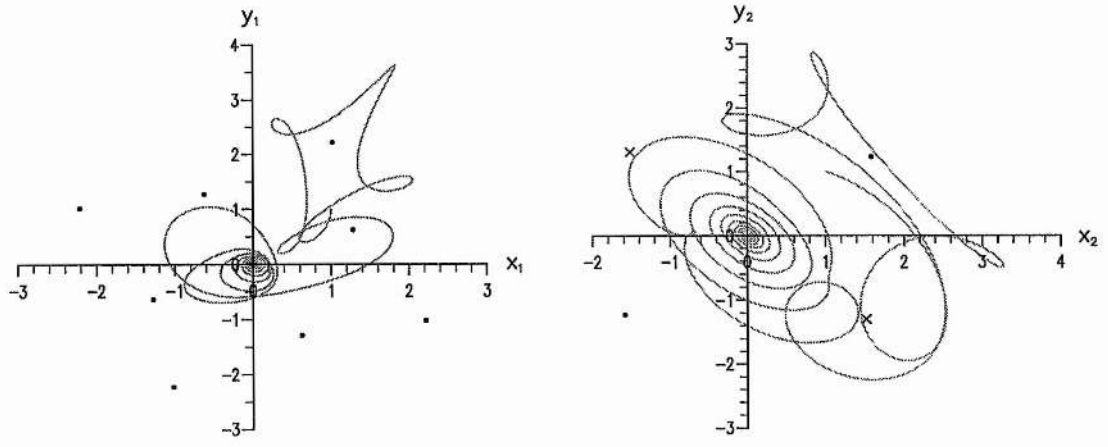

Figure 4.22: Solution trajectories for initial $(x_{10}, y_{10}, x_{20}, y_{20}) = (1, 1, 1, 1)$ when $\sigma_1 = \sigma_2 = 0.1$ and $\beta = \gamma = 1$.

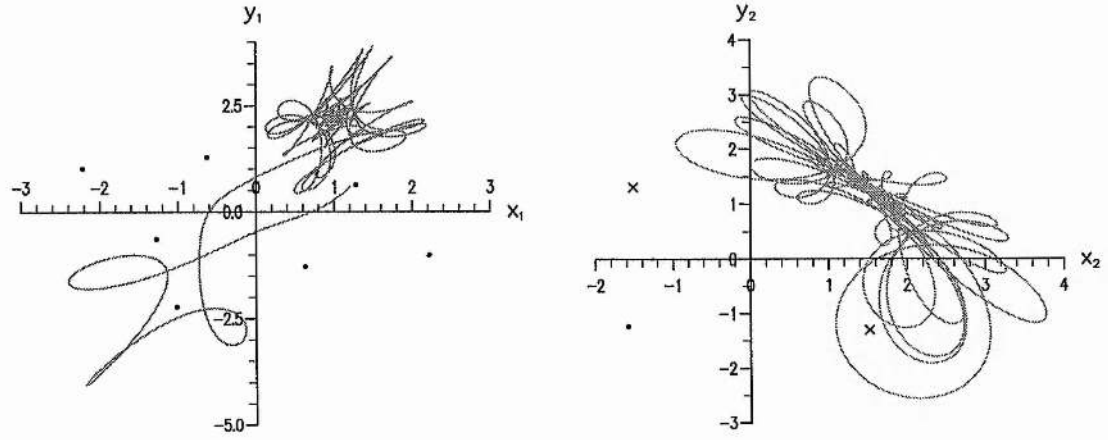

Figure 4.23: Solution trajectories for initial $(x_{10}, y_{10}, x_{20}, y_{20}) = (1.2, 0.6, 1.5, 1.3)$ when $\sigma_1 = \sigma_2 = 0.1$ and $\beta = \gamma = 1$.

4.6 Conclusions.

The fixed points and solution trajectories that appear in the off-resonance and damped system display interesting behaviour. In the absence of damping we find a host of oscillatory and chaotically wandering solutions. For initial data close to one of the saddle points, closed heteroclinic orbits may be found. Here a series of saddle points become joined along their stable and unstable manifolds, with the other fixed points having little influence on the solution trajectories.

The introduction of viscous damping sees the neutrally stable points develop into sinks. The saddles remain unstable and any closed orbits that may have existed are found to break down. For any degree of damping it is found that the solution trajectories end at one of the stable points if the detuning is great enough.

Due to the complexity of the fixed point solutions, it is impractical to give a full account of all the behaviours possible. A sample of these has been highlighted for special cases and this should provide a firm base for any further investigation.

Chapter 5

Introduction to flows with uniform strain rates.

5.1 General review.

Kelvin (1887) presented a method for solving the linearized equations governing small disturbances in unbounded plane Couette flow. The solutions took the form of wave modes which were either periodic in, or independent of, each space co-ordinate. Orr (1907a,b) described these modes in more detail, but it was not until the latter half of this century that the implications of Kelvin's solution were more thoroughly examined.

Craik & Criminale (1986), whilst developing a procedure for finding classes of exact solutions for the Navier-Stokes equations, discovered that a single 'Kelvin

mode' was in fact an exact solution. Besides the unbounded parallel flows examined by Kelvin, Craik & Criminale also studied flows that were non-parallel but which were characterized by spatially uniform shearing rates. see also Langnado, Phen-Thein & Leal (1984). Such flows were shown to give rise to a wide class of exact solutions as well as incorporating the linear 'Kelvin modes'.

A special case of the two-dimensional flows studied by Craik & Criminale, that with elliptical streamlines and constant vorticity, was examined numerically by Pierrehumbert (1986). He discovered such flows gave rise to strong three-dimensional instabilities with exponential growth and this growth was estimated numerically. Pierrehumbert's observations led Bayly (1986) to examine this system analytically, in a manner similar to Craik & Criminale, but quite independently. Bayly discovered that the two-dimensional inviscid flow was experiencing a resonance mechanism due to the periodic distortion of certain plane-wave modes. This resonance was associated with a Floquet-type instability, and the Floquet exponents obtained by Bayly coincided with the approximate growth rates obtained by Pierrehumbert. This work was subsequently followed by Landman & Saffman (1987) who, using Craik & Criminale's earlier analysis, incorporated viscosity into Bayly's system.

Waleffe (1990) also considered the three-dimensional instability of a two-dimensional flow with elliptical streamlines. Instead of undertaking the type of numerical investigation conducted by Bayly, Waleffe focused on obtaining a

more physical description for the instability mechanism. This question was indeed interesting, especially as Malkus (1989) suggested that the three-dimensional breakdown of such flows might play an important role in the planetary dynamo problem. Waleffe discovered that the stability of an elliptical flow was governed by an Ince equation and this allowed analytic extensions, in particular, the construction of localized solutions.

Craik (1989) extended this earlier work to include body forces. Although Craik & Criminale had included such forces in their general formulation, their results were obtained without their presence. Craik followed through this formulation and gave an account of the exact solutions that existed. A more detailed study was concentrated on Bayly's inviscid Floquet instability. Here Craik found that the effect of a Coriolis force on such elliptical flows was highly significant. Instability was found to be present for all except a narrow band of rotation speeds and the strength of the instability was also found to vary according to the amount of rotation.

Craik & Allen (1992) extended the Floquet analysis of Bayly to investigate the stability of certain three-dimensional time-periodic flows. These flows had spatially uniform but time-periodic strain rates and when the flow was symmetric about the axis of rotation, it was found that inviscid plane-wave disturbances were governed by a Hill's equation. When the strain rates were small, the Hill's equation reduced to a Mathieu's equation and the principal bands of instability

could be found analytically. However, for larger rates of strain the problem had to be looked at numerically. They expressed their Hill's equation as a pair of first-order differential equations. To this system Floquet theory was applied and various instability bands were numerically isolated. It was found that in general the growth rates of the main bands could be large, but those for the higher-order bands tended to be much smaller.

A further class of time-periodic flows, namely those within a rotating and precessing axisymmetric ellipsoid, was examined by Kerswell (1993). Motivated by an earlier analysis by Poincaré (1910), Kerswell found that a rotating reference frame could be chosen within which the given flows were steady. This resulted in the analysis again reducing to a Floquet problem at the expense only of introducing a Coriolis force.

While a Floquet approach was suitable for examining disturbance equations containing a periodic function, the method became unavailable when the equations contained quasi-periodic terms. Craik & Allen (1992) noted that this was the case for their non-axisymmetric basic flows, but whilst examining the special case of small amplitude forcing, they found that the more general case could not yet be addressed.

Bayly, Holm & Lifschitz (1995) recently re-visited this problem, when they considered two families of two-dimensional flows with time-periodic strain rates. Using theoretical studies of the Schrödinger equation with quasi-periodic poten-

tials, [Johnson & Moser (1982), Moser & Poschel (1982) and Simon (1982)], they developed a convincing computational method that determined the stability of such systems after computations over large time. The first class of flows examined contained a steady elliptical flow as a limiting case, but in general it led to a potential that contained functions with two periods. When these periods were rationally related, Floquet theory could be used to confirm the numerical results. It was found that several distinct instability bands existed, with one of these much stronger and wider than the rest. When the periods became irrationally related, the number of bands became infinite. Only a few of these could be detected numerically and the system was shown to be highly unstable to three-dimensional plane-wave disturbances.

The second class of flows considered by Bayly et al. was a family of time-periodic, uniform-vorticity cores associated with externally-strained Kirchoff-Kida vortices (Kida 1981). Again this class of flows was found to be highly unstable.

5.1.1 Outline of the problem.

Another class of flows that can be investigated using a computational method similar to that developed by Bayly et al. (1995) are those of the form of three-dimensional unbounded time-periodic flows with fixed ellipsoidal stream-surfaces. Stability of steady and uniformly precessing ellipsoids has been examined by Gledzer & Ponomarev (1992) and Kerswell (1993), and the problem of time-

periodic flows was posed, but not solved, by Craik (1995). Here we study such a flow. Section 5.2 discusses the mathematical background surrounding such study and Chapter 6 proceeds with a stability analysis of the system.

5.2 Mathematical review.

To formulate our problem, notation similar to that used by Craik & Criminale (1986) is adopted. As always with such systems, the governing equations of the flow are the incompressible Navier-Stokes equations. When body force is excluded these read

$$\frac{\partial u_i}{\partial t} + u_j \frac{\partial u_i}{\partial x_j} = -\frac{1}{\rho}\frac{\partial p}{\partial x_i} + \nu \frac{\partial^2 u_i}{\partial x_j \partial x_j} \tag{5.1}$$

$$\frac{\partial u_j}{\partial x_j} = 0. \tag{5.2}$$

Here the equations are expressed in Cartesian tensor form with $x_i (i = 1, 2, 3)$ representing the Cartesian space co-ordinates and $u_i (i = 1, 2, 3)$ being the flow field. There is summation over repeated indices ($j = 1, 2, 3$). The pressure is denoted by p, the density by ρ, the kinematic viscosity by ν and time by t.

The flow field u_i is now decomposed into a basic flow U_i and a plane-wave disturbance u_i' in such a way that $u_i = U_i + u_i'$. U_i is chosen so that it depends linearly on the space co-ordinates as

$$U_i(x_i, t) = \sigma_{ij}(t) x_j + U_i^{(0)}(t) \qquad (i, j = 1, 2, 3). \tag{5.3}$$

Here $U_i^{(0)}$ denotes the instantaneous velocity of the basic flow at the origin and the disturbance is taken to have the form

$$u_i'(x_i, t) = \mathrm{Re}\{v_i(t) \exp[i\alpha_j(t)x_j]\} \tag{5.4}$$

with $\boldsymbol{\alpha}(t) \equiv \{\alpha_i(t)\}$ being a time-dependent wavenumber.

It is known, [see Craik & Criminale (1986)], that, since the basic flow (5.3) satisfies the Navier-Stokes equations, then the matrix $\boldsymbol{S}(t) \equiv \{\sigma_{ij}\}$ must satisfy the relations

$$\dot{\boldsymbol{S}}(t) + \boldsymbol{S}^2(t) = \boldsymbol{M}(t), \qquad \mathrm{tr}[\boldsymbol{S}(\mathrm{t})] = 0,$$

where tr denotes the trace of the matrix and $\boldsymbol{M}(t)$ is an arbitrary symmetric matrix. Body forces may simply be included in the above equation by the addition of a single term only. [see Craik (1989), Miyazaki & Fukumoto (1992)].

As shown by Craik & Criminale, the wavenumber $\boldsymbol{\alpha}(t)$ of the disturbance (5.4) must satisfy

$$\dot{\boldsymbol{\alpha}} = -\mathbf{S}^{\mathrm{T}}\boldsymbol{\alpha} \tag{5.5}$$

where $\boldsymbol{S}^T$ is the transpose of $\boldsymbol{S}$. This equation represents advection of the disturbance by the primary flow in such a way that material planes remain plane at all later times, though with differing orientation. The momentum equation (5.1) for the disturbance velocity components $\boldsymbol{v}(t)$, then has the form

$$\dot{\boldsymbol{v}}(t) + \boldsymbol{S}\boldsymbol{v}(t) + \nu(\boldsymbol{\alpha} \cdot \boldsymbol{\alpha})\boldsymbol{v}(t) = 0. \tag{5.6}$$

Equation (5.6) can be related to the inviscid limit $\boldsymbol{u}(t)$ by the incorporation of a damping factor

$$\boldsymbol{v}(t) = \exp\left\{-\nu \int_0^t (\boldsymbol{\alpha}\cdot\boldsymbol{\alpha})dt\right\}\boldsymbol{u}(t).$$

[c.f. Craik & Criminale (1986), Landman and Saffman (1987)].

The inviscid velocity components then satisfy

$$\dot{\boldsymbol{u}} + \Pi\boldsymbol{u} = 0 \qquad\qquad \Pi = \{\tau_{ij}\} \tag{5.7}$$

where

$$\tau_{ij} = \sigma_{ij} - \frac{2\alpha_i\alpha_k\sigma_{kj}}{(\boldsymbol{\alpha}\cdot\boldsymbol{\alpha})} \qquad \text{when} \qquad \mathbf{S} \equiv \{\sigma_{ij}\}.$$

By continuity we also have $\boldsymbol{u}\cdot\boldsymbol{\alpha} = 0$, i.e.

$$u_1\alpha_1 + u_2\alpha_2 + u_3\alpha_3 = 0, \tag{5.8}$$

which can be used to reduce the expressions

$$\dot{u}_1 = -\sigma_{1j}u_j + \frac{2\alpha_1\alpha_k\sigma_{kj}u_j}{(\boldsymbol{\alpha}\cdot\boldsymbol{\alpha})} \tag{5.9}$$

$$\dot{u}_2 = -\sigma_{2j}u_j + \frac{2\alpha_2\alpha_k\sigma_{kj}u_j}{(\boldsymbol{\alpha}\cdot\boldsymbol{\alpha})} \tag{5.10}$$

$$\dot{u}_3 = -\sigma_{3j}u_j + \frac{2\alpha_3\alpha_k\sigma_{kj}u_j}{(\boldsymbol{\alpha}\cdot\boldsymbol{\alpha})} \tag{5.11}$$

to coupled equations for two variables.

Chapter 6

Time-dependent flows with ellipsoidal stream-surfaces.

6.1 Mathematical introduction to the problem.

The case we are concerned with is when the basic flow is time-periodic and confined along ellipsoidal stream-surfaces

$$\left(\frac{x}{a}\right)^2 + \left(\frac{y}{b}\right)^2 + \left(\frac{z}{c}\right)^2 = \text{constant}.$$

In this instance possible primary flows with spatially-uniform strain rates are

$$U_i(x_i, t) = \boldsymbol{S}(t) x_j$$

where

$$\mathbf{S}(t) = \begin{pmatrix} 0 & \frac{a\omega_3}{b} & -\frac{a\omega_2}{c} \\ -\frac{b\omega_3}{a} & 0 & \frac{b\omega_1}{c} \\ \frac{c\omega_2}{a} & -\frac{c\omega_1}{b} & 0 \end{pmatrix} \tag{6.1}$$

[see Craik (1989), Gledzer & Ponomarev (1992)].

Here the $\omega_i's$ represent one half the vorticity of the flow and are determined by the three coupled equations

$$\dot{\omega}_1 = \frac{c^2 - b^2}{c^2 + b^2}\omega_2\omega_3 \tag{6.2}$$

$$\dot{\omega}_2 = \frac{a^2 - c^2}{a^2 + c^2}\omega_3\omega_1 \tag{6.3}$$

$$\dot{\omega}_3 = \frac{b^2 - a^2}{b^2 + a^2}\omega_1\omega_2. \tag{6.4}$$

[c.f. Euler's equations for rigid body rotation]. For the wavenumber $\boldsymbol{\alpha}(t)$, (5.5) gives

$$\frac{d}{dt}\begin{pmatrix} a\alpha_1 \\ b\alpha_2 \\ c\alpha_3 \end{pmatrix} = \begin{pmatrix} 0 & \omega_3 & -\omega_2 \\ -\omega_3 & 0 & \omega_1 \\ \omega_2 & -\omega_1 & 0 \end{pmatrix}\begin{pmatrix} a\alpha_1 \\ b\alpha_2 \\ c\alpha_3 \end{pmatrix}, \tag{6.5}$$

yielding a further three coupled equations

$$\dot{\alpha}_1 = \frac{\omega_3 b}{a}\alpha_2 - \frac{\omega_2 c}{a}\alpha_3 \tag{6.6}$$

$$\dot{\alpha}_2 = -\frac{\omega_3 a}{b}\alpha_1 + \frac{\omega_1 c}{b}\alpha_3 \tag{6.7}$$

$$\dot{\alpha}_3 = \frac{\omega_2 a}{c}\alpha_1 - \frac{\omega_1 b}{c}\alpha_2 \tag{6.8}$$

which depend on the ω_i's from (6.2)-(6.4).

6.2 Reduction of the system.

6.2.1 Elimination of the velocity components.

We now seek to reduce equations (5.9), (5.10) and (5.11) into two coupled equations. To do this we introduce the dependent variables

$$P \equiv \alpha_1 u_2 - \alpha_2 u_1, \qquad Q \equiv |\boldsymbol{\alpha}(0)| u_3. \tag{6.9}$$

It is easily seen that

$$\dot{P} = \dot{\alpha}_1 u_2 - \dot{\alpha}_2 u_1 + \alpha_1 \dot{u}_2 - \alpha_2 \dot{u}_1 \tag{6.10}$$

and using equations (6.6), (6.7), (5.9) and (5.10) in (6.10), we obtain the expression

$$\dot{P} = u_3 \left[-\alpha_3 \omega_3 \left(\frac{b}{a} + \frac{a}{b} \right) - \frac{\alpha_2 \omega_2 a}{c} - \frac{\alpha_1 \omega_1 b}{c} \right] - c\alpha_3 \left(\frac{u_1 \omega_1}{b} + \frac{u_2 \omega_2}{a} \right).$$

Next the u_j components are eliminated explicitly from this expression using the relations (5.8) and (6.9). This gives

$$\begin{aligned} \dot{P} = -\frac{c\alpha_3 P}{(\alpha_1^2 + \alpha_2^2)} \left(\frac{\alpha_1 \omega_2}{a} - \frac{\alpha_2 \omega_1}{b} \right) + \frac{Q}{|\boldsymbol{\alpha}(0)|} \Bigg[-\alpha_3 \omega_3 \left(\frac{b}{a} + \frac{a}{b} \right) \\ -\alpha_2 \omega_2 \left(\frac{a}{c} - \frac{c\alpha_3^2}{a(\alpha_1^2 + \alpha_2^2)} \right) - \alpha_1 \omega_1 \left(\frac{b}{c} - \frac{c\alpha_3^2}{b(\alpha_1^2 + \alpha_2^2)} \right) \Bigg]. \end{aligned} \tag{6.11}$$

The second of the required relations is, from (5.11) and (6.9),

$$\dot{Q} = |\boldsymbol{\alpha}(0)|\dot{u}_3 = |\boldsymbol{\alpha}(0)| \left[-\sigma_{3j}u_j + \frac{2\alpha_3\alpha_k\sigma_{kj}u_j}{(\boldsymbol{\alpha}\cdot\boldsymbol{\alpha})} \right],$$

i.e.

$$\begin{aligned} \dot{Q} = |\boldsymbol{\alpha}(0)| \Bigg[& u_1 \left(-\frac{c\omega_2}{a} - \frac{2b\alpha_2\alpha_3\omega_3}{a(\boldsymbol{\alpha}\cdot\boldsymbol{\alpha})} + \frac{2c\alpha_3^2\omega_2}{a(\boldsymbol{\alpha}\cdot\boldsymbol{\alpha})} \right) \\ & + u_2 \left(\frac{c\omega_1}{b} + \frac{2a\alpha_1\alpha_3\omega_3}{b(\boldsymbol{\alpha}\cdot\boldsymbol{\alpha})} - \frac{2c\alpha_3^2\omega_1}{b(\boldsymbol{\alpha}\cdot\boldsymbol{\alpha})} \right) \\ & + u_3 \left(\frac{2\alpha_3}{(\boldsymbol{\alpha}\cdot\boldsymbol{\alpha})} \left(-\frac{a\alpha_1\omega_2}{c} + \frac{b\alpha_2\omega_1}{c} \right) \right) \Bigg]. \end{aligned} \tag{6.12}$$

From (5.8) and (6.9) we obtain the two relations

$$\alpha_2 P = -\left(\alpha_1\alpha_3 u_3 + u_1(\alpha_1^2 + \alpha_2^2) \right)$$

and

$$\alpha_1 P = u_2(\alpha_1^2 + \alpha_2^2) + \alpha_2\alpha_2 u_3,$$

which upon use of $u_3 = \frac{Q}{|\boldsymbol{\alpha}(0)|}$ yields

$$\begin{aligned} u_1 &= \left(\frac{-1}{\alpha_1^2 + \alpha_2^2} \right) \left(\alpha_2 P + \frac{\alpha_1\alpha_3 Q}{|\boldsymbol{\alpha}(0)|} \right) \\ u_2 &= \left(\frac{1}{\alpha_1^2 + \alpha_2^2} \right) \left(\alpha_1 P - \frac{\alpha_2\alpha_3 Q}{|\boldsymbol{\alpha}(0)|} \right), \end{aligned}$$

With a little rearranging equation (6.12) is now rewritten

$$\begin{aligned}\dot{Q} &= \frac{|\boldsymbol{\alpha}(0)|P}{\alpha_1^2+\alpha_2^2}\left[\frac{c(\alpha_1^2+\alpha_2^2-\alpha_3^2)}{(\boldsymbol{\alpha}\cdot\boldsymbol{\alpha})}\left(\frac{\omega_1\alpha_1}{b}+\frac{\omega_2\alpha_2}{a}\right)+\frac{2\alpha_3\omega_3}{(\boldsymbol{\alpha}\cdot\boldsymbol{\alpha})}\left(\frac{\alpha_1^2 a}{b}+\frac{\alpha_2^2 b}{a}\right)\right] \\ &+ \frac{Q\alpha_3}{(\alpha_1^2+\alpha_2^2)(\boldsymbol{\alpha}\cdot\boldsymbol{\alpha})}\left[c(\alpha_1^2+\alpha_2^2-\alpha_3^2)\left(\frac{\alpha_1\omega_2}{a}-\frac{\alpha_2\omega_1}{b}\right)\right. \\ &+ \left.\frac{2(\alpha_1^2+\alpha_2^2)}{c}(-\alpha_1 a\omega_2+\alpha_2 b\omega_1)+2\alpha_1\alpha_2\alpha_3\omega_3\left(\frac{b}{a}-\frac{a}{b}\right)\right] \qquad (6.13)\end{aligned}$$

and equations (6.11) and (6.13) can be expressed in the form

$$\begin{pmatrix}\dot{P}\\ \dot{Q}\end{pmatrix}=\begin{pmatrix}r_{11} & r_{12}\\ r_{21} & r_{22}\end{pmatrix}\begin{pmatrix}P\\ Q\end{pmatrix}, \qquad (6.14)$$

where the $r_{ij}(t)$ are obtained from the above expressions.

6.2.2 Reduction to polar form.

We now seek to express the system (6.14) in a form similar to that obtained by Bayly *et al* (1995), so that their techniques may be manipulated. As in this earlier study, polar variables are introduced such that

$$P+iQ=\rho e^{i\phi}. \qquad (6.15)$$

This gives

$$\dot{\rho}=\cos\phi\dot{P}+\sin\phi\dot{Q}$$

from which we obtain

$$\dot{\rho} = \rho \left[r_{11} \cos^2 \phi + r_{22} \sin^2 \phi + (r_{12} + r_{21}) \sin \phi \cos \phi \right]. \tag{6.16}$$

Supposing we let $\rho = \rho(0) e^{s(t)}$, equation (6.16) will then give

$$\dot{s} = r_{11} \cos^2 \phi + r_{22} \sin^2 \phi + (r_{12} + r_{21}) \sin \phi \cos \phi$$

and upon use of trigonometric identities this yields

$$\dot{s} = \left(\frac{r_{11} - r_{22}}{2} \right) \cos 2\phi + \left(\frac{r_{12} + r_{21}}{2} \right) \sin 2\phi + \left(\frac{r_{11} + r_{22}}{2} \right). \tag{6.17}$$

Looking next for an expression for $\dot{\phi}$, we note from (6.15) that

$$\frac{dP}{dt} = \frac{d(\rho \cos \phi)}{dt} = \dot{\rho} \cos \phi - \rho \sin \phi \dot{\phi} = (\dot{s} \cos \phi - \dot{\phi} \sin \phi) \rho,$$

giving from (6.14),

$$\dot{\phi} \sin \phi = \dot{s} \cos \phi - r_{11} \cos \phi - r_{12} \sin \phi,$$

leading to

$$\dot{\phi} = -r_{12} + \cot \phi \left[\left(\frac{r_{11} - r_{22}}{2} \right) (\cos 2\phi - 1) + \left(\frac{r_{12} + r_{21}}{2} \right) \sin 2\phi \right],$$

on using (6.17). We therefore have the two equations

$$\dot{\phi} = \left(\frac{r_{12} + r_{21}}{2} \right) \cos 2\phi - \left(\frac{r_{11} - r_{22}}{2} \right) \sin 2\phi + \left(\frac{r_{21} - r_{12}}{2} \right), \tag{6.18}$$

$$\dot{s} = \left(\frac{r_{12} + r_{21}}{2} \right) \sin 2\phi + \left(\frac{r_{11} - r_{22}}{2} \right) \cos 2\phi + \left(\frac{r_{11} + r_{22}}{2} \right), \tag{6.19}$$

where

$$
\begin{aligned}
r_{11}+r_{22} &= \frac{\alpha_3}{(\alpha_1^2+\alpha_2^2)(\boldsymbol{\alpha}\cdot\boldsymbol{\alpha})}\left[2\alpha_2\omega_1\left(\frac{c\alpha_3^2}{b}+\frac{(\alpha_1^2+\alpha_2^2)b}{c}\right)\right.\\
&+ \left. 2\alpha_1\alpha_2\alpha_3\omega_3\left(\frac{b}{a}-\frac{a}{b}\right)-2\alpha_1\omega_2\left(\frac{c\alpha_3^2}{a}+\frac{a(\alpha_1^2+\alpha_2^2)}{c}\right)\right],\\
r_{11}-r_{22} &= \frac{2\alpha_3}{(\boldsymbol{\alpha}\cdot\boldsymbol{\alpha})}\left[\alpha_2\omega_1\left(\frac{c}{b}-\frac{b}{c}\right)+\alpha_1\omega_2\left(\frac{a}{c}-\frac{c}{a}\right)-\frac{\alpha_1\alpha_2\alpha_3\omega_3}{(\alpha_1^2+\alpha_2^2)}\left(\frac{b}{a}-\frac{a}{b}\right)\right],\\
r_{21}\pm r_{12} &= \frac{|\boldsymbol{\alpha}(0)|}{(\alpha_1^2+\alpha_2^2)(\boldsymbol{\alpha}\cdot\boldsymbol{\alpha})}\left[(\alpha_1^2+\alpha_2^2-\alpha_3^2)c\left(\frac{\omega_1\alpha_1}{b}+\frac{\omega_2\alpha_2}{a}\right)\right.\\
&+ \left. 2\alpha_3\omega_3\left(\frac{\alpha_1^2 a}{b}+\frac{\alpha_2^2 b}{a}\right)\right]\pm\frac{1}{|\boldsymbol{\alpha}(0)|}\left[-\alpha_1\omega_1\left(\frac{b}{c}-\frac{c\alpha_3^2}{b(\alpha_1^2+\alpha_2^2)}\right)\right.\\
&- \left.\alpha_2\omega_2\left(\frac{a}{c}-\frac{c\alpha_3^2}{a(\alpha_1^2+\alpha_2^2)}\right)-\alpha_3\omega_3\left(\frac{b}{a}+\frac{a}{b}\right)\right]. \qquad (6.20)
\end{aligned}
$$

From the theory of quasi-periodic potentials, as exploited by Bayly *et al* (1995), the limit

$$W=\lim_{t\to\infty}\left(\frac{\phi(t)}{t}\right) \qquad (6.21)$$

can be shown to exist. This is called the 'winding number' of the potential and is independent of the initial value $\phi(0)$. The limit

$$I=\lim_{t\to\infty}\left(\frac{s(t)}{t}\right) \qquad (6.22)$$

similarly exists and this is known as the 'growth rate'. For instability to occur it is sufficient that $I>0$, since I is in fact the average exponential growth rate. The procedure for investigating this requirement is described subsequently.

6.2.3 Reduction to Schrödinger form.

Before examining the stability of the system (6.14), we first need to justify the existence of our limits (6.21) and (6.22) by relating them to the linear Schrödinger equation, [for which appropriate theorems are available: see Johnson & Moser (1982), Moser & Poschel (1982), Simon (1982).] Initially (6.14) needs to be formulated as a second-order differential equation. To do this the system is re-written as

$$\left(\frac{d}{dt} - r_{11}\right) P = r_{12} Q \tag{6.23}$$

$$\left(\frac{d}{dt} - r_{22}\right) Q = r_{21} P. \tag{6.24}$$

The substitution of (6.23) into (6.24) next yields

$$\left(\frac{d}{dt} - r_{22}\right)\left(\frac{1}{r_{12}}\frac{d}{dt} - \frac{r_{11}}{r_{12}}\right) P = r_{21} P,$$

giving

$$\ddot{P} + \left(\frac{\dot{r}_{12}}{r_{12}} - r_{11} - r_{22}\right)\dot{P} + \left(r_{11}r_{22} - r_{12}\frac{d}{dt}\left(\frac{r_{11}}{r_{12}}\right) - r_{12}r_{21}\right) P = 0. \tag{6.25}$$

This equation is of the form

$$\ddot{P} + p(t)\dot{P} + q(t)P = 0,$$

where $p(t)$ and $q(t)$ are quasi-periodic functions. On setting

$$P(t) = S(t)v(t), \tag{6.26}$$

where $v(t)$ is the integrating factor

$$v(t) = \exp\left[-\frac{1}{2}\int p(t)dt\right], \tag{6.27}$$

this gives

$$\ddot{S}(t) + I(t)S(t) = 0$$

in which

$$I(t) = q(t) - \frac{1}{2}\dot{p}(t) - \frac{1}{4}p^2(t).$$

Our resultant second-order differential equation therefore becomes

$$\ddot{S} + \left(r_{11}r_{22} - r_{12}\frac{d}{dt}\left(\frac{r_{11}}{r_{12}}\right) - r_{12}r_{21} - \frac{1}{2}\frac{d}{dt}\left(p(t)\right) - \frac{1}{4}\left(p(t)\right)^2\right)S = 0, \tag{6.28}$$

where

$$p(t) = \frac{\dot{r}_{12}}{r_{12}} - r_{11} - r_{22}.$$

Equation (6.28) is now of a Schrödinger form and this can be written as

$$\ddot{S} + d(t)S = 0, \tag{6.29}$$

where $d(t)$ is a quasi-periodic potential. A certain amount of theory exists about such potentials and this is now employed to relate the Schrödinger results to those of our equation (6.25).

It is known [Moser & Poschel (1984)] that for (6.29) a winding number μ exists such that

$$\mu(\lambda) = \lim_{t\to\infty}\frac{1}{t}\arg\left(\dot{S}(t,\lambda) + iS(t,\lambda)\right), \tag{6.30}$$

where λ is the long time average of $d(t)$. From (6.26) we have

$$S(t) = P(t)v^{-1}(t),$$

giving

$$\dot{S}(t) = \dot{P}(t)v^{-1}(t) - P(t)v^{-2}(t)\dot{v}(t). \tag{6.31}$$

and from this we obtain

$$\arg(\dot{S} + iS) = \tan^{-1}\left(\frac{S}{\dot{S}}\right) = \cot^{-1}\left(\frac{\dot{P} - \frac{P\dot{v}}{v}}{P}\right).$$

Differentiating (6.27) gives

$$\dot{v}(t) = -\frac{1}{2}p(t)v(t),$$

and (6.31) then becomes

$$\arg(\dot{S} + iS) = \cot^{-1}\left(\frac{\dot{P}}{P} - \frac{1}{2}p(t)\right). \tag{6.32}$$

Defining $\arg(\dot{S} + iS) = \theta$ we now have

$$\cot\theta = \left(\frac{\dot{P}}{P} - \frac{1}{2}p(t)\right). \tag{6.33}$$

For the system we are examining we have

$$P + iQ = \rho e^{i\phi},$$

which gives

$$\arg(P + iQ) = \phi.$$

From (6.23) we also have

$$Q = \frac{\dot{P}}{r_{12}} - \frac{r_{11}P}{r_{12}}.$$

Therefore

$$\arg(P + iQ) = \tan^{-1}\frac{1}{r_{12}}\left(\frac{\dot{P}}{P} - r_{11}\right),$$

yielding

$$\tan\phi = \frac{1}{r_{12}}\left(\frac{\dot{P}}{P} - r_{11}\right). \tag{6.34}$$

Combining equations (6.33) and (6.34) it is easily seen that

$$r_{12}\cot\theta - r_{12}^2\tan\phi = \frac{1}{2}r_{22}r_{12} + \frac{3}{2}r_{11}r_{12} + \frac{1}{2}\dot{r}_{12}. \tag{6.35}$$

The r.h.s. of this equation is quasi-periodic and thus bounded. Due to this a strong correlation exists between the phases θ and ϕ, if $\cot\theta \to \pm\infty$ then likewise $\tan\phi \to \pm\infty$. Thus ϕ and θ must exhibit the same asymptotic properties and the winding number of one is closely related to that of the other. The existence of our limits (6.21) and (6.22) can therefore be confidently asserted and we proceed with our analysis.

6.3 Numerical results.

In order to find the limits, the sets of equations (6.2)-(6.4) for $\boldsymbol{\omega}$, (6.6)-(6.8) for $\boldsymbol{\alpha}$, then (6.18) and (6.19), are integrated numerically over sufficiently large times that the limits (6.21) and (6.22) are approached convincingly. We can take

$|\omega(0)| = 1$, $|\alpha(0)| = 1$ and one of the $\alpha_j(0) = 0$ without loss of generality. By choosing $\alpha_2(0)$ to be equal to zero, we can introduce the variable θ such that $\alpha_1(0) = \sin\theta$ and $\alpha_3(0) = \cos\theta$. Here the angle θ represents the angle between the initial wavevector of the disturbance and the z co-ordinate axis. The initial values $s(0)$ and $\phi(0)$ can also be taken as zero without loss as the limits are independent of these values.

Upon declaration of the variables $\omega_{1,2}(0)$, and a, b, c, a numerical integration is initiated, generally over a time $t = 1000$, and this was found to be sufficient for satisfactory convergence. The integration comprised a Merson form of the explicit Runga-Kutta method and consisted of a sequence of steps whose sizes were adapted throughout the integration in order that the final result should lie within a tolerance of 10^{-10}. Values of θ were chosen between 0 and $\frac{\pi}{2}$ at intervals of 0.005 until the time limit was reached, and graphs were then plotted of $\cos\theta$ against the large-time limits of $\frac{s(t)}{t}$ and $\frac{\phi(t)}{t}$ respectively.

In order to see if the integration was proceeding correctly, a number of numerical checks were introduced into the program. These checks were of the form of relations obtained from earlier equations. Looking back at equations (6.2), (6.3) and (6.4) it is seen that, when integrated, these equations provide us with the relation

$$(c^2 + b^2)\omega_1^2 + (a^2 + c^2)\omega_2^2 + (b^2 + a^2)\omega_3^2 = \text{constant}. \tag{6.36}$$

At all stages of the integration the above relation must hold and this gave us a

check on the values that the routine was generating for the ω_i's. A similar relation is also derived to verify the values being generated for the α_i's. It is known that

$$\hat{\boldsymbol{\alpha}} \cdot (\hat{\boldsymbol{\alpha}} \times \dot{\boldsymbol{\omega}}) = 0$$

where $\hat{\boldsymbol{\alpha}} = (a\alpha_1, b\alpha_2, c\alpha_3)$, and this gives

$$\hat{\boldsymbol{\alpha}} \cdot \dot{\hat{\boldsymbol{\alpha}}} = 0 \qquad \Rightarrow \qquad \frac{1}{2}\frac{d}{dt}(\hat{\boldsymbol{\alpha}} \cdot \hat{\boldsymbol{\alpha}}) = 0.$$

Therefore

$$\frac{1}{2}\frac{d}{dt}(a^2\alpha_1^2 + b^2\alpha_2^2 + c^2\alpha_3^2) = 0$$

giving

$$a^2\alpha_1^2 + b^2\alpha_2^2 + c^2\alpha_3^2 = \text{constant}. \tag{6.37}$$

Thus we have the two equations (6.36) and (6.37) which confirmed the accuracy of our computations at various stages during the integration.

The case examined in detail is when (a,b,c)=(3,2,1), but others may be done similarly. Throughout we chose $\omega_2(0) = 0$, with the evolution of the unstable regions being shown as the initial values of ω_1 and ω_3 are altered. This does entail some loss of generality, but other choices yield similar results. Figures (6.1) and (6.2) show the stability properties when $\omega_1(0) = 0$ and $\omega_3(0) = 1$. This corresponds to a purely elliptical fluid flow centred around the z-axis, with no fluid rotation around the x or y axes. Here our system is equivalent to the Floquet case examined by Bayly (1986) and, in the special case of no body force,

by Craik (1989). Figures (6.1) clearly shows that one instability band exists for the region $0.45 < \theta < 0.68$ and this is confirmed by (6.2) where the winding number is constant in the unstable region. These results are in agreement with the theory and with the results obtained by Craik.

We now examine what happens when the basic motion of the fluid is not purely in the $x-y$ planes. To do this a small initial component of rotation $\omega_1(0)$, about the x-axis, is imposed. This has the result of introducing a time-periodicity into the basic fluid flow which causes a marked change in the stability of the system. Figures (6.3) and (6.4) show such a case. Here two more instability bands have appeared on either side of the main band. These new bands have a maximum growth rate considerably smaller than that of the original and they span a much smaller range of initial wavevectors.

In fact, the calculation of the winding number, pictured in figure (6.4), breaks down for small θ. This corresponds to the case of the initial disturbance wavevector lying almost along the z-axis. At this instant we begin to obtain inaccuracies with the numerics due to α_1 and α_2 passing through, or very close to, zero at the same time. This causes problems with the calculation of the expressions (6.20) because of the numerous divisions by the $\alpha_1^2+\alpha_2^2$ terms. The situation is discussed in more detail in the next section, but for the moment we will just outline the solution.

The problem was overcome by setting up the same system relative to different

coordinates. This was achieved by switching the x-axis and z-axis and also the a and c components of the ellipsoid. The same numerical integration was then performed, but this time, due to the switch of axes, the initial conditions ω_{10} and ω_{30} were interchanged and the growth rates and winding numbers were plotted against $\sin\theta$ instead of $\cos\theta$. This method produces an identical growth rate to before, but the winding number will not be the same quantity. As figure (6.5) clearly shows, the change of coordinates has eliminated the breakdown of numerics, this time close to $\theta = \frac{\pi}{2}$. The analysis of the system remains unaffected by the change in the winding number, with both figures (6.4) and (6.5) showing the same characteristic features. We now continue to investigate the stability properties of the system and, for simplicity, these are described in the original coordinates.

Increasing the initial component of fluid rotation about the x-axis we see that many smaller instability bands begin to become apparent and the three main bands continue to grow. Figures (6.12) and (6.13) show such a case. Here some of these bands are not large to be resolved clearly by figure (6.13), but as we increase the initial x-rotation these bands become much more evident. With a further increase in the initial x-rotation, some of the smaller instability bands can not now be isolated by the resolution employed previously. Figures (6.14) and (6.15) have been produced using an enhanced resolution. Here values of θ were chosen at intervals of 0.001 instead of 0.005 and the extra data points generated

were found to be sufficient to pick up some of the smaller bands.

The fluid flows are clearly highly unstable to most disturbances. Figures (6.16) and (6.17) show the stability when an initial x-axis rotation equivalent to $\omega_1(0) = 0.5$ is chosen. An instability band is now found for almost every angle of θ over $\frac{\pi}{6}$ radians and much sharper resolution still is needed at this stage to examine the rich structure of bands that exist. Figures (6.18) and (6.19) have been produced using intervals of 0.0005 over a region of figures (6.16) and (6.17) with $\cos\theta$ between 0.54 and 0.75. These figures show clearly the complex structure of this interval, but even at this higher resolution it is impossible to show exactly the large number of stability bands that exist. Indeed they are likely to be dense in some sections.

Attention is now switched to the situation when the initial fluid rotation is purely around the x-axis. This is shown in figures (6.20) and (6.21). Again the system reduces to a Floquet problem, but here the instability occurs over smaller values of θ and a larger growth rate than that shown in figure (6.1). When a rotation is introduced around the z-axis, the plots of growth rate and winding number change dramatically. Figure (6.22) shows many more instability bands becoming evident and the system quickly becomes extremely unstable as the initial z-rotation is increased. At this stage we again begin to experience numerical problems, with the winding number depicted in (6.23) no longer monotonic. Due to this graphs showing a further increase in initial z-rotation are omitted.

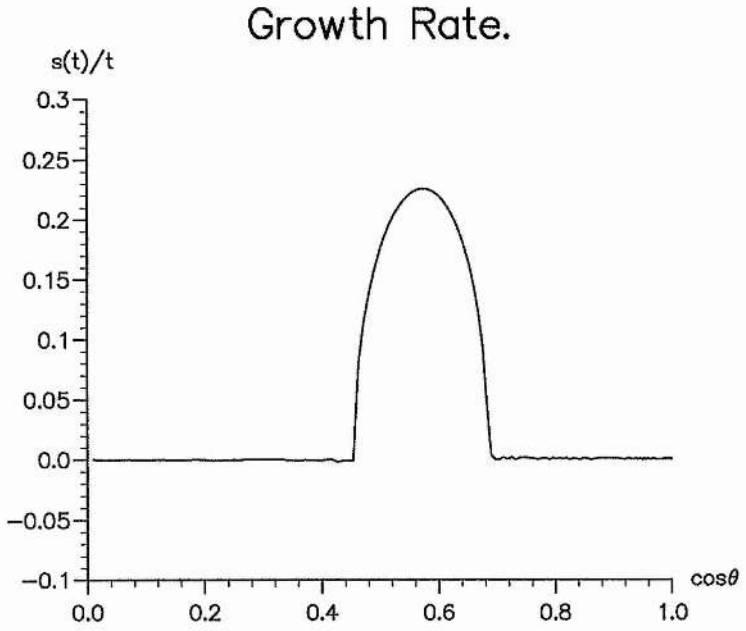

Figure 6.1: Graph showing the regions of stability for $\omega_1(0) = 0$ and $\omega_3(0) = 1$. Here the axes of the ellipsoid are $(a, b, c) = (3, 2, 1)$.

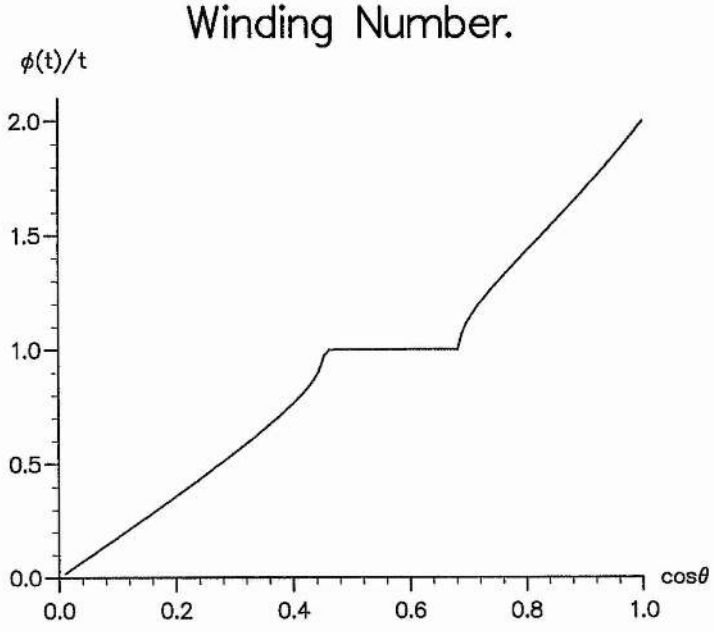

Figure 6.2: Graph showing the winding number for $\omega_1(0) = 0$ and $\omega_3(0) = 1$. Here the axes of the ellipsoid are $(a, b, c) = (3, 2, 1)$.

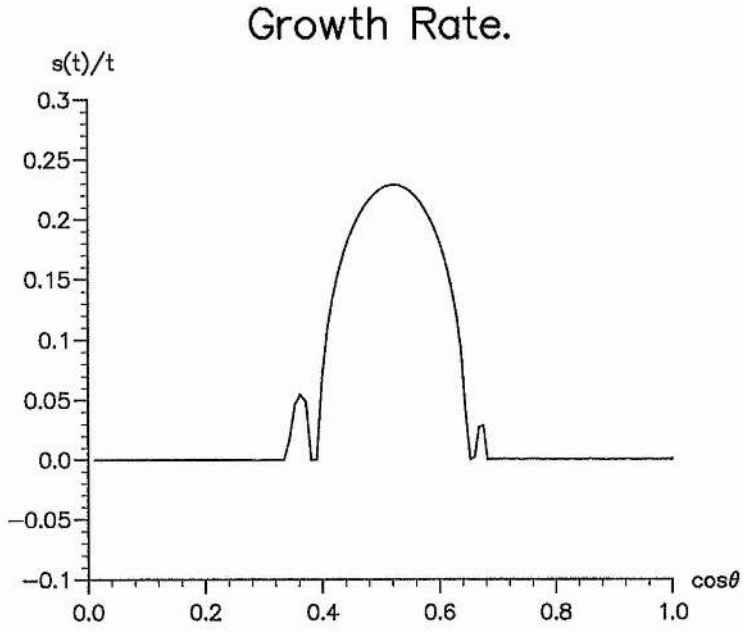

Figure 6.3: Graph showing the regions of stability for $\omega_1(0) = 0.075$ and $\omega_3(0) = 0.997183533$. The axes of the ellipsoid are $(a, b, c) = (3, 2, 1)$.

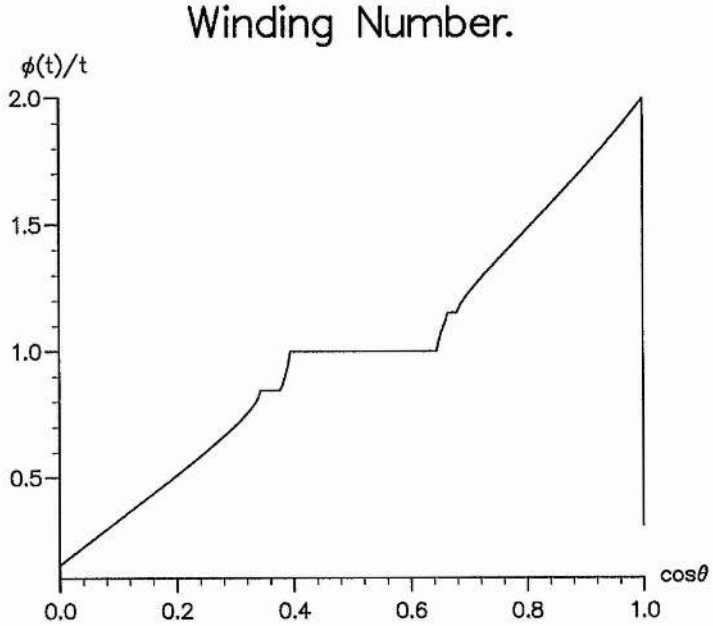

Figure 6.4: Graph showing the regions of stability for $\omega_1(0) = 0.075$ and $\omega_3(0) = 0.997183533$. The axes of the ellipsoid are $(a, b, c) = (3, 2, 1)$.

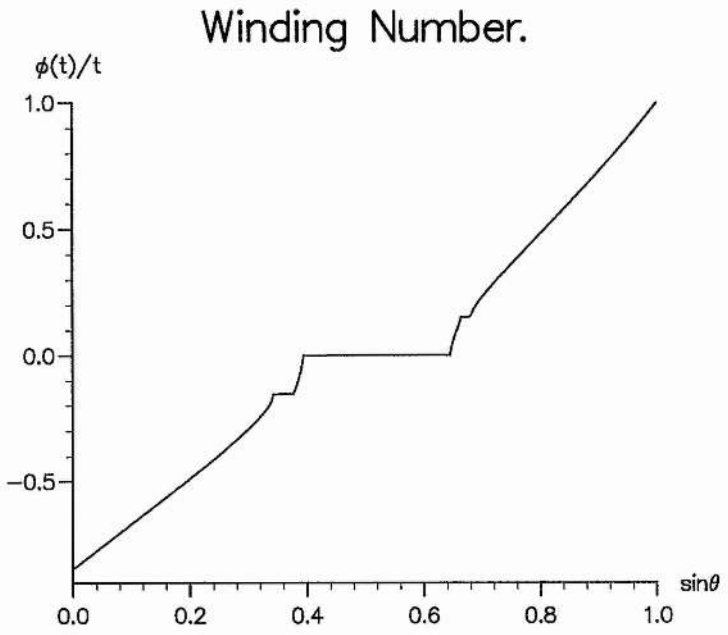

Figure 6.5: Graph showing the winding number for $\omega_1(0) = 0.997183533$ and $\omega_3(0) = 0.075$. Here the axes of the ellipsoid are $(a, b, c) = (1, 2, 3)$.

6.4 Approximation.

It has been seen in the previous section that a breakdown of numerics occurs for small θ in figure (6.4). Here we will isolate the cause of this breakdown and discuss an alternative method which prevents this.

Examining the initial conditions imposed in the last section we have $a > b > c$. This gives equations (6.2), (6.3) and (6.4) as

$$\dot{\omega}_1 = -\mid k_1 \mid \omega_2\omega_3 \tag{6.38}$$

$$\dot{\omega}_2 = \mid k_2 \mid \omega_3\omega_1 \tag{6.39}$$

$$\dot{\omega}_3 = -\mid k_3 \mid \omega_1\omega_2 \tag{6.40}$$

where

$$| k_1 | = \left| \frac{c^2 - b^2}{c^2 + b^2} \right|, \quad | k_2 | = \left| \frac{a^2 - c^2}{a^2 + c^2} \right|, \quad | k_3 | = \left| \frac{b^2 - a^2}{b^2 + a^2} \right|.$$

An approximate solution is now sought to these equations when the ω_i's satisfy the condition

$$| \omega_3 | \gg | \omega_2 |, | \omega_1 | . \tag{6.41}$$

Here $\omega_3 \sim O(1)$ and $\omega_{1,2} \sim O(\varepsilon)$, where ε is a small parameter. Substituting these into (6.38), (6.39) and (6.40) and linearizing the resultant equations, it is easily seen from (6.40) that

$$\begin{aligned} \dot{\omega}_3 &\approx 0, \\ \omega_3 &\approx \text{constant} = \omega_{30}. \end{aligned}$$

Differentiation of equation (6.38) gives

$$\ddot{\omega}_1 = - | k_1 | \omega_{30} \dot{\omega}_2, \tag{6.42}$$

and substitution of (6.39) into (6.42) then yields

$$\ddot{\omega}_1 + | k_1 || k_2 | \omega_{30}^2 \omega_1 = 0. \tag{6.43}$$

Applying the initial values for this system

$$\omega_1(0) = \omega_{10}, \qquad \dot{\omega}_1(0) = 0,$$

equation (6.43) then solves to give

$$\omega_1 = \omega_{10} \cos \sqrt{| k_1 || k_2 |} \omega_{30} t.$$

Similarly for ω_2 we have

$$\ddot{\omega}_2 = \mid k_2 \mid \omega_{30}\dot{\omega}_1,$$

and substitution of (6.38) into this equation gives

$$\ddot{\omega}_2 + \mid k_1 \mid\mid k_2 \mid \omega_{30}^2\omega_2 = 0.$$

The initial values for ω_2 are

$$\omega_2(0) = 0, \qquad \dot{\omega}_2(0) = \mid k_2 \mid \omega_{30}\omega_{10},$$

and using these the solution for ω_2 is found to be

$$\omega_2 = \sqrt{\frac{\mid k_2 \mid}{\mid k_1 \mid}}\omega_{10} \sin \sqrt{\mid k_1 \mid\mid k_2 \mid}\omega_{30}t.$$

A similar treatment is now applied to the wavenumber advection equations (6.6), (6.7) and (6.8). For small θ we have the condition

$$\mid \alpha_3 \mid \gg \mid \alpha_2 \mid, \mid \alpha_1 \mid, \tag{6.44}$$

where $\alpha_3 \sim O(1)$ and $\alpha_{1,2} \sim O(\varepsilon)$. Substitution and linearization immediately yields the result

$$\dot{\alpha}_3 \approx 0$$

$$\alpha_3 \approx \text{constant} = \alpha_{30},$$

from equation (6.8).

The linearized forms of equations (6.6) and (6.7) are found to be

$$\dot{\alpha}_1 = \frac{\omega_{30}b}{a}\alpha_2 - \frac{c}{a}\sqrt{\frac{\mid k_2 \mid}{\mid k_1 \mid}}\omega_{10}\alpha_{30} \sin \tilde{\omega}t$$

$$\dot{\alpha}_2 = -\frac{\omega_{30}a}{b}\alpha_1 + \frac{c}{b}\omega_{10}\alpha_{30}\cos\tilde{\omega}t,$$

where $\tilde{\omega} = \sqrt{\mid k_1 \mid\mid k_2 \mid}\omega_{30}$, and from these equations we obtain the second derivatives

$$\ddot{\alpha}_1 = \frac{\omega_{30}b}{a}\dot{\alpha}_2 - \frac{c}{a}\sqrt{\frac{\mid k_2 \mid}{\mid k_1 \mid}}\omega_{10}\alpha_{30}\tilde{\omega}\cos\tilde{\omega}t \tag{6.45}$$

$$\ddot{\alpha}_2 = -\frac{\omega_{30}a}{b}\dot{\alpha}_1 - \frac{c}{b}\omega_{10}\alpha_{30}\tilde{\omega}\sin\tilde{\omega}t. \tag{6.46}$$

Equation (6.45) can now be expressed as

$$\ddot{\alpha}_1 + \omega_{30}^2\alpha_1 = \frac{c}{a}\omega_{10}\omega_{30}\alpha_{30}(1- \mid k_2 \mid)\cos\tilde{\omega}t$$

and this leads to a solution of the form

$$\alpha_1 = E\sin\omega_{30}t + F\cos\omega_{30}t + \frac{c\alpha_{30}\omega_{10}(1- \mid k_2 \mid)}{a\omega_{30}(1- \mid k_1 \mid\mid k_2 \mid)}\cos\tilde{\omega}t.$$

Using the initial data

$$\alpha_1(0) = \alpha_{10}, \qquad \dot{\alpha}_1(0) = 0,$$

then the solution for α_1 is found to be

$$\alpha_1 = \left(\alpha_{10} + \frac{c\alpha_{30}\omega_{10}(\mid k_2 \mid -1)}{a\omega_{30}(1- \mid k_1 \mid\mid k_2 \mid)}\right)\cos\omega_{30}t + \frac{c\alpha_{30}\omega_{10}(1- \mid k_2 \mid)}{a\omega_{30}(1- \mid k_1 \mid\mid k_2 \mid)}\cos\tilde{\omega}t. \tag{6.47}$$

Examining finally equation (6.46), and expressing in the form

$$\ddot{\alpha}_2 + \omega_{30}^2\alpha_2 = \frac{c}{b}\omega_{10}\omega_{30}\alpha_{30}\sqrt{\mid k_2 \mid}\sin\tilde{\omega}t\left(\frac{1}{\sqrt{\mid k_1 \mid}} - \sqrt{\mid k_1 \mid}\right),$$

it is seen that this equation has a general solution

$$\alpha_2 = G\sin\omega_{30}t + H\cos\omega_{30}t + \frac{c\omega_{10}\alpha_{30}\sqrt{\mid k_2 \mid}}{b\omega_{30}(1-\mid k_1 \mid\mid k_2 \mid)}\left(\frac{1}{\sqrt{\mid k_1 \mid}} - \sqrt{\mid k_1 \mid}\right)\sin\tilde{\omega}t.$$

Using the initial data for α_2,

$$\alpha_2(0) = 0, \qquad \dot{\alpha}_2(0) = -\frac{a\omega_{30}\alpha_{10}}{b} + \frac{c\omega_{10}\alpha_{30}}{b},$$

then the solution for α_2 is found to be

$$\alpha_2 = G\sin\omega_{30}t + \frac{c\omega_{10}\alpha_{30}\sqrt{\mid k_2 \mid}}{b\omega_{30}(1-\mid k_1 \mid\mid k_2 \mid)}\left(\frac{1}{\sqrt{\mid k_1 \mid}} - \sqrt{\mid k_1 \mid}\right)\sin\tilde{\omega}t, \qquad (6.48)$$

where

$$G = \frac{1}{b\omega_{30}}\left(-\omega_{30}\alpha_{10}a - \frac{c\omega_{10}\alpha_{30}}{(1-\mid k_1 \mid\mid k_2 \mid)}(\mid k_2 \mid -1)\right).$$

The accuracy of our approximate solutions, (6.47) and (6.48), is now briefly examined. Taking initial data satisfying the conditions (6.41) and (6.44), amplitudes are plotted comparing the exact and approximate solutions for α_1 and α_2 over a time $t = 100$. The approximate doubly periodic solutions for α_1 and α_2 are shown in figures (6.6) and (6.8) respectively. It is clear from the exact solutions, figures (6.7) and (6.9), that (6.47) and (6.48) represent a good approximation for α_1 and α_2 under the assumptions used. When ω_1 is not small, figures (6.10) and (6.11), the conditions of our approximation are violated and equations (6.47) and (6.48) no longer hold. This is clearly shown in the figures.

Next we examine the possibility of α_1 and α_2 going through, or very close to zero at the same instant [which would cause numerical problems in (6.20)]. This is clearly trivial when $\alpha_{10} = 0$, but can it exist when $\alpha_{10} \neq 0$?

If we let $\alpha_1 = 0$ at some time $t > 0$, then we obtain the relation

$$\frac{\cos\tilde{\omega}t}{\cos\omega_{30}t} = \alpha_{10}\frac{a\omega_{30}(1-\mid k_1 \mid\mid k_2 \mid)}{c\alpha_{30}\omega_{10}(1-\mid k_2 \mid)} + 1. \tag{6.49}$$

Letting $\tilde{t} = \omega_{30}t$ we then have

$$\frac{\cos A\tilde{t}}{\cos\tilde{t}} = K_1, \tag{6.50}$$

where A, when $(a, b, c) = (3, 2, 1)$ is the irrational number $\sqrt{\mid k_1 \mid\mid k_2 \mid}$ and K_1 represents the r.h.s. of (6.49).

Next we suppose that $\alpha_2 = 0$ at some future time, yielding a second relation

$$\frac{\sin\tilde{\omega}t}{\sin\omega_{30}t} = \sqrt{\mid k_1 \mid}\left(\frac{c\alpha_{30}\omega_{10}(1-\mid k_2 \mid) - a\alpha_{10}\omega_{30}(1-\mid k_1 \mid\mid k_2 \mid)}{c\omega_{10}\alpha_{30}\sqrt{\mid k_2 \mid}(\mid k_1 \mid -1)}\right).$$

Similarly this can be written

$$\frac{\sin A\tilde{t}}{\sin\tilde{t}} = K_2, \tag{6.51}$$

where K_2 is a second constant.

Combination of equations (6.50) and (6.51) yields the two expressions

$$\sin\tilde{t} = \pm\sqrt{\frac{(1-K_1^2)}{(K_2^2-K_1^2)}} \tag{6.52}$$

and

$$\sin A\tilde{t} = \pm K_2\sqrt{\frac{(1-K_1^2)}{(K_2^2-K_1^2)}}.$$

If the r.h.s. of these equations are less then 1, then they can clearly be satisfied independently, but we require them to be satisfied at the same time. Assuming that (6.52) is true for some $\tilde{t} = t^*$, then it is also true for

$$\tilde{t}_n = t^* + 2n\pi \qquad \text{or} \qquad \tilde{t}_n = t^* - (2n+1)\pi.$$

This means we also require

$$\sin A(t^* + 2n\pi) = \pm K_2 \sqrt{\frac{(1 - K_1^2)}{(K_2^2 - K_1^2)}} \tag{6.53}$$

or

$$\sin A(t^* - (2n + 1)\pi) = \pm K_2 \sqrt{\frac{(1 - K_1)^2}{(K_2^2 - K_1^2)}}. \tag{6.54}$$

Clearly, because A is irrational certain values of n will satisfy the conditions (6.53) or (6.54) to high accuracy, so it is possible that α_1 and α_2 will go arbitrarily close to zero at the same time. If this happens a breakdown in the calculation of the relations (6.20) will occur, as was found to happen.

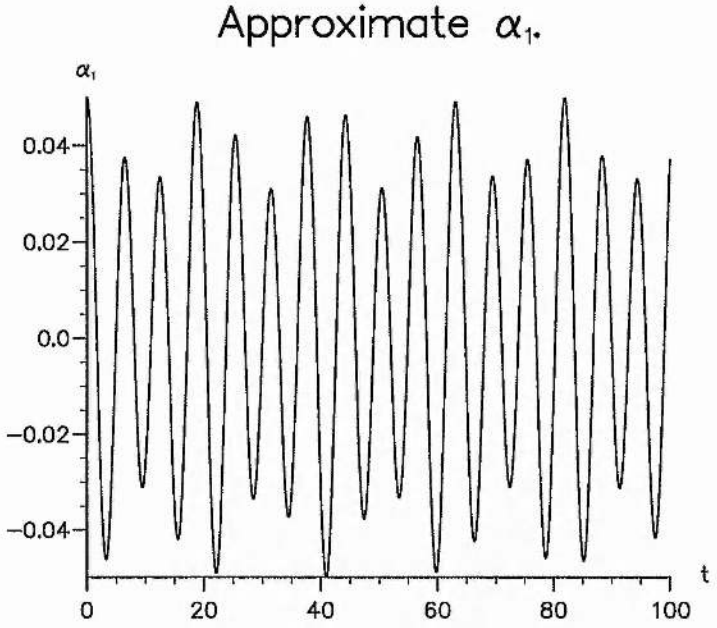

Figure 6.6: Graph showing the amplitude plot for α_1 using an approximation and the initial data $\omega_1(0) = 0.075$, $\omega_3(0) = 0.997183533$ and $\theta = 0.05$.

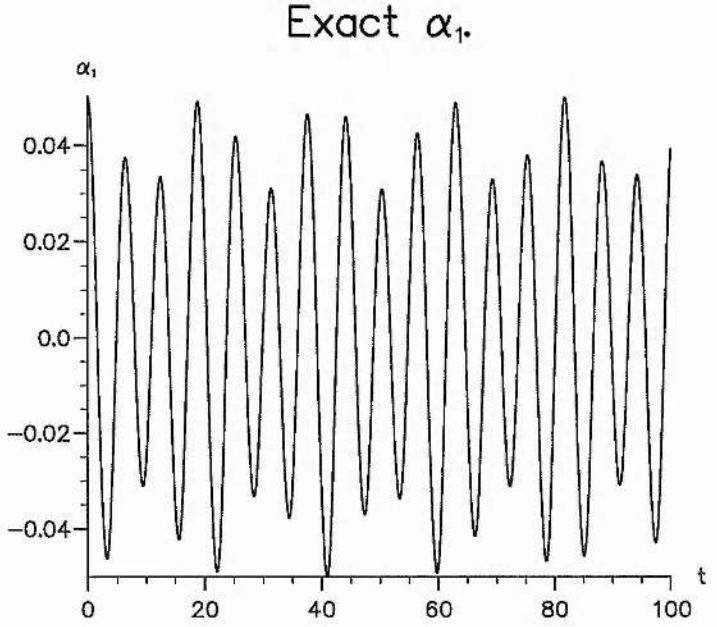

Figure 6.7: Graph showing the exact amplitude plot α_1 for the initial data $\omega_1(0) = 0.075$, $\omega_3(0) = 0.997183533$ and $\theta = 0.05$.

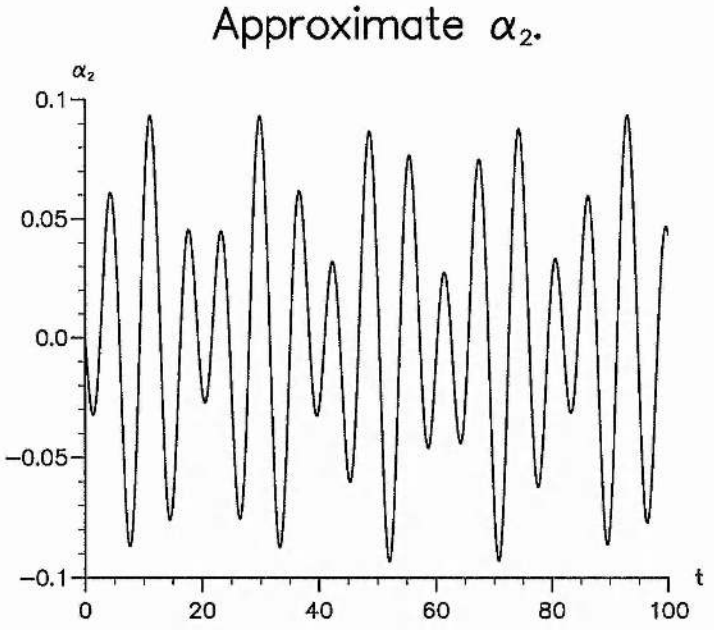

Figure 6.8: Graph showing the amplitude plot for α_2 using an approximation and the initial data $\omega_1(0) = 0.075$, $\omega_3(0) = 0.997183533$ and $\theta = 0.05$.

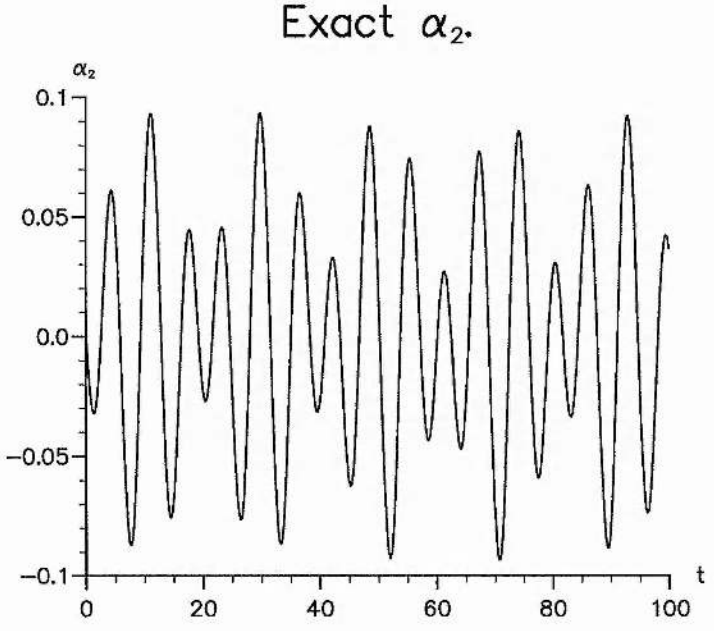

Figure 6.9: Graph showing the exact amplitude plot α_2 for the initial data $\omega_1(0) = 0.075$, $\omega_3(0) = 0.997183533$ and $\theta = 0.05$.

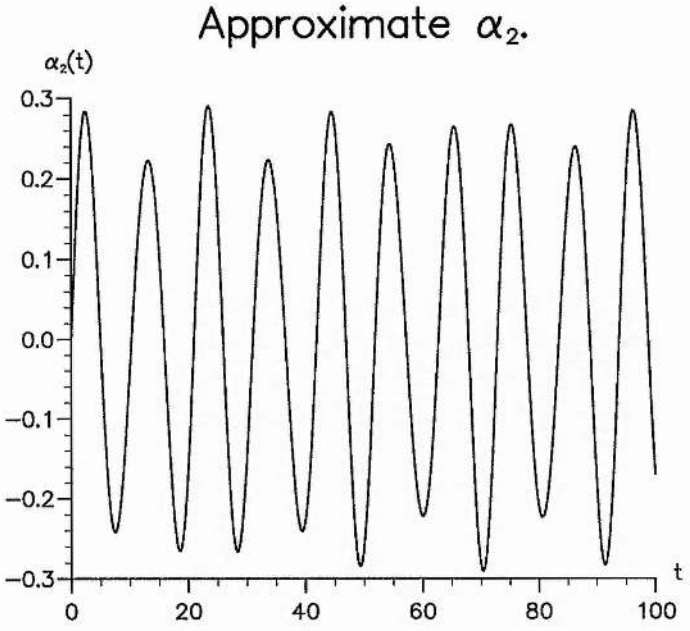

Figure 6.10: Graph showing the amplitude plot for α_2 using an approximation and the initial data $\omega_1(0) = 0.50$, $\omega_3(0) = 0.866025404$ and $\theta = 0.05$.

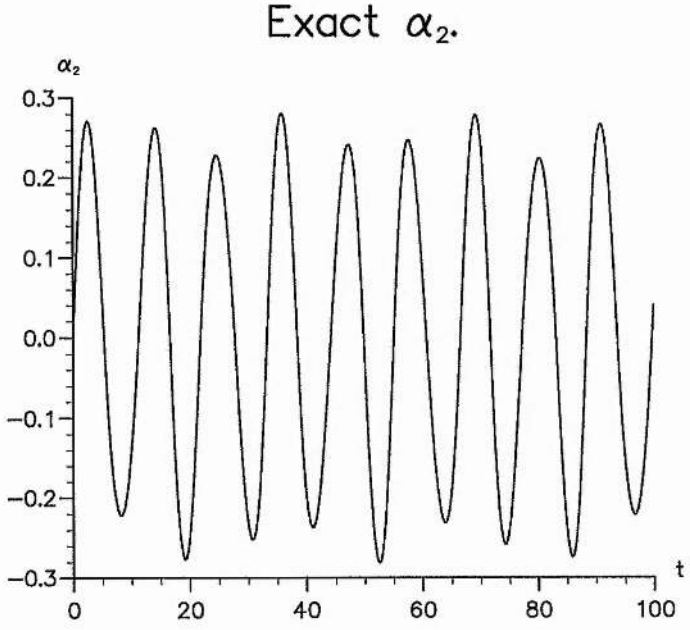

Figure 6.11: Graph showing the exact amplitude plot α_2 for the initial data $\omega_1(0) = 0.50$, $\omega_3(0) = 0.866025404$ and $\theta = 0.05$.

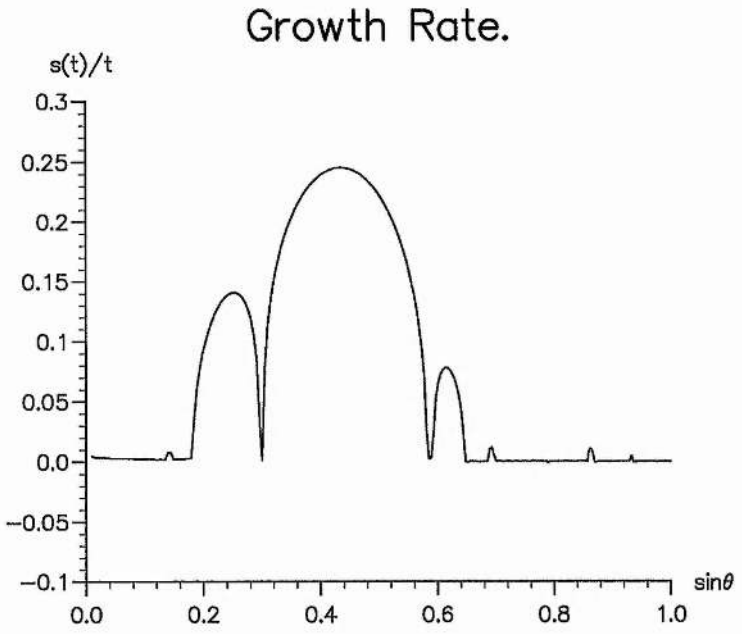

Figure 6.12: Graph showing the regions of stability for $\omega_1(0) = 0.979795897$ and $\omega_3(0) = 0.20$. Here the axes of the ellipsoid are $(a, b, c) = (1, 2, 3)$.

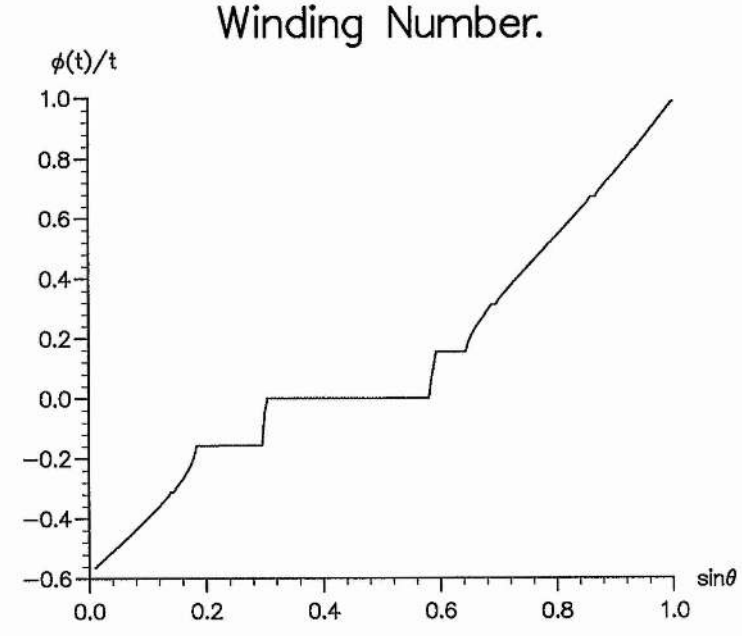

Figure 6.13: Graph showing the winding number for $\omega_1(0) = 0.979795897$ and $\omega_3(0) = 0.20$. Here the axes of the ellipsoid are $(a, b, c) = (1, 2, 3)$.

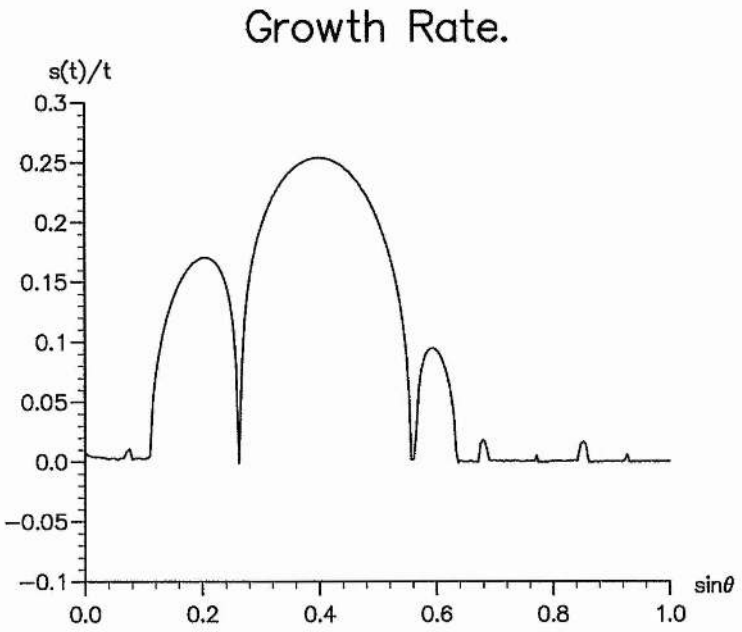

Figure 6.14: Graph showing the regions of stability for $\omega_1(0) = 0.968245836$ and $\omega_3(0) = 0.25$. Here the axes of the ellipsoid are $(a, b, c) = (1, 2, 3)$.

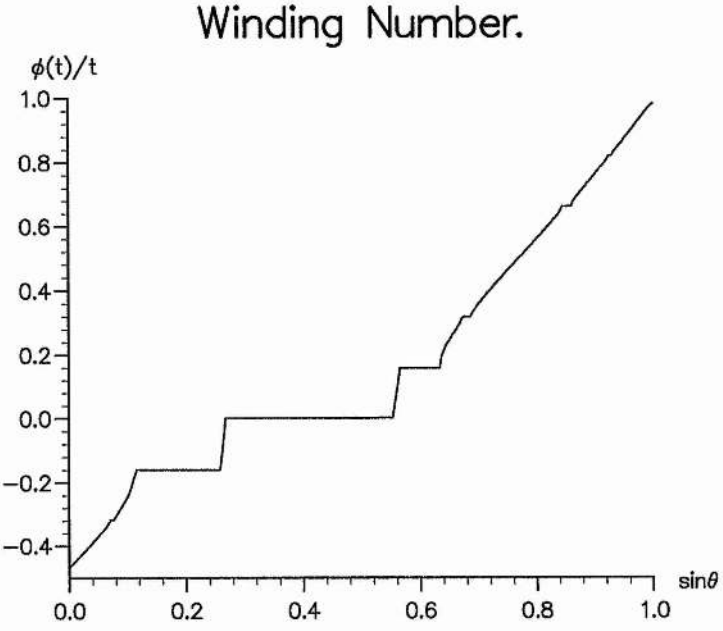

Figure 6.15: Graph showing the winding number for $\omega_1(0) = 0.968245836$ and $\omega_3(0) = 0.25$. Here the axes of the ellipsoid are $(a, b, c) = (1, 2, 3)$.

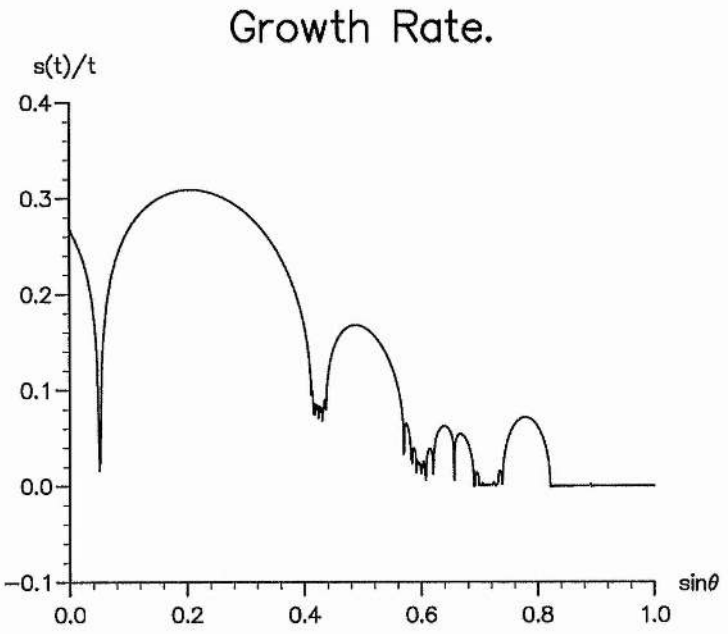

Figure 6.16: Graph showing the regions of stability for $\omega_1(0) = 0.866025404$ and $\omega_3(0) = 0.50$. Here the axes of the ellipsoid are $(a, b, c) = (1, 2, 3)$.

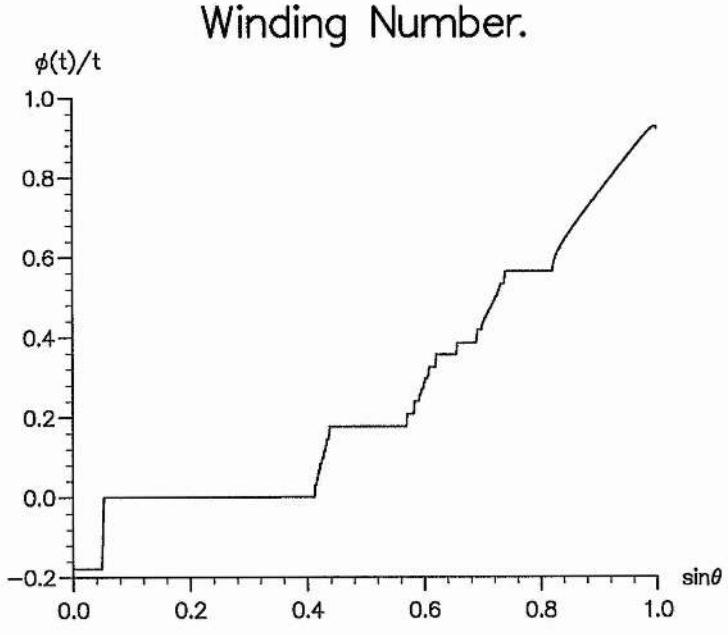

Figure 6.17: Graph showing the winding number for $\omega_1(0) = 0.866025404$ and $\omega_3(0) = 0.50$. Here the axes of the ellipsoid are $(a, b, c) = (1, 2, 3)$.

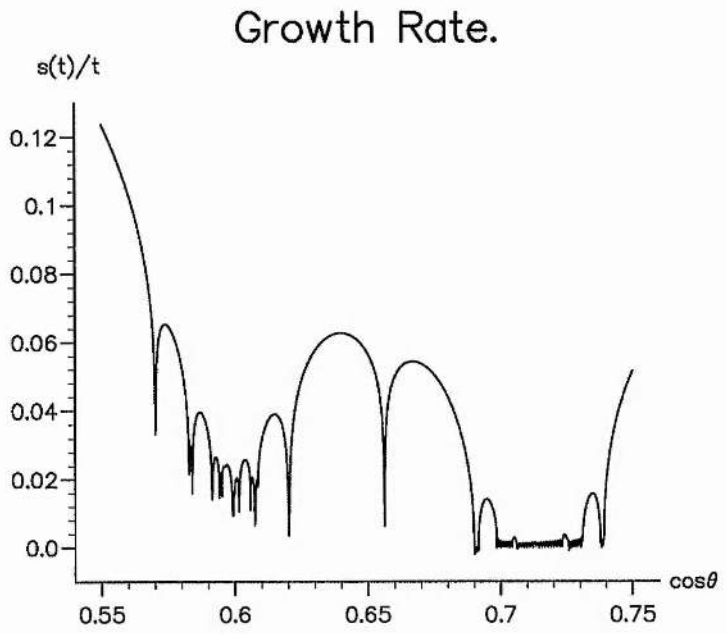

Figure 6.18: Graph showing a interval of the stability regions for $\omega_1(0) = 0.866025404$ and $\omega_3(0) = 0.50$ and the axes being $(a, b, c) = (1, 2, 3)$.

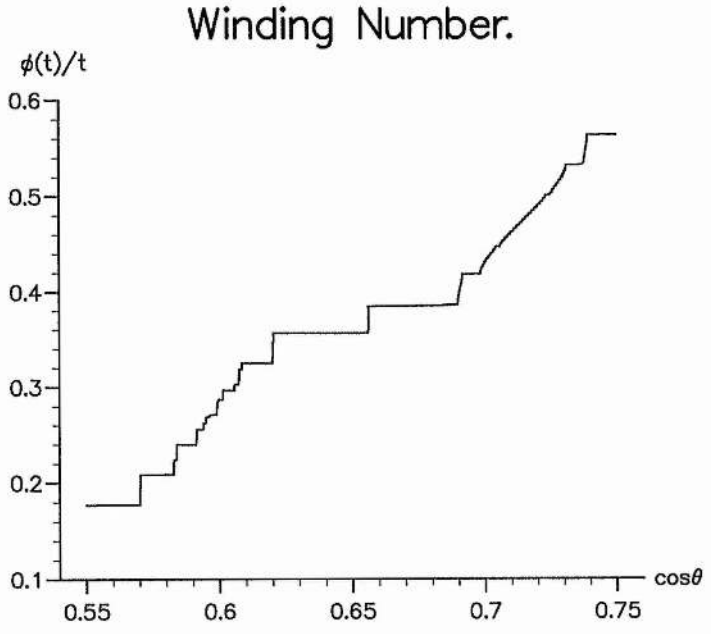

Figure 6.19: Graph showing an interval of the winding number for $\omega_1(0) = 0.866025404$ and $\omega_3(0) = 0.50$ and the axes being $(a, b, c) = (1, 2, 3)$.

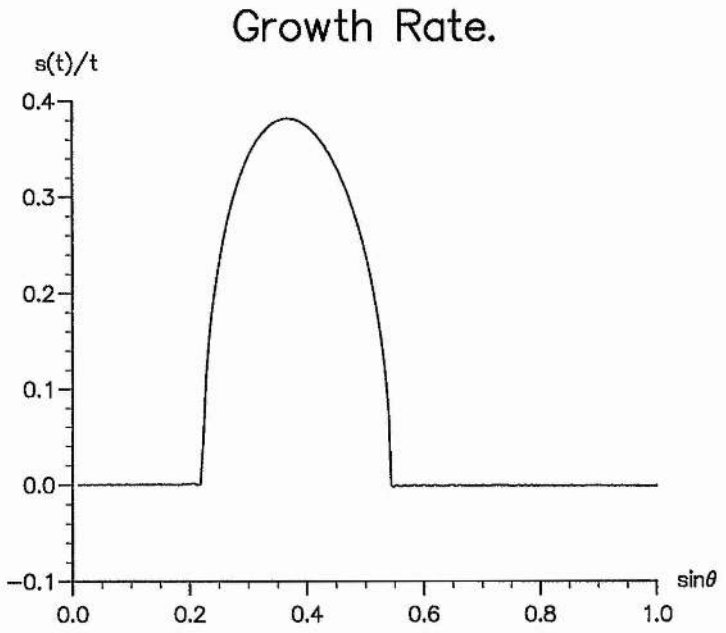

Figure 6.20: Graph showing the regions of stability for $\omega_1(0) = 0$ and $\omega_3(0) = 1.0$. Here the axes of the ellipsoid are $(a, b, c) = (1, 2, 3)$.

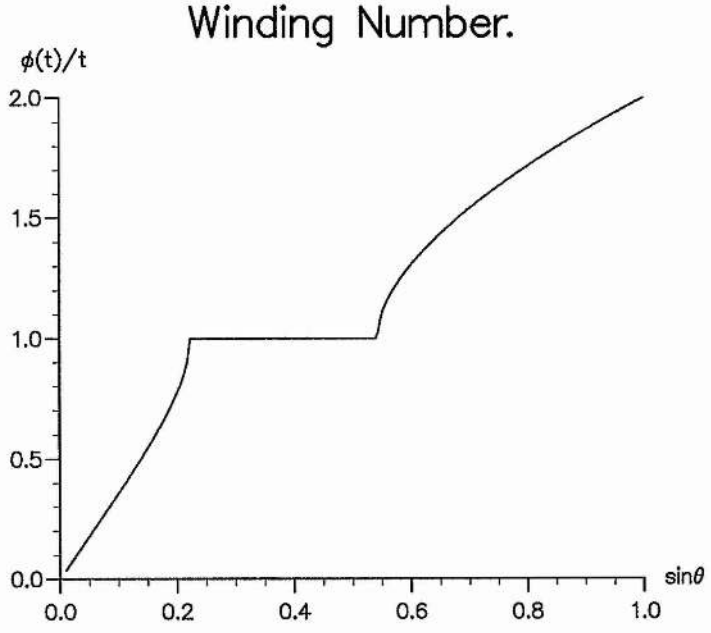

Figure 6.21: Graph showing the winding number for $\omega_1(0) = 0$ and $\omega_3(0) = 1.0$. Here the axes of the ellipsoid are $(a, b, c) = (1, 2, 3)$.

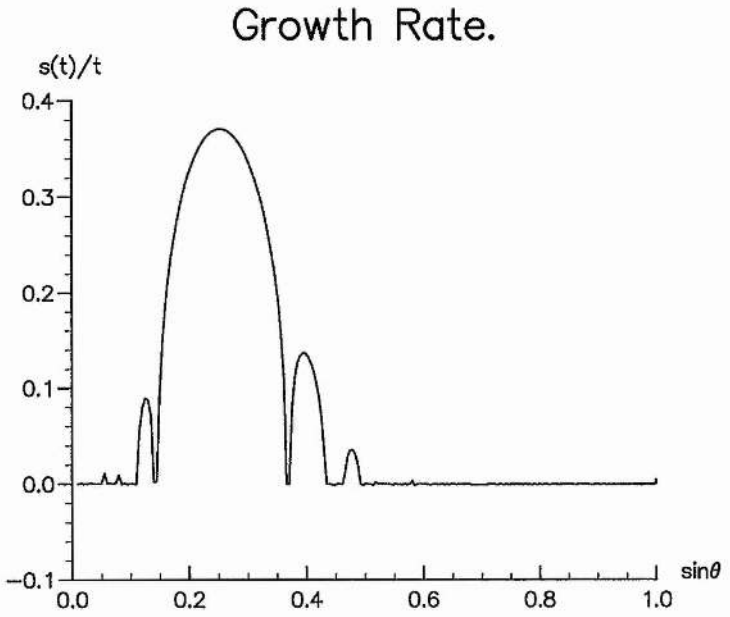

Figure 6.22: Graph showing the regions of stability for $\omega_1(0) = 0.075$ and $\omega_3(0) = 0.997183533$. Here the axes of the ellipsoid are $(a, b, c) = (1, 2, 3)$.

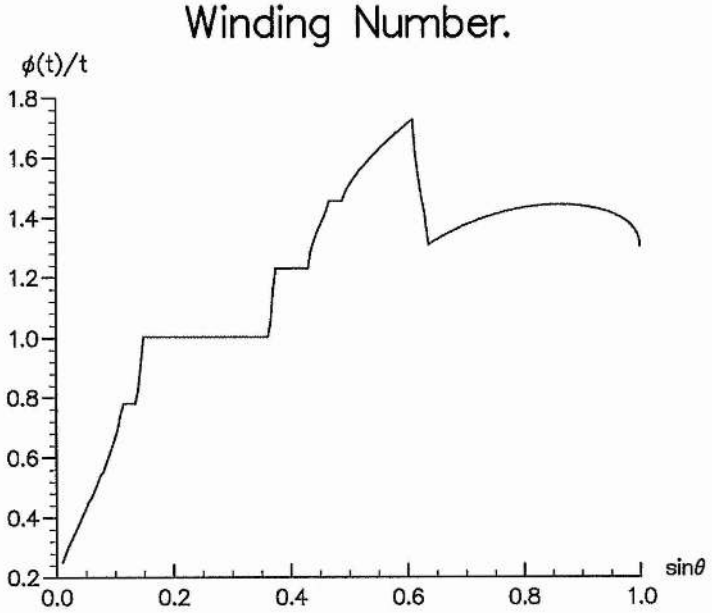

Figure 6.23: Graph showing the winding number for $\omega_1(0) = 0.075$ and $\omega_3(0) = 0.997183533$. Here the axes of the ellipsoid are $(a, b, c) = (1, 2, 3)$.

6.5 Discussion.

In this chapter we have examined the stability of a class of three-dimensional time-periodic flows with fixed ellipsoidal stream surfaces. Relating our system to a Schrödinger equation with quasi-periodic potential, we adapt a recently developed computational method and determine when the system becomes unstable to plane-wave disturbances. If rotation of the fluid occurs around only one of the coordinate axes, the flow corresponds to the purely elliptical case and may be examined using Floquet theory. Allowing rotation around a further coordinate axis introduces a time-periodicity into the basic flow. This acts to reinforce the elliptical instability through the creation of new parametric instability bands and the system is then highly unstable.

Clearly most swirling flows of this sort are expected to be unstable, unless the spatial dimensions are sufficiently small that viscous damping is considerable. Such flows as are inviscidly stable will either have circular streamlines or - as for elliptical flows in a rotating frame - will have vorticity close to zero in an inertial frame. Virtually any externally-driven large-scale vortical flow within an asymmetric container will be highly unstable to broad-band disturbances of the sort exemplified here. This suggests that the natural state of such flows will be turbulent.

Chapter 7

More time-dependent flows.

7.1 Time-periodic flows with oscillatory strain rates.

Other time-dependent flows that can be examined using the method employed in the previous chapter, are those flows which have oscillatory principal rates of strain, $(a, b, -a-b)$, directed constantly along the coordinate axes. This class of flows, discussed by Craik & Allen (1992), produces a matrix $\boldsymbol{S}$ of the form

$$\boldsymbol{S} = \{\sigma_{ij}\} = \begin{pmatrix} a(t) & -\omega_3(t) & \omega_2(t) \\ \omega_3(t) & b(t) & -\omega_1(t) \\ -\omega_2(t) & \omega_1(t) & -a(t)-b(t) \end{pmatrix}, \tag{7.1}$$

where

$$a(t) = a_0 \cos \Omega t, \qquad b(t) = b_0 \cos \Omega t, \qquad \Omega \quad \text{constant}.$$

From Craik & Allen equation (2.5), the matrix (7.1) yields the components

$$\omega_1 = \omega_{10} \exp\left(\frac{a_0}{\Omega} \sin \Omega t\right), \tag{7.2}$$

$$\omega_2 = \omega_{20} \exp\left(\frac{b_0}{\Omega} \sin \Omega t\right), \tag{7.3}$$

$$\omega_3 = \omega_{30} \exp\left(-\frac{(a_0 + b_0)}{\Omega} \sin \Omega t\right), \tag{7.4}$$

where the ω_{i0}'s are constants. Next, the wavenumber advection equation,

$$\dot{\boldsymbol{\alpha}} = -\boldsymbol{S}^T \boldsymbol{\alpha},$$

together with (7.1), gives the further three equations

$$\dot{\alpha}_1 = -a_0 \alpha_1 \cos \Omega t - \omega_3 \alpha_2 + \omega_2 \alpha_3, \tag{7.5}$$

$$\dot{\alpha}_2 = -b_0 \alpha_2 \cos \Omega t + \omega_3 \alpha_1 - \omega_1 \alpha_3, \tag{7.6}$$

$$\dot{\alpha}_3 = (a_0 + b_0) \alpha_3 \cos \Omega t - \omega_2 \alpha_1 + \omega_1 \alpha_2. \tag{7.7}$$

The inviscid velocity components, again obtained from (5.9)-(5.11), can be written as

$$\begin{aligned}
\dot{u}_1 &= -a u_1 + \omega_3 u_2 - \omega_2 u_3 + \frac{2\alpha_1 u_1}{(\boldsymbol{\alpha} \cdot \boldsymbol{\alpha})}(\alpha_1 a + \alpha_2 \omega_3 - \alpha_3 \omega_2) \\
&+ \frac{2\alpha_1 u_2}{(\boldsymbol{\alpha} \cdot \boldsymbol{\alpha})}(-\alpha_1 \omega_3 + \alpha_2 b + \alpha_3 \omega_1) + \frac{2\alpha_1 u_3}{(\boldsymbol{\alpha} \cdot \boldsymbol{\alpha})}(\alpha_1 \omega_2 - \alpha_2 \omega_1 - \alpha_3 (a + b)) \\
\dot{u}_2 &= -\omega_3 u_1 - b u_2 + \omega_1 u_3 + \frac{2\alpha_2 u_1}{(\boldsymbol{\alpha} \cdot \boldsymbol{\alpha})}(\alpha_1 a + \alpha_2 \omega_3 - \alpha_3 \omega_2) \\
&+ \frac{2\alpha_2 u_2}{(\boldsymbol{\alpha} \cdot \boldsymbol{\alpha})}(-\alpha_1 \omega_3 + \alpha_2 b + \alpha_3 \omega_1) + \frac{2\alpha_2 u_3}{(\boldsymbol{\alpha} \cdot \boldsymbol{\alpha})}(\alpha_1 \omega_2 - \alpha_2 \omega_1 - \alpha_3 (a + b)) \\
\dot{u}_3 &= \omega_2 u_1 - \omega_1 u_2 + (a + b) u_3 + \frac{2\alpha_3 u_1}{(\boldsymbol{\alpha} \cdot \boldsymbol{\alpha})}(\alpha_1 a + \alpha_2 \omega_3 - \alpha_3 \omega_2) \\
&+ \frac{2\alpha_3 u_2}{(\boldsymbol{\alpha} \cdot \boldsymbol{\alpha})}(-\alpha_1 \omega_3 + \alpha_2 b + \alpha_3 \omega_1) + \frac{2\alpha_3 u_3}{(\boldsymbol{\alpha} \cdot \boldsymbol{\alpha})}(\alpha_1 \omega_2 - \alpha_2 \omega_1 - \alpha_3 (a + b)).
\end{aligned}$$

The system is again reduced to two coupled equations by using the dependent variables (6.9), together with continuity equation (5.8). The inviscid velocity equations can then be written in the form

$$\begin{pmatrix} \dot{P} \\ \\ \dot{Q} \end{pmatrix} = \begin{pmatrix} r_{11} & r_{12} \\ \\ r_{21} & r_{22} \end{pmatrix} \begin{pmatrix} P \\ \\ Q \end{pmatrix}, \tag{7.8}$$

where

$$\begin{aligned}
r_{11} &= \frac{1}{(\alpha_1^2+\alpha_2^2)}\left[\alpha_1\alpha_3\omega_2 - \alpha_2\alpha_3\omega_1 - (\alpha_1^2+\alpha_2^2)(a_0+b_0)\cos\Omega t\right] \\
r_{12} &= \frac{1}{|\alpha(0)|(\alpha_1^2+\alpha_2^2)}\left[2\alpha_3\omega_3(\alpha_1^2+\alpha_2^2) + (1-\alpha_3^2)(\alpha_2\omega_2+\alpha_1\omega_1)\right] \\
r_{21} &= \frac{2\alpha_1\alpha_2\alpha_3|\alpha(0)|(b_0-a_0)\cos\Omega t}{(\alpha_1^2+\alpha_2^2)(\boldsymbol{\alpha}\cdot\boldsymbol{\alpha})} - \frac{2\alpha_3\omega_3|\alpha(0)|}{(\boldsymbol{\alpha}\cdot\boldsymbol{\alpha})} \\
&+ \frac{\alpha_1\omega_1|\alpha(0)|}{(\alpha_1^2+\alpha_2^2)}\left(\frac{2\alpha_3^2}{(\boldsymbol{\alpha}\cdot\boldsymbol{\alpha})}-1\right) + \frac{\alpha_2\omega_2|\alpha(0)|}{(\alpha_1^2+\alpha_2^2)}\left(\frac{2\alpha_3^2}{(\boldsymbol{\alpha}\cdot\boldsymbol{\alpha})}-1\right) \\
r_{22} &= \frac{\alpha_3(\alpha_1\omega_2-\alpha_2\omega_1)}{(\alpha_1^2+\alpha_2^2)} + \frac{(\alpha_1^2+\alpha_2^2-2\alpha_3^2)(a_0+b_0)\cos\Omega t}{(\boldsymbol{\alpha}\cdot\boldsymbol{\alpha})} \\
&+ \frac{\alpha_3^2(a_0-b_0)(\alpha_2^2-\alpha_1^2)}{(\alpha_1^2+\alpha_2^2)(\boldsymbol{\alpha}\cdot\boldsymbol{\alpha})}\cos\Omega t.
\end{aligned}$$

Equation (7.8) is similar to that obtained by Craik & Allen and, with the simplification $\omega_{10} = \omega_{20} = 0$, reduces to a form equivalent to their (2.12a) and (2.12b). If $a_0 = b_0$, the special case of axisymmetric flow, (7.8) can be formulated as a Hill's equation with a periodic potential. [see Craik & Allen equation (2.17)]. This being the case, the governing equations become linear and time-periodic and the stability problem may be solved by the use of Floquet theory. (Craik & Allen section 4). However, when the flow is non-axisymmetric, ($a_0 \neq b_0$), the potential becomes quasi-periodic and this method can no longer be used. In order to

examine the stability of such a system the technique highlighted in the previous chapter must again be invoked.

With use of equations (7.2)-(7.7), together with the constant Ω, the coefficients r_{ij} can now be calculated at each time interval. These, when substituted into the previously derived equations

$$\dot{\phi} = \left(\frac{r_{12}+r_{21}}{2}\right)\cos 2\phi - \left(\frac{r_{11}-r_{22}}{2}\right)\sin 2\phi + \left(\frac{r_{21}-r_{12}}{2}\right)$$

$$\dot{s} = \left(\frac{r_{12}+r_{21}}{2}\right)\sin 2\phi + \left(\frac{r_{11}-r_{22}}{2}\right)\cos 2\phi + \left(\frac{r_{11}+r_{22}}{2}\right),$$

enable us to calculate the winding number and growth rate for each initial disturbance $\boldsymbol{\alpha}(0)$.

7.2 Numerical results.

The stability of the basic flow is now examined for cases when the straining is axisymmetric and non-axisymmetric. This can be thought of as examining a rotating body of fluid which is being deformed due to the presence of sinusoidally varying external forces acting along the coordinate axes. When a small disturbance is added into the flow two things may happen. Firstly, the disturbance may grow, causing the flow to become unstable, secondly, it may remain small, dying away if viscous damping is present. The numerical investigation concentrates on calculating the growth rates for different disturbances and concluding whether or not they cause instability.

For simplicity attention is restricted to basic flows that have x_3-vorticity only, i.e. $\omega_{10} = \omega_{20} = 0$ and $\omega_{30} = 1$. This allows us to compare our results closely with those obtained by Craik & Allen, who used a similar simplification. Initially the axisymmetric flow is taken and the instability bands located. Non-axisymmetric properties are introduced and the stability of the flows to plane-wave disturbances examined. As before the limits of growth rate and winding number are calculated numerically over large times and with the conditions $|\boldsymbol{\omega}(0)| = 1$ and $|\boldsymbol{\alpha}(0)| = 1$ again being imposed.

7.2.1 The axisymmetric case.

The axisymmetric case, equivalent to that studied by Craik & Allen, is the first examined. Here we have the restriction $a_0 = b_0$, with the values $a_0 = b_0 = 0.5$ being initially chosen. Figures (7.1) and (7.2) show the calculated growth rates and winding numbers for this system. The initial data chosen is equivalent to that of $\overline{a} = 1.0$ in the Craik & Allen study, with the instability bands depicted in figures (7.1) and (7.2) corresponding to the results shown in their figure (1). Here only the four strongest instability bands can be seen, with any weaker, narrower bands unable to be found at this resolution. Two strong/broad and two weaker/narrow bands can easily be identified and the maximum growth rates tabulated by Craik & Allen for these are confirmed. [It should be noted that θ_0 in the Craik & Allen study corresponds to $(\frac{\pi}{2} - \theta)$ here]. Clearly this system is

stable to most plane-wave disturbances, but strong growth occurs for a band of disturbances introduced between $\theta = \cos^{-1} 0.8$ and $\theta = \cos^{-1} 1.0$.

In order to examine the effects of the frequency Ω on the stability of the system, Ω is now increased. Figures (7.3) and (7.4) show the effect which this has when Ω is increased to 0.75. Although the two main bands are still visible, the two weaker bands have now been suppressed. This indicates that increasing the forcing frequency Ω results in a stabilizing effect. Further increases in Ω were found to suppress the growth rates of these bands still further and for values of $\Omega > 4$, the bands disappeared altogether.

Next the values of $a_0 = b_0$ are lowered in order to observe the effect that the ratio $\frac{a_0}{\Omega}$ has on the system. By lowering a_0 to 0.1, we obtain the results shown in figures (7.5) and (7.6). Here the value of Ω is still taken to be 0.75, but because of the decrease in the ratios $\frac{a_0}{\Omega}$, the growth rates and widths of the unstable regions are found to be much smaller. This indicates that decreasing these ratios has a stabilizing influence on the system as one would expect. This is consistent with the observations of Craik & Allen: they found that for small $\frac{a_0}{\Omega}$, the system may be predicted to good approximation by an equation of Mathieu's type. For such equations, regions of parametric instability then emanate from

$$\left(\frac{2\omega_{30}\sin\theta}{\Omega}\right)^2 = \frac{1}{4}n^2 \qquad (n = 1, 2, 3, 4..), \tag{7.9}$$

(c.f. Craik & Allen). Clearly when $\Omega = 0.75$ and $\omega_{10} = 1$ we should expect to

obtain five regions of instability as given by (7.9), but only two bands can be seen in figures (7.5) and (7.6). This again can be explained by the findings of Craik & Allen, since they discovered that for small $\frac{a_0}{\Omega}$, the growth rates and bandwidths of the unstable regions are of $O\left\{\left(\frac{a_0}{\Omega}\right)^n\right\}$ and thus higher number bands can not be seen by our graphical representation.

To verify the equation (7.9) further, Ω is now raised to 2.5, with a_0 remaining at 0.1. As predicted by (7.9), the system now has only one instability band emanating from the $\cos\theta$-axis at $\cos\theta = 0.78$, and this is shown clearly in figures (7.7) and (7.8). Once $\frac{\Omega}{\omega_{30}} \geq 4$, then no instability bands exist and the system becomes stable.

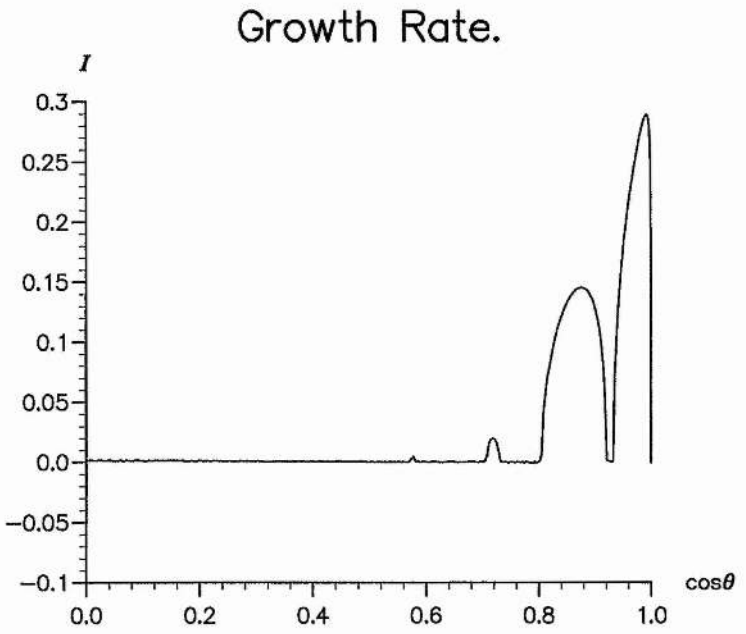

Figure 7.1: Graph showing the regions of stability for $a_0 = 0.5$ and $b_0 = 0.5$. Here $\Omega = 0.5$, $\omega_1(0) = 0$ and $\omega_3(0) = 1$.

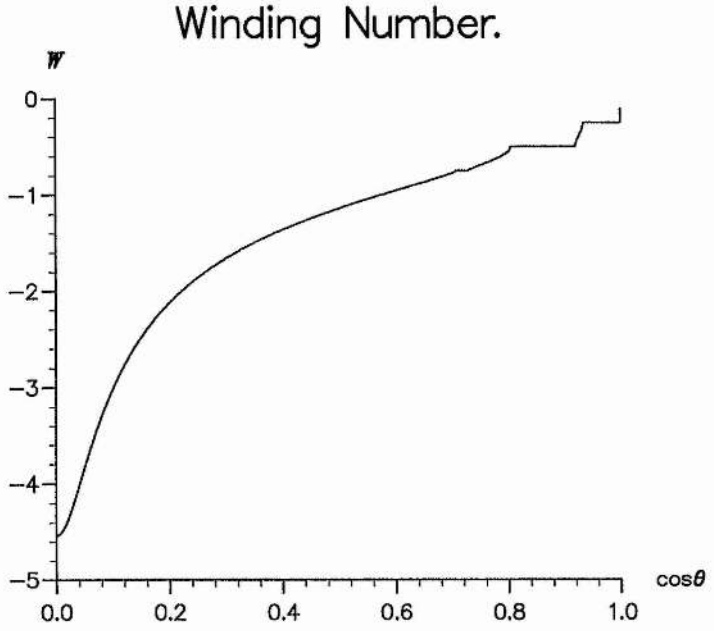

Figure 7.2: Graph showing the winding number when $a_0 = 0.5$ and $b_0 = 0.5$. Here $\Omega = 0.5$, $\omega_1(0) = 0$ and $\omega_3(0) = 1$.

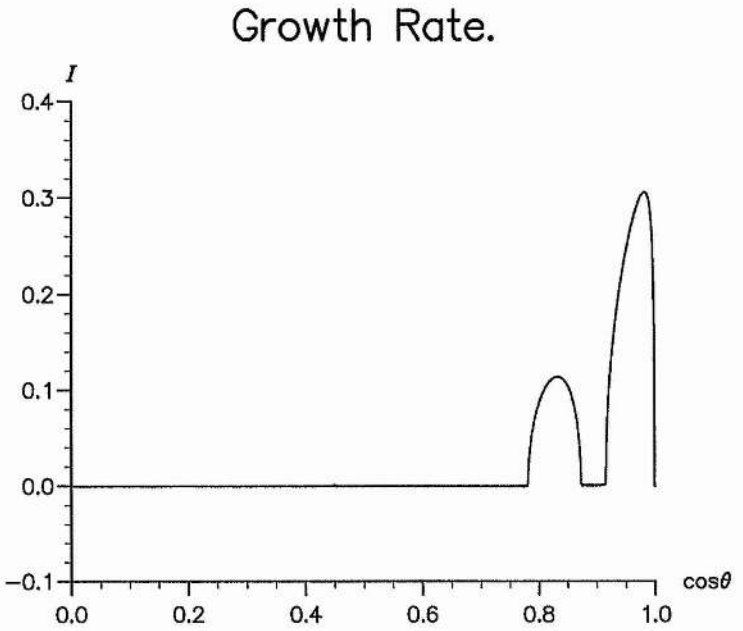

Figure 7.3: Graph showing the regions of stability for $a_0 = 0.5$ and $b_0 = 0.5$. Here $\Omega = 0.75$, $\omega_1(0) = 0$ and $\omega_3(0) = 1$.

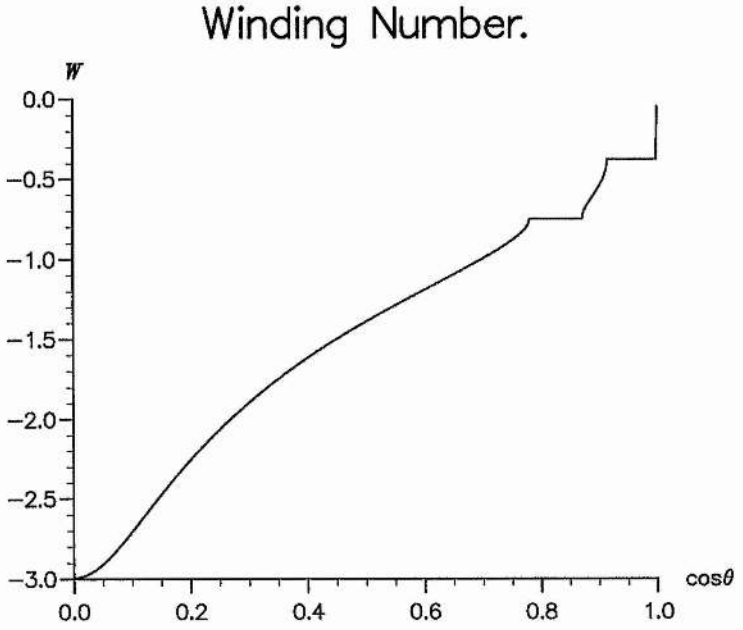

Figure 7.4: Graph showing the winding number when $a_0 = 0.5$ and $b_0 = 0.5$. Here $\Omega = 0.75$, $\omega_1(0) = 0$ and $\omega_3(0) = 1$.

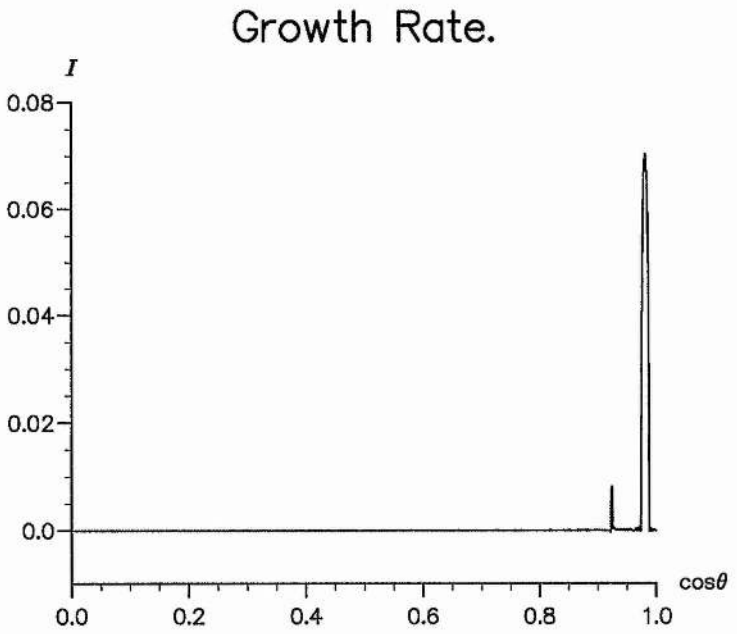

Figure 7.5: Graph showing the regions of stability for $a_0 = 0.1$ and $b_0 = 0.1$. Here $\Omega = 0.75$, $\omega_1(0) = 0$ and $\omega_3(0) = 1$.

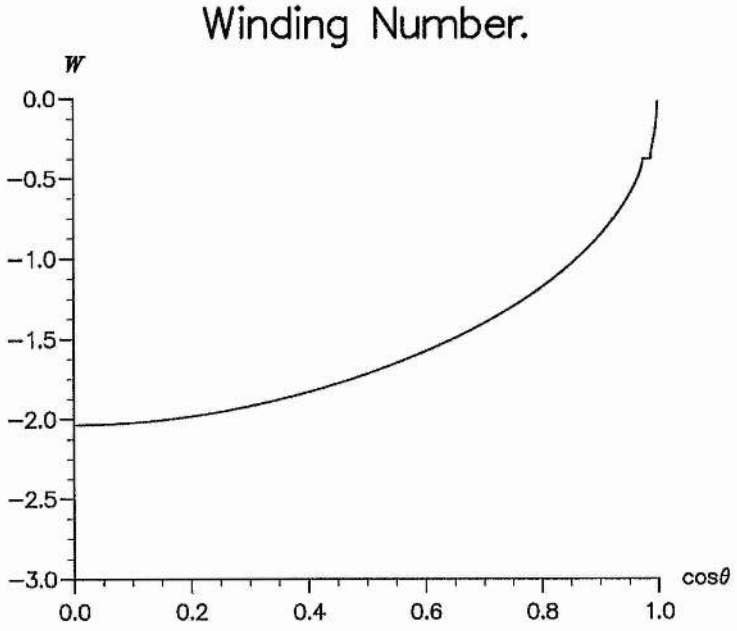

Figure 7.6: Graph showing the winding number when $a_0 = 0.1$ and $b_0 = 0.1$. Here $\Omega = 0.75$, $\omega_1(0) = 0$ and $\omega_3(0) = 1$.

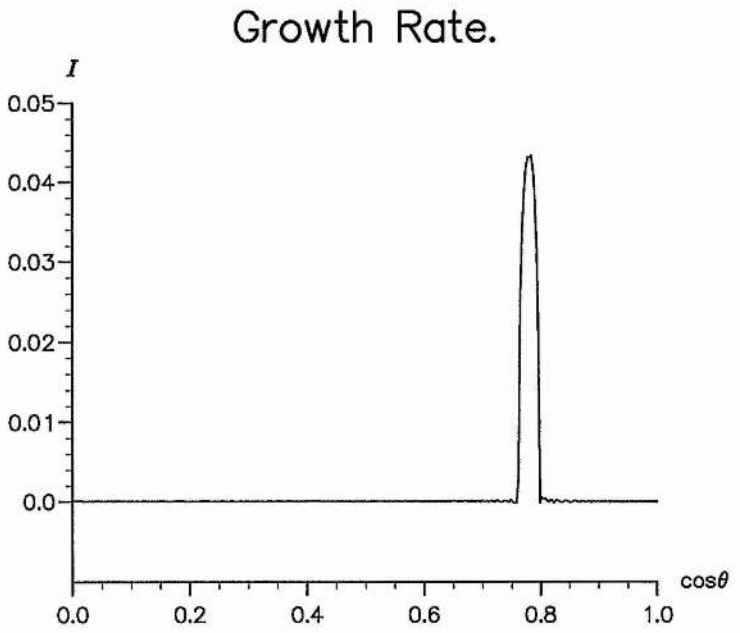

Figure 7.7: Graph showing the regions of stability for $a_0 = 0.1$ and $b_0 = 0.1$. Here $\Omega = 2.5$, $\omega_1(0) = 0$ and $\omega_3(0) = 1$.

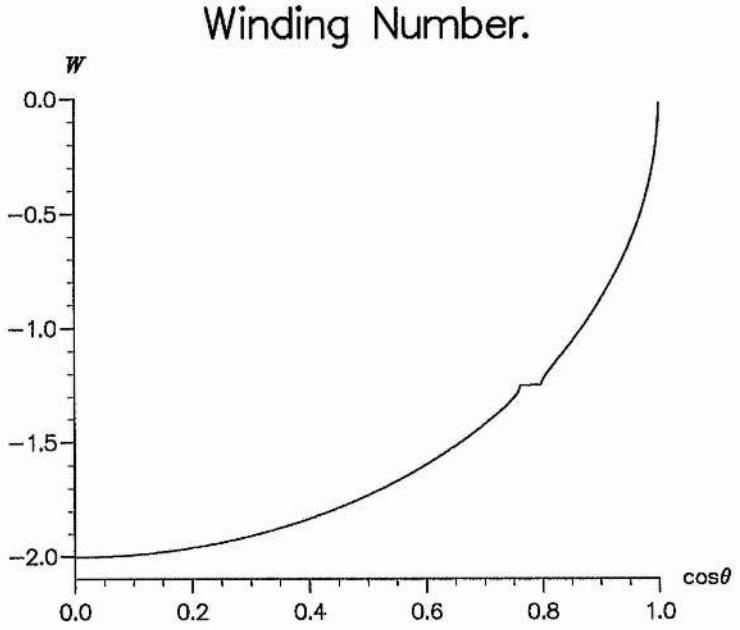

Figure 7.8: Graph showing the winding number when $a_0 = 0.1$ and $b_0 = 0.1$. Here $\Omega = 2.5$, $\omega_1(0) = 0$ and $\omega_3(0) = 1$.

7.2.2 The non-axisymmetric case.

We now examine the more complicated case of a non-axisymmetric flow. Here the condition $a_0 \neq b_0$ is imposed, with b_0 being gradually increased from a_0. Initially the value of a_0 is taken as 0.5, with $\Omega = 0.5$ also. However b_0 is now given the value 0.6 in order to impose the non-axisymmetric nature. It is clear from figures (7.9) and (7.10) that the regions of instability have become wider and more numerous than those in figures (7.1) and (7.2), but although the system is more unstable, the major characteristics of the axisymmetric case are still evident.

When the value of b_0 is increased still further, the system soon becomes strongly non-axisymmetric. Figures (7.11) and (7.12) represent the case where b_0 has been increased to 0.7. Here we have a highly unstable situation with (7.11) and (7.12) showing extremely complicated behaviour. The bands are probably infinite in number and virtually any plane wave disturbance now causes instability within the basic flow. It is clear from the graphs that different initial disturbances produce different strengths of instability. In this case any disturbance introduced within $\cos^{-1} 0.93$ radians of the x_3-axis leads to a much stronger instability than any introduced outwith this region. Due to the complicated nature of the system at this highly non-axisymmetric level, it proved necessary to calculate many more data points in order to obtain accurate results. Also the amount of time needed before the limits I and W settled down was at least double that of most

axisymmetric cases.

In order to obtain a better insight into the richness of the structure, a small area of (7.11) is now examined more closely. Figures (7.13) and (7.14) show an interval of (7.11) and (7.12) between $\cos\theta = 0.85$ and $\cos\theta = 0.9$. Here an enhanced resolution of 0.0001 radians was employed, with the time over which the growth rates and winding numbers were calculated being increased to $t = 3000$. Even at this higher resolution the system is clearly unstable at almost all angles, with the areas of stability still being too narrow to be shown graphically.

It was found that any further increase in b_0 continued to destablize the system still further and, due to the already complicated nature, no greater insight into the behaviour of the system can be gained by presenting additional data. With this in mind attention is now switched to the the role that Ω has upon the stability in non-axisymmetric cases.

First Ω is increased from 0.5 to 1.0 for the case when $a_0 = 0.5$ and $b_0 = 0.7$. The results are shown in figures (7.15) and (7.16). Here the system displays a much more ordered form than in figures (7.11) and (7.12). Regions of stability can now be isolated at some higher values of θ and, although the growth rates at some angles are higher than before, the instability bands are now well defined. If the value of Ω is raised further, this time to 2.0, the calculated growth rates and winding numbers take the values displayed in figures (7.17) and (7.18). It is clear that only two main areas of instability now exist, the main one being

between $\cos\theta = 0.55$ and $\cos\theta = 0.95$, and a smaller and weaker region around $\cos\theta = 0.15$. Note that the maximum growth rates have now started to decrease as the forcing frequency has a stronger stabilizing effect. Increasing Ω to 3.0, figures (7.19) and (7.20), we now find only one main instability band, although two much weaker bands can be seen as peaks in figure (7.19). The main band is again weaker than the previous case when $\Omega = 2.0$, and we can now see large areas of stability.

It is obvious from figures (7.15)-(7.20) that increasing the value of Ω results in a more stable system. The number of instability bands evident in (7.15) still indicates a reasonable level of instability, but their appearence is well defined unlike the confused nature of figure (7.11). This is emphasised by a further increase in Ω. At a value of $\Omega = 5.0$ it is found that only two regions of instability exist. These are shown by the two peaks in the growth rate of figure (7.21). The growth rates are considerably smaller than those in earlier diagrams, with the width of each being extremely narrow. The isolation of such bands is indeed verging on the edge of computational accuracy and the results cannot be guaranteed. Any other instabilities occurring at higher Ω's were unable to be located due to their small magnitudes, if they exist at all.

Next we examine the effect that the ratios $\frac{a_0}{\Omega}$ and $\frac{b_0}{\Omega}$ have on the stability of the system. Examining the case when $\Omega = 2.0$, as in figures (7.17) and (7.18), a_0 and b_0 are decreased and increased in such a way that they remain in the

ratio 0.5:0.7. Figures (7.23) and (7.24) depict the stability of the system when a_0 and b_0 have been reduced to 0.4 and 0.56 respectively. Here the system has many more regions of instability than its counterpart in figures (7.17) and (7.18), but the strength of these regions has decreased substantially. Lowering a_0 and b_0 still further, figures (7.25) and (7.26), reduces the maximum growth rate but, surprisingly, admits a wider range of unstable wavenumbers, with the instability bands becoming much narrower and less well separated. Further decreases in a_0 and b_0 appear to continue this increase in the range of unstable wavenumbers, but the magnitudes of the growth rates soon become so small that the results of the computations can not be guaranteed.

We also examined what happens when the values of a_0 and b_0 are raised above 0.5 and 0.7. Figures (7.27) and (7.28) show the bands of instability isolated when a_0 and b_0 take the values 0.6 and 0.84 respectively. Here the system takes on a more ordered appearance than at lower values of a_0 and b_0, with the majority of bands being clearly visible and well defined. The instabilities that occur are now stronger than those of figures (7.17)-(7.26), but have a simpler band structure.

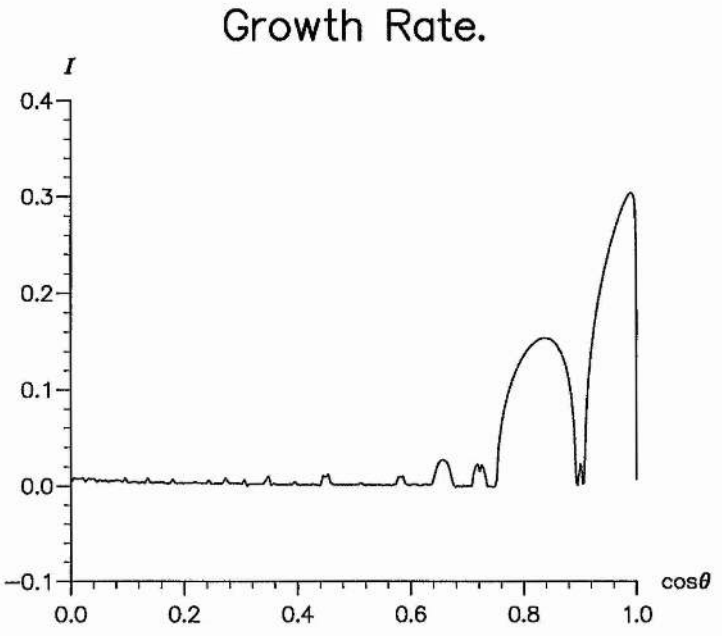

Figure 7.9: Graph showing the regions of stability for $a_0 = 0.5$ and $b_0 = 0.6$. Here $\Omega = 0.5$, $\omega_1(0) = 0$ and $\omega_3(0) = 1$.

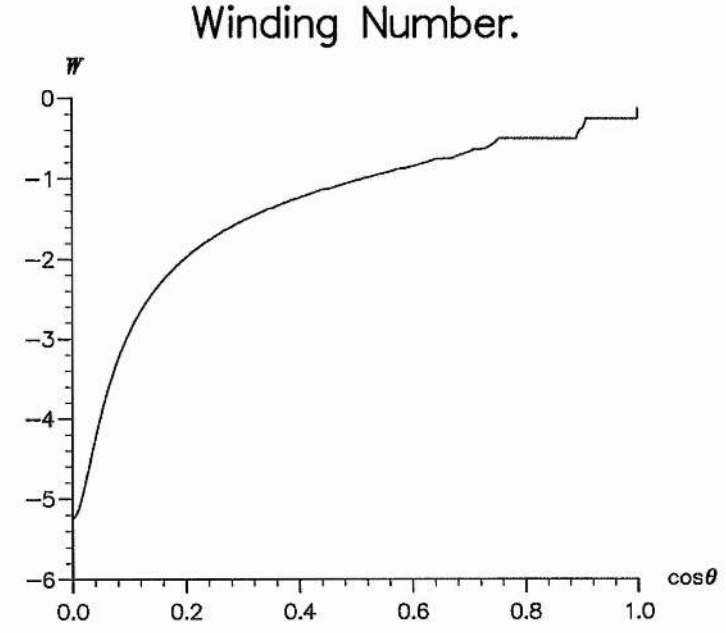

Figure 7.10: Graph showing the winding number when $a_0 = 0.5$ and $b_0 = 0.6$. Here $\Omega = 0.5$, $\omega_1(0) = 0$ and $\omega_3(0) = 1$.

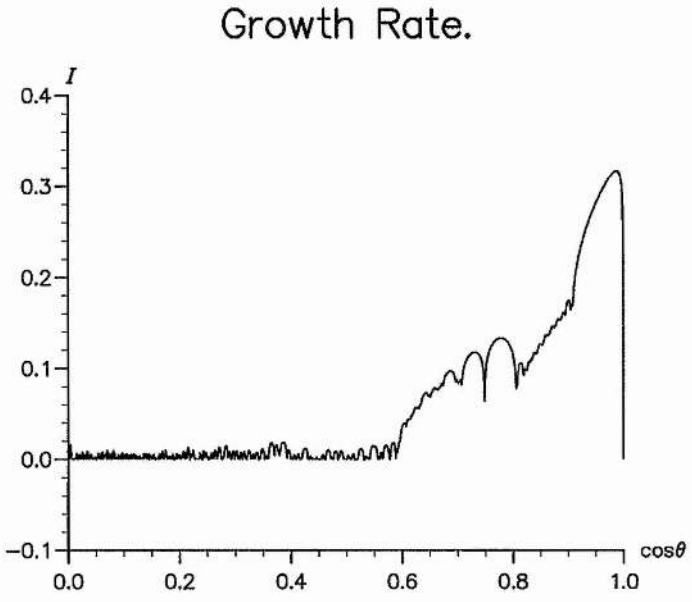

Figure 7.11: Graph showing the regions of stability for $a_0 = 0.5$ and $b_0 = 0.7$. Here $\Omega = 0.5$, $\omega_1(0) = 0$ and $\omega_3(0) = 1$.

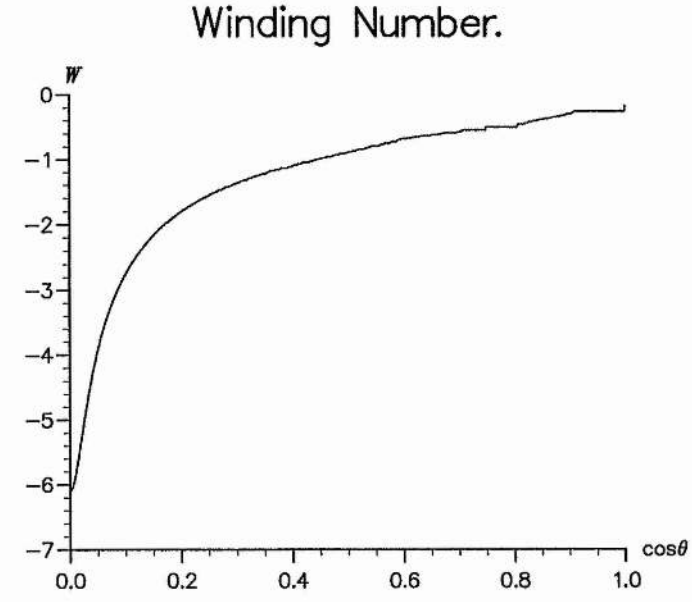

Figure 7.12: Graph showing the winding number when $a_0 = 0.5$ and $b_0 = 0.7$. Here $\Omega = 0.5$, $\omega_1(0) = 0$ and $\omega_3(0) = 1$.

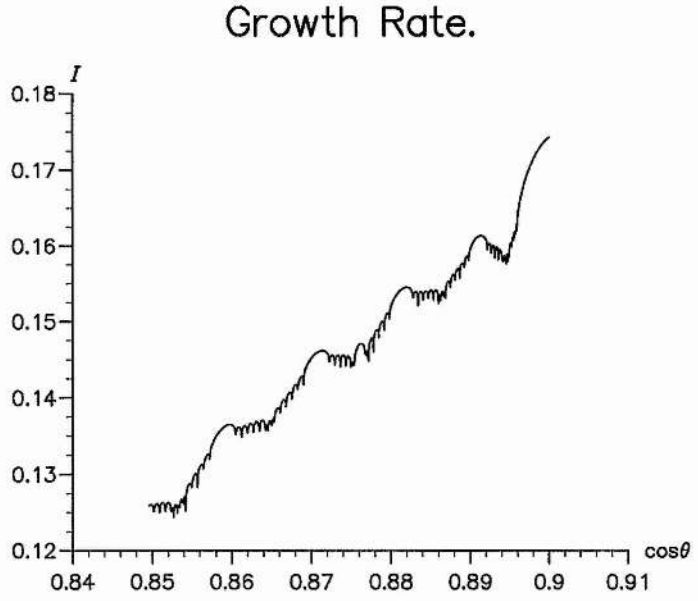

Figure 7.13: Graph showing an interval of stability when $a_0 = 0.5$ and $b_0 = 0.7$. Here $\Omega = 0.5$, $\omega_1(0) = 0$ and $\omega_3(0) = 1$.

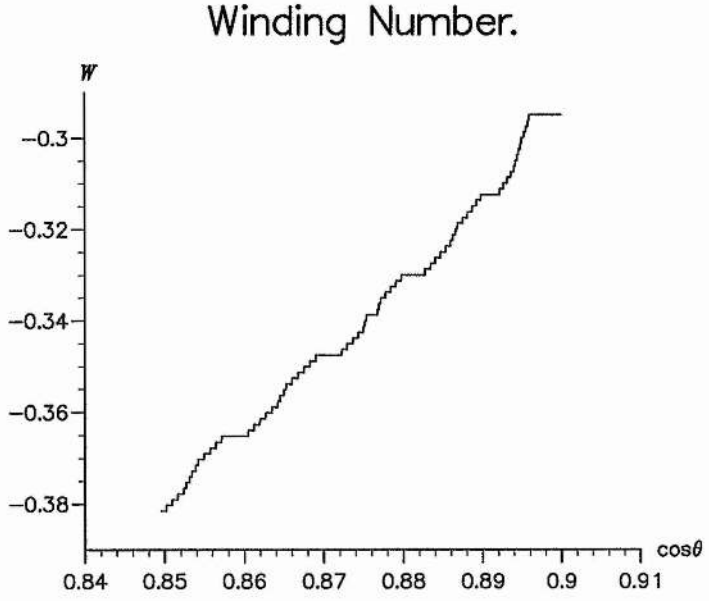

Figure 7.14: Graph showing an interval of the winding number when $a_0 = 0.5$ and $b_0 = 0.7$. Here $\Omega = 0.5$, $\omega_1(0) = 0$ and $\omega_3(0) = 1$.

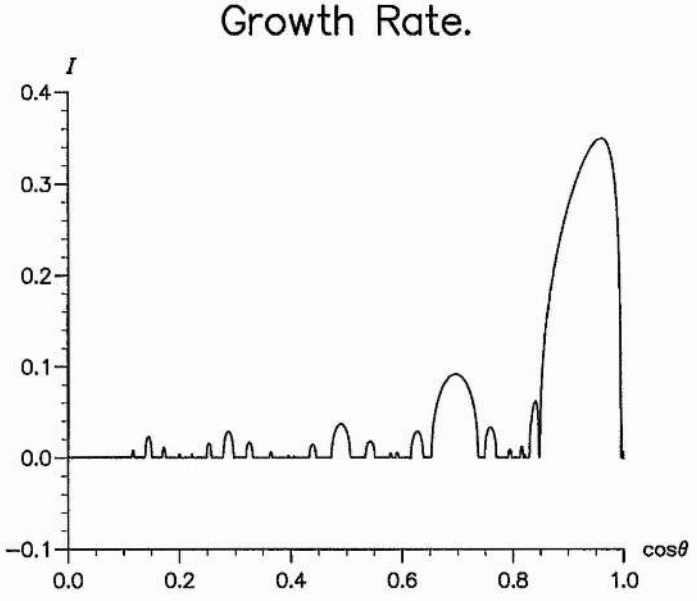

Figure 7.15: Graph showing the regions of stability when $a_0 = 0.5$ and $b_0 = 0.7$. Here $\Omega = 1.0$, $\omega_1(0) = 0$ and $\omega_3(0) = 1$.

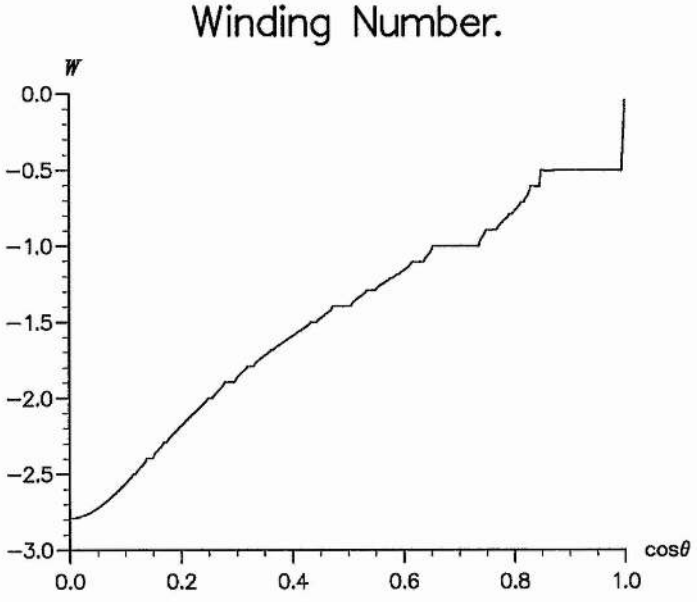

Figure 7.16: Graph showing the winding number when $a_0 = 0.5$ and $b_0 = 0.7$. Here $\Omega = 1.0$, $\omega_1(0) = 0$ and $\omega_3(0) = 1$.

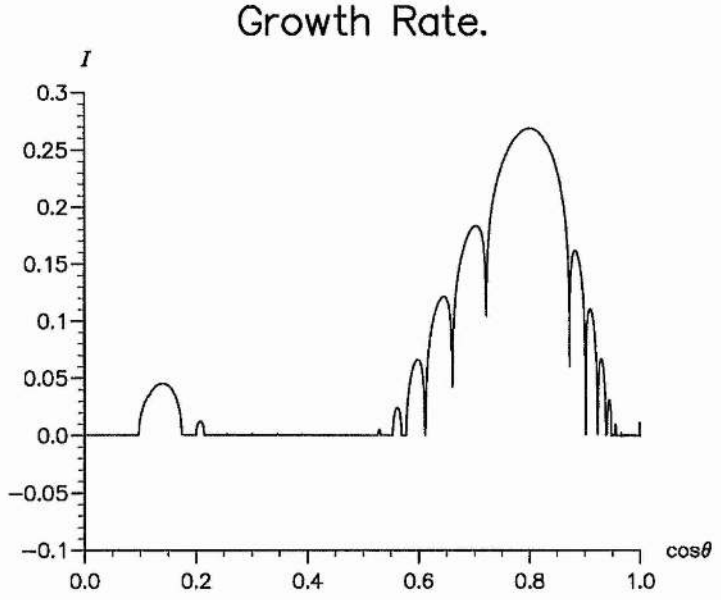

Figure 7.17: Graph showing the regions of stability when $a_0 = 0.5$ and $b_0 = 0.7$. Here $\Omega = 2.0$, $\omega_1(0) = 0$ and $\omega_3(0) = 1$.

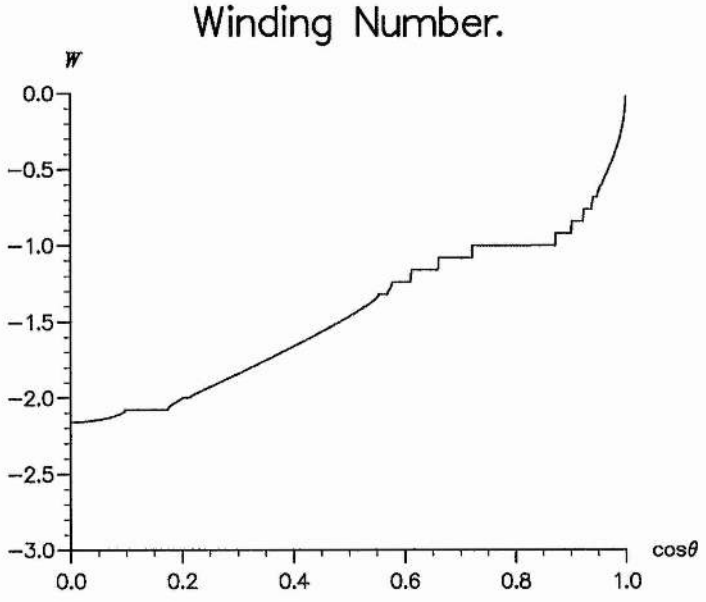

Figure 7.18: Graph showing the winding number when $a_0 = 0.5$ and $b_0 = 0.7$. Here $\Omega = 2.0$, $\omega_1(0) = 0$ and $\omega_3(0) = 1$.

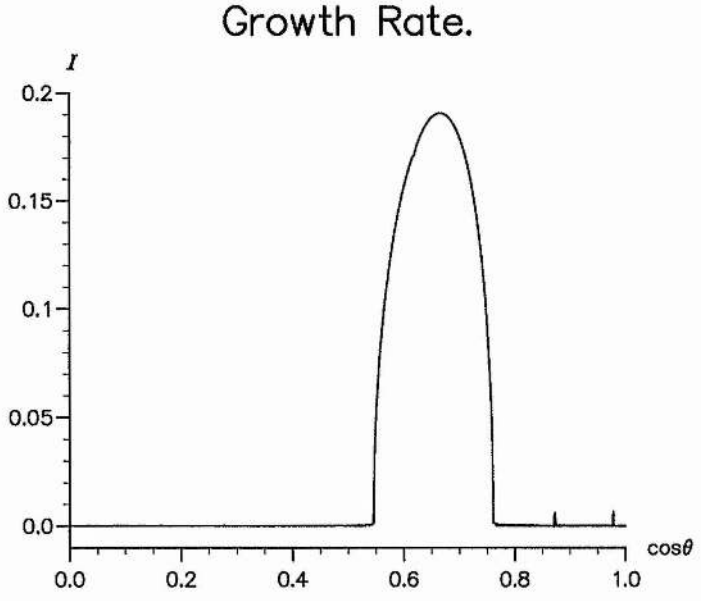

Figure 7.19: Graph showing the regions of stability when $a_0 = 0.5$ and $b_0 = 0.7$. Here $\Omega = 3.0$, $\omega_1(0) = 0$ and $\omega_3(0) = 1$.

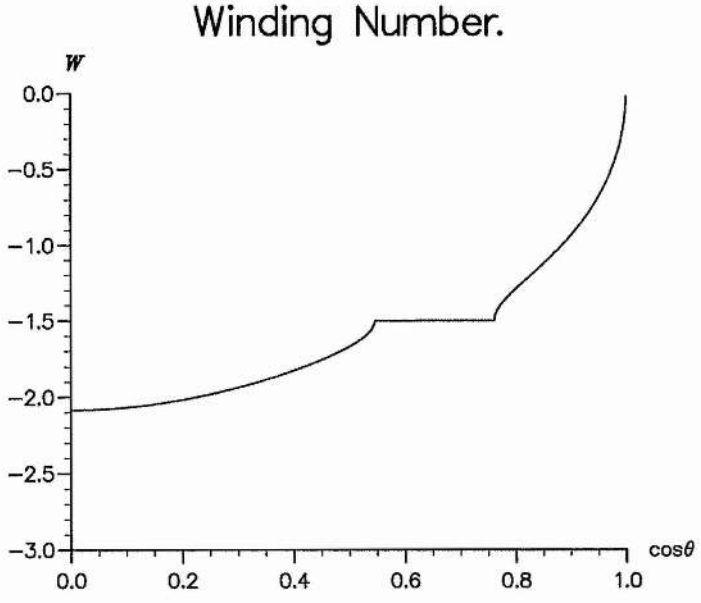

Figure 7.20: Graph showing the winding number when $a_0 = 0.5$ and $b_0 = 0.7$. Here $\Omega = 3.0$, $\omega_1(0) = 0$ and $\omega_3(0) = 1$.

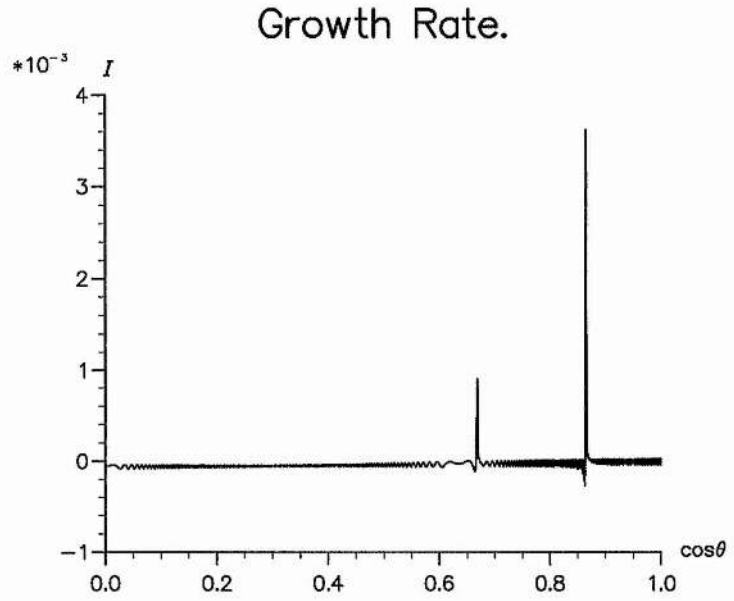

Figure 7.21: Graph showing the regions of stability when $a_0 = 0.5$ and $b_0 = 0.7$. Here $\Omega = 5.0$, $\omega_1(0) = 0$ and $\omega_3(0) = 1$.

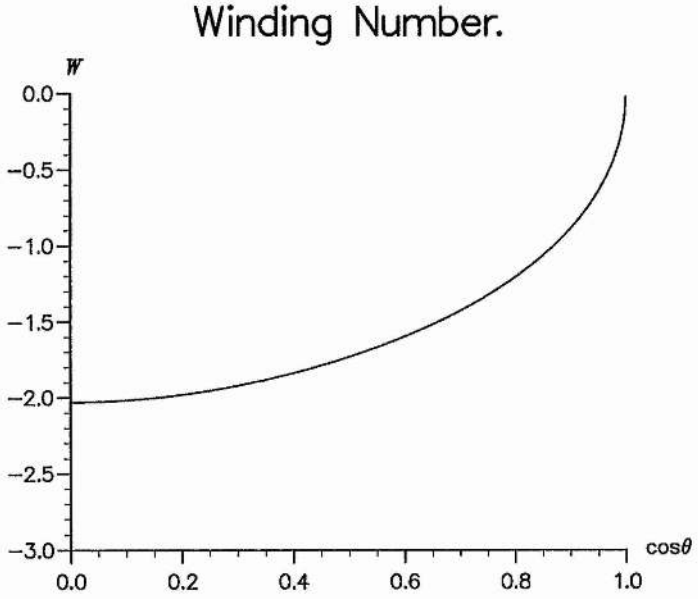

Figure 7.22: Graph showing the winding number when $a_0 = 0.5$ and $b_0 = 0.7$. Here $\Omega = 5.0$, $\omega_1(0) = 0$ and $\omega_3(0) = 1$.

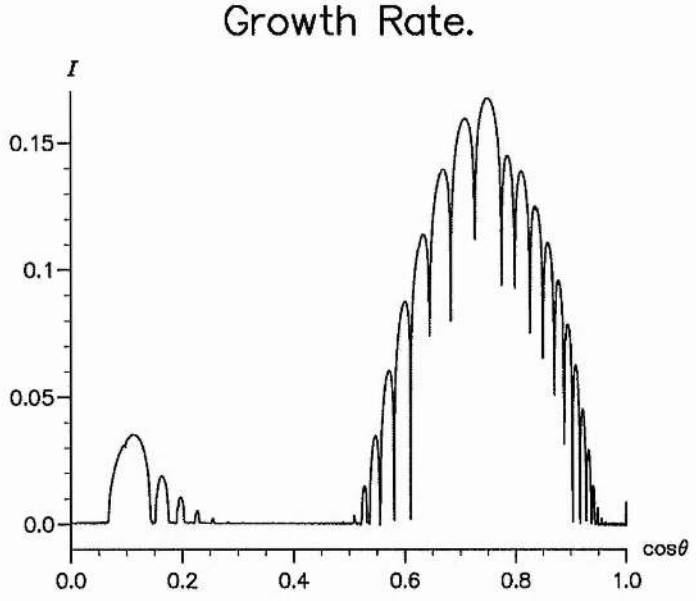

Figure 7.23: Graph showing the regions of stability when $a_0 = 0.4$ and $b_0 = 0.56$. Here $\Omega = 2.0$, $\omega_1(0) = 0$ and $\omega_3(0) = 1$.

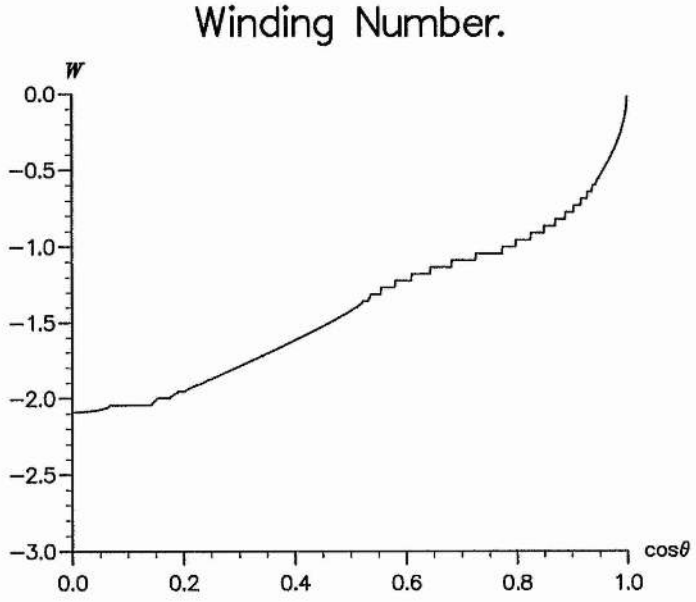

Figure 7.24: Graph showing the winding number when $a_0 = 0.4$ and $b_0 = 0.56$. Here $\Omega = 2.0$, $\omega_1(0) = 0$ and $\omega_3(0) = 1$.

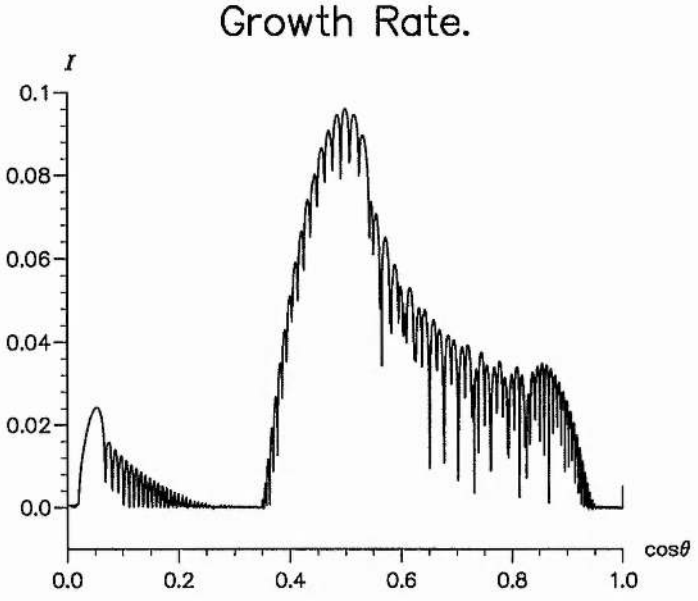

Figure 7.25: Graph showing the regions of stability when $a_0 = 0.3$ and $b_0 = 0.42$. Here $\Omega = 2.0$, $\omega_1(0) = 0$ and $\omega_3(0) = 1$.

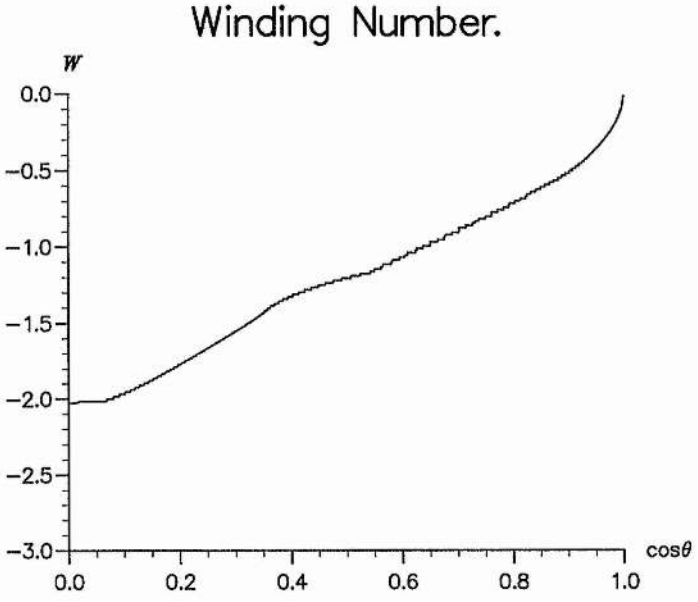

Figure 7.26: Graph showing the winding number when $a_0 = 0.3$ and $b_0 = 0.42$. Here $\Omega = 2.0$, $\omega_1(0) = 0$ and $\omega_3(0) = 1$.

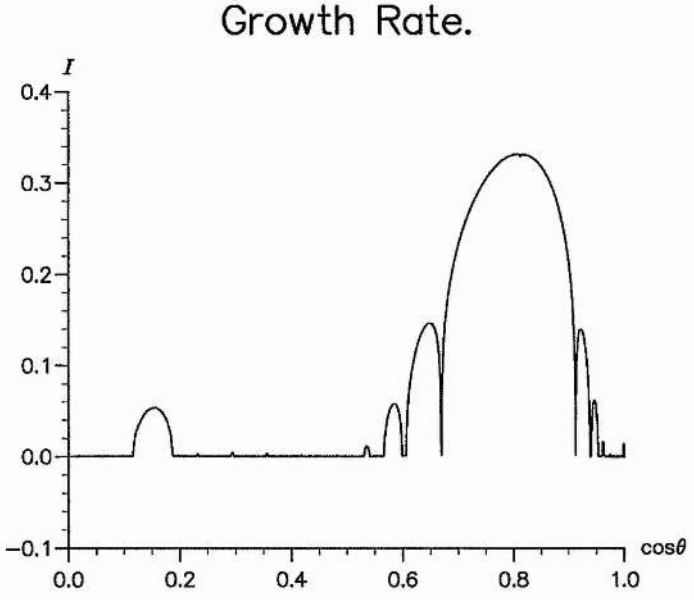

Figure 7.27: Graph showing the regions of stability when $a_0 = 0.6$ and $b_0 = 0.84$. Here $\Omega = 2.0$, $\omega_1(0) = 0$ and $\omega_3(0) = 1$.

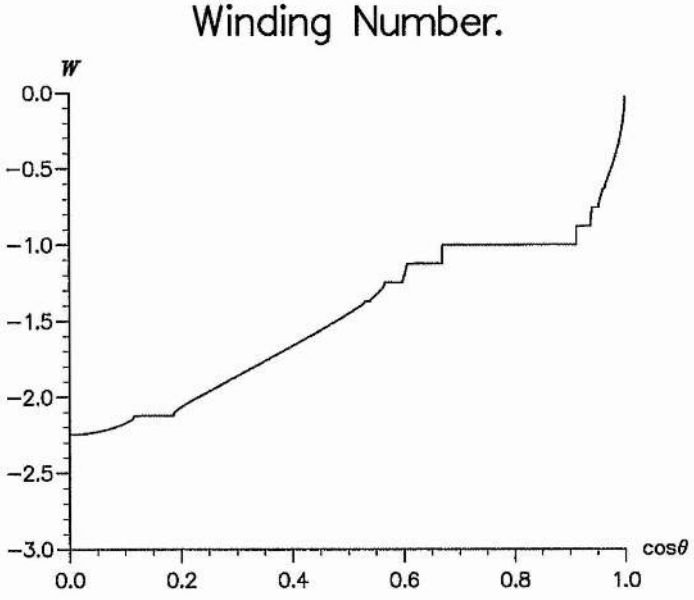

Figure 7.28: Graph showing the winding number when $a_0 = 0.6$ and $b_0 = 0.84$. Here $\Omega = 2.0$, $\omega_1(0) = 0$ and $\omega_3(0) = 1$.

7.3 Discussion.

In this chapter we have considered time-dependent flows subject to oscillatory rates of strain directed constantly along the coordinate axes. When these rates of strain are axisymmetric, the results are equivalent to those of Craik & Allen (1992). For the axisymmetric case, $a_0 = b_0$, it is found that the ratio $\frac{a_0}{\Omega}$ plays a central role in determining the stability of the system. An increase in Ω or decrease in a_0, b_0 is found to increase the stability of the basic flow to plane wave disturbances. When $\frac{a_0}{\Omega}$ is sufficiently small, the governing equations reduce to Mathieu's equation, see Craik & Allen section 3, and the number and position of the instability bands may be predicted. Our results agree with their predictions for regions of instability and support their view that the weak higher order instabilities are extremely difficult to find, computationally.

As expected, the non-axisymmetric case changes the system to a highly unstable state. For weakly non-axisymmetric cases, the main instability bands closely resemble those of the corresponding axisymmetric case, but this resemblence breaks down as the non-axisymmetric nature is increased. For highly non-axisymmetric cases, the system is found to be unstable to nearly all initial disturbances when the forcing frequency Ω is small enough. As shown, the instability bands appear infinite in number and vary greatly in strength. Increasing the frequency Ω again stabilizes the system, with the instability bands becoming

less numerous and much weaker.

When the amplitudes of the straining are reduced, one would expect the stability of the system to increase as in the axisymmetric case. This is found to be not quite so. Although the maximum growth rate of the unstable disturbances is not as strong as before, when Ω is small the range of unstable wavenumbers is enlarged. With the decrease, bands of instability seem to break down into many smaller bands, with instability occurring over a wider range of initial disturbances. For small enough amplitudes of straining, the strength of these bands becomes so small that they cannot be accurately confirmed by the computations. The overall stability of the system is not simply determined by the ratio $\frac{a_0}{\Omega}$ as in the axisymmetric case. For large enough Ω no instability bands were found, but at smaller values the system is highly unstable. The amplitudes of the straining become increasingly important when Ω is small and at all times they govern the strength of the instabilities. When these amplitudes are zero, no instabilities of course occur.

The non-axisymmetric case is considerably more complicated than its axisymmetric counterpart, with the system displaying rich structure in certain parameter ranges. The effect of the straining frequency is shown to be similar in both cases, but the straining amplitudes clearly play a more complicted role when they are non-axisymmetric.

Bibliography

Banerjee, P. P. & Korpel, A. 1982 *Phys. Fluids* **25**, 1938-1943.

Bayly, B. J. 1986 *Phys. Rev. Lett.* **57**, 2160-2171.

Bayly, B. J., Holm, D. D. & Lifschitz, A. 1995 *Phil. Trans. Roy. Soc. Lond.* (To appear.)

Becker, J. & Miles, J. W. 1986 *Z.A.M.P.* **37**, 641-650.

Benjamin, T. B. & Ursell, F. 1954 *Proc. Roy. Soc. Lond.* A **225**, 505-515.

Benney, D. J. 1962 *J. Fluid Mech.* **14**, 577-584.

Byrd, P. F. & Friedman, M. D. 1954 *Handbook of Elliptic integrals for engineers and scientists.* Springer Verlag.

Case, K. M. & Chiu, S. C. 1977 *Phys. Fluids* **20**, 742-745.

Craik, A. D. D. 1985 *Wave Interactions and Fluid Flows.* Cambridge Univ. Press.

Craik, A. D. D. & Criminale, W.O. 1986 *Proc. R. Soc. Lond.* A **406**, 13-26.

Craik, A. D. D. 1989 *J. Fluid Mech.* **198**, 275-292.

Craik, A. D. D. & Allen, H. R. 1992 *J. Fluid Mech.* **234**, 613-627.

Craik, A. D. D., Nagata, M. & Moroz, I. M. 1992 *Wave Motion* **15**, 173-183.

Craik, A. D. D. 1995 *Laminar-Turbulent Transition: Proc. IUTAM Symp. Sept. 1994, Sendai, Japan.* ed. R. Kobayashi, 53-58. Springer Verlag.

Dodge, F. T., Kana, D. D. & Abramson, H. 1965 *AIAAJ.* **3**, 685-695.

Faraday, M. 1831 *Phil. Trans. Roy. Soc. Lond.* **121**, 299-340.

Gledzer, E. B. & Ponomarev, V. M. 1992 *J. Fluid Mech.* **240**, 1-30.

Gu, X. M. & Sethna, P. R. 1987 *J. Fluid Mech.* **183**, 543-565.

Hammack, J. L. & Henderson D. M. 1993 *Ann. Rev. Fluid Mech.* **25**, 55-97.

Harrison, W. J. 1909 *Proc. Lond. Math. Soc.* **7**, 107-121.

Henderson, D. M. & Miles, J. W. 1991 *J. Fluid Mech.* **222**, 449-470.

Henstock, W. & Sani, R. L. 1974 *Lett. Heat Mass Transfer* **1**, 95-102.

Hogan, S. J. 1984 *Phys. Fluids* **27**, 42-45.

Hughes, D. W. & Proctor, M. R. E. 1990 *Physica* D **46**, 163-176.

Hughes, D. W. & Proctor, M. R. E. 1994 *Wave Motion* **20**, 201-209.

Johnson, R. & Moser, J. 1982 *Commun. Math. Phys.* **84**, 403-483.

Jones, M. C. W. 1992 *Wave Motion* **15**, 267-283.

Kaup, D. J. 1981 *J. Math. Phys.* **22**, 1176-1181.

Kelvin, Lord. 1887 *Phil. Mag.* **24** (5), 188-196.

Kerswell, R. R. 1993 *Geophys. Astrophys. Fluid Dyn.* **72**, 107-144.

Kida, S. 1981 *J. Phys. Soc. Japan* **50**, 3517-3520.

Kinsman, B. 1969 *Wind Waves: Their Generation and Propagation on the Ocean Surface.* Prentice-Hall, Englewood Cliffs, N.J.

Lamb, H. 1932 *Hydrodynamics.* 6th edn. Cambridge Univ. Press.

Landman, M. J. & Saffman, P. G. 1987 *Phys. Fluids* **30**, 2339-2342.

Langnado, R. R., Phan-Thein, N. & Leal, L. G. 1984 *Phys. Fluids.* **27**, 1094-1101.

Longuet-Higgins, M. S. 1962 *J. Fluid Mech.* **12**, 321-332.

Longuet-Higgins, M. S. & Phillips, O. M. 1962 *J. Fluid Mech.* **12**, 333-336.

Longuet-Higgins, M. S. & Smith, N. D. 1966 *J. Fluid Mech.* **25**, 417-435.

Malkus, W. V. R. 1989 *Geophys. Astrophys. Fluid Dyn.* **48**, 123-134.

Matthiessen, L. 1868 *Ann. Phys.* **134**, 107-117.

Matthiessen, L. 1870 *Ann. Phys.* **141**, 375.

McDougall, S. R. & Craik, A. D. D. 1991 *Wave Motion* **13**, 155-165.

McGoldrick, L. F. 1965 *J. Fluid Mech.* **21**, 305-331.

McGoldrick, L. F., Phillips, O. M., Huang, N. E. & Hodgson, T. H. 1966 *J. Fluid Mech.* **25**, 437-456.

McGoldrick, L. F. 1970a *J. Fluid Mech.* **42**, 193-200.

McGoldrick, L. F. 1970b *J. Fluid Mech.* **40**, 251-271.

McGoldrick, L. F. 1972 *J. Fluid Mech.* **52**, 725-751.

Miles, J. W. 1976 *J. Fluid Mech.* **75**, 419-448.

Miles, J. W. 1984 *J. Fluid Mech.* **146**, 419-448.

Miles, J. W. 1985 *Z.A.M.P.* **36**, 337-345.

Mitropolsky, Y. A. 1965 *Problems of Asymptotic Theory of Non-Stationary Vibrations*. Israel Program for Scientific Translations, Jerusalem.

Miyazaki, T. & Fukumoto, Y. 1992 *Phys. Fluids* A **4**, 2515-2522.

Moser, J. & Poschel, J. 1982 *Physica* A **124**, 535-542.

Nagata, M. 1989 *J. Fluid Mech.* **209**, 265-284.

Nayfeh, A. H. 1973 *J. Fluid Mech.* **59**, 803-816.

Ockendon, J. R. & Ockendon, H. 1973. *J. Fluid Mech.* **59**, 397-413.

Orr, W. McF. 1907a *Proc. R. Irish Acad.* A **27**, 9-69.

Orr, W. McF. 1907b *Proc. R. Irish Acad.* A **27**, 69-138.

Phillips, O. M. 1960 *J. Fluid Mech.* **9**, 193-217.

Phillips, O. M. 1961 *J. Fluid Mech.* **11**, 143-155.

Phillips, O. M. 1977 *The Dynamics of the Upper Ocean.* 2nd edn. Cambridge Univ. Press.

Phillips, O. M. 1981 *J. Fluid Mech.* **106**, 215-227.

Pierrehumbert, R.T. 1986 *Phys. Rev. Lett.* **57**, 2157-2159.

Poincaré, H. 1910 *Bull Astron.* **27**, 321.

Rayleigh, Lord. 1883a *Philos. Mag.* **15**, 229-235.

Rayleigh, Lord. 1883b *Philos. Mag.* **16**, 50-58.

Rott, N. 1970 *Z.A.M.P.* **21**, 570-582.

Simmons, W. F. 1969 *Proc. R. Soc. Lond.* A **309**, 551-575.

Simon, B. 1982 *Advances Appl. Mech.* **3**, 463-490.

Stokes, G. G. 1847 *Trans. Camb. Phil. Soc.* **8**, 441-455.

Waleffe, F. A. 1990 *Phys. Fluids* A **2(1)**, 76-80.

Wersinger, J-M., Finn, J. M. & Ott, E. 1980 *Phys. Fluids* **23**, 1142-1154.

West, B. J. 1981 *Deep Water Gravity Waves.* Lecture Notes in Physics No. 146, Springer.

Whitham, G. B. 1965a *Proc. Roy. Soc.* A **283**, 238-261.

Whitham, G. B. 1965b *J. Fluid Mech.* **22**, 273-283.

Whitham, G. B. 1967 *J. Fluid Mech.* **27**, 399-412.

Whitham, G. B. 1974 *Linear and Nonlinear Waves.* Wiley, New York.

Wilton, J. R. 1915 *Phil. Mag.* **29**, 688-700.

Yuen, H. C. & Lake, B. M. 1982 *Advances in Appl. Mech.* **22**, 67-229.